

Neutron capture on gallium in the  
astrophysical s process using time of flight

Dissertation

zur Erlangung des Doktorgrades  
der Naturwissenschaften

vorgelegt am Fachbereich Physik  
der Johann Wolfgang Goethe-Universität  
in Frankfurt am Main

von  
Cem Deniz Kurtulgil  
aus Lingen (Ems)

Frankfurt am Main 2022

(D30)



Vom Fachbereich Physik der  
Johann Wolfgang Goethe-Universität  
als Dissertation angenommen.

<b>Dekan:</b>	Prof. Dr. Harald Appelshäuser
<b>Gutachter:</b>	Prof. Dr. René Reifarth
<b>Gutachter:</b>	Prof. Dr. Christoph Langer

<b>Datum der Disputation:</b>	20.10.2022
-------------------------------	------------



It's still magic even if you know how it's done.

*Terry Pratchett, A Hat Full of Sky*



The stellar nucleosynthesis of elements heavier than iron can primarily be attributed to neutron capture reactions in the s and r process. While the s process is considered to be well understood with regards to the stellar sites, phases and conditions where it occurs, nucleosynthesis networks still need accurate neutron capture cross sections with low uncertainties as input parameters. Their quantitative outputs for the isotopic abundances produced in the s process, coupled with the observable solar abundances, can be used to indirectly infer the expected r process abundances. The two stable gallium isotopes,  $^{69}\text{Ga}$  and  $^{71}\text{Ga}$ , have been shown in sensitivity studies to have considerable impact on the weak s process in massive stars. The available experimental data, mostly derived from neutron activation measurements for quasi-stellar neutron spectra at  $k_{\text{B}}T = 25$  keV, show disagreements up to a factor of three.

Determining the differential neutron capture cross section can provide input data for the whole range of astrophysically relevant energies. To that end, a neutron time of flight experimental campaign at the n\_TOF facility at CERN was performed for three months, using isotopically enriched samples of both isotopes. The data taken at the EAR1 experimental area covered a wide neutron energy range from thermal to several hundred keV. The respective differential and spectrum averaged neutron capture cross sections for  $^{69}\text{Ga}$  and  $^{71}\text{Ga}$  were determined in this thesis. They show good agreement with the evaluated cross sections for  $^{71}\text{Ga}$ , but reproduce the deviations from the evaluated data that other, more recent activation measurements showed for  $^{69}\text{Ga}$ .





Die Nukleosynthese der meisten Elemente schwerer als Eisen in Sternen erfolgt durch Neutroneneinfangreaktionen im s- und r-Prozess. Während der s-Prozess bezüglich der stellaren Szenarien, Brennphasen und Bedingungen, unter welchen er vorkommt, als gut verstanden gilt, erfordern Nukleosynthese Netzwerkrechnungen genaue Neutroneneinfangwirkungsquerschnitte als Eingabeparameter. Ihre quantitativen Ergebnisse der s-Prozess Isotopenhäufigkeiten, kombiniert mit den beobachtbaren solaren Isotopenhäufigkeiten, können genutzt werden, um die zu erwartenden r-Prozess-Häufigkeiten zu bestimmen. Sensitivitätsstudien des schwachen s-Prozess in massiven Sternen haben gezeigt, dass die zwei stabilen Gallium Isotope,  $^{69}\text{Ga}$  und  $^{71}\text{Ga}$ , einen beachtlichen Einfluss auf diesen haben. Die verfügbare experimentelle Datenlage stammt primär aus Aktivierungsmessungen für quasi-stellare Neutronenspektren bei  $k_{\text{B}}T = 25 \text{ keV}$ , und weist Unterschiede bis zu einem Faktor drei zueinander auf.

Die Bestimmung der differentiellen Neutroneneinfangwirkungsquerschnitte ermöglicht es, Eingabeparameter für den kompletten Bereich astrophysikalisch relevanter Energien zu generieren. Zu diesem Zweck wurde am n\_TOF Experiment am CERN eine Flugzeitmessung über drei Monate hinweg durchgeführt. Die gemessenen Daten erstrecken sich über einen Neutronenenergiebereich von thermischen Energien bis zu mehreren hundert keV. Die differentiellen und über die jeweiligen stellaren Neutronenspektren gemittelten Wirkungsquerschnitte von  $^{69}\text{Ga}$  und  $^{71}\text{Ga}$  wurden in dieser Arbeit bestimmt. Sie zeigen gute Übereinstimmung mit den evaluierten Wirkungsquerschnitten für  $^{71}\text{Ga}$ , reproduzieren aber die in kürzlich durchgeführten Aktivierungsmessungen gefundenen Abweichungen von den evaluierten Daten für  $^{69}\text{Ga}$ .



**Abstract****Kurzübersicht**

<b>1. Introduction</b>	<b>1</b>
1.1. Stellar Nucleosynthesis . . . . .	1
1.1.1. Synthesis of light elements . . . . .	1
1.1.2. Neutron capture beyond fusion . . . . .	3
1.2. The case of gallium . . . . .	7
1.3. Goals of this work . . . . .	7
<b>2. Theory</b>	<b>9</b>
2.1. Neutron capture reactions . . . . .	9
2.1.1. Q-value . . . . .	9
2.1.2. Cross section . . . . .	10
2.2. The time of flight technique . . . . .	14
2.3. Radiation detection . . . . .	16
2.3.1. Photon interactions with matter . . . . .	16
2.3.2. Neutron interactions . . . . .	18
2.3.3. Scintillation detectors . . . . .	18
<b>3. Gallium samples</b>	<b>22</b>
3.1. Properties of gallium . . . . .	22
3.2. Sample production . . . . .	23
3.3. Capture target assembly . . . . .	24

<b>4. The n_TOF experiment</b>	<b>26</b>
4.1. Facility overview . . . . .	26
4.1.1. Neutron production through spallation . . . . .	27
4.1.2. The $\gamma$ -flash . . . . .	28
4.2. Experimental Setup . . . . .	30
4.2.1. Beam position and profile . . . . .	31
4.2.2. Auxiliary samples . . . . .	32
4.2.3. Neutron flux . . . . .	33
<b>5. Analysis</b>	<b>34</b>
5.1. Detector calibration . . . . .	34
5.2. Detector consistency . . . . .	36
5.2.1. Neutron beam monitors . . . . .	36
5.2.2. C <sub>6</sub> D <sub>6</sub> stability . . . . .	41
5.3. ToF to energy conversion . . . . .	43
5.4. Dead time correction . . . . .	44
5.5. Background subtraction . . . . .	48
5.5.1. Ambient component . . . . .	49
5.5.2. Beam related component . . . . .	50
5.5.3. Scattering component . . . . .	52
5.6. Pulse height weighting technique . . . . .	56
5.6.1. Monte Carlo detector simulation . . . . .	57
5.6.2. Determination the weighting function . . . . .	58
5.7. Determination of the neutron flux . . . . .	61
5.7.1. Evaluated n_TOF flux . . . . .	61
5.7.2. Saturated resonance technique . . . . .	62
5.8. Uncertainties . . . . .	64
5.8.1. ToF to energy conversion . . . . .	64
5.8.2. Background subtraction . . . . .	64
5.8.3. Pulse height weighting . . . . .	65
5.8.4. Neutron flux normalization . . . . .	66
5.8.5. Sample mass and geometry . . . . .	66
5.8.6. Sample contamination correction . . . . .	67
<b>6. Results</b>	<b>69</b>
6.1. Cross section from yields . . . . .	69
6.2. MACS calculation . . . . .	69

6.3. Comparison of results . . . . .	74
6.3.1. Previous experimental data situation . . . . .	74
6.3.2. Current data . . . . .	74
<b>7. Conclusion and outlook</b>	<b>77</b>
<b>8. Zusammenfassung</b>	<b>79</b>
<b>A. Appendix</b>	<b>84</b>
A.1. Uncertainty calculation . . . . .	84
A.2. Chemical sample composition . . . . .	85
A.3. Calibration sources . . . . .	87
A.4. Monitor consistency . . . . .	93
A.5. Rebound effect . . . . .	94
A.6. PHWT . . . . .	97
<b>List of figures</b>	<b>100</b>
<b>List of tables</b>	<b>101</b>
<b>List of literature</b>	<b>107</b>



## 1.1. Stellar Nucleosynthesis

The discipline of nuclear astrophysics aims to quantitatively explain the production of the observed (solar) isotopic abundances, using models of our current understanding of different stellar scenarios, with nuclear reaction rates as input parameters. The primordial nucleosynthesis following the Big Bang produced the initial abundances of hydrogen, helium and traces of lithium in the universe. Moving along the chart of nuclides, the *light nuclei* up to iron are produced through fusion reactions of charged particles in stars. The majority of all *heavy nuclei* beyond iron are then created through different types of neutron capture reactions.

Burbidge, Burbidge, Fowler and Hoyle [1] laid many foundations for our understanding of the synthesis of heavy elements in their seminal paper from 1957. The abundance distribution of isotopes in our solar system, as depicted in Figure 1.1, is the standard which stellar models need to be able to reproduce, and which at the same time motivates new experimental measurements of those nuclear reaction cross sections with the highest uncertainties and/or highest impact on the final isotopic abundance distribution.

### 1.1.1. Synthesis of light elements

The light elements hydrogen, helium and in minute amounts lithium and beryllium were created in the *primordial nucleosynthesis* within the first 20 minutes after the

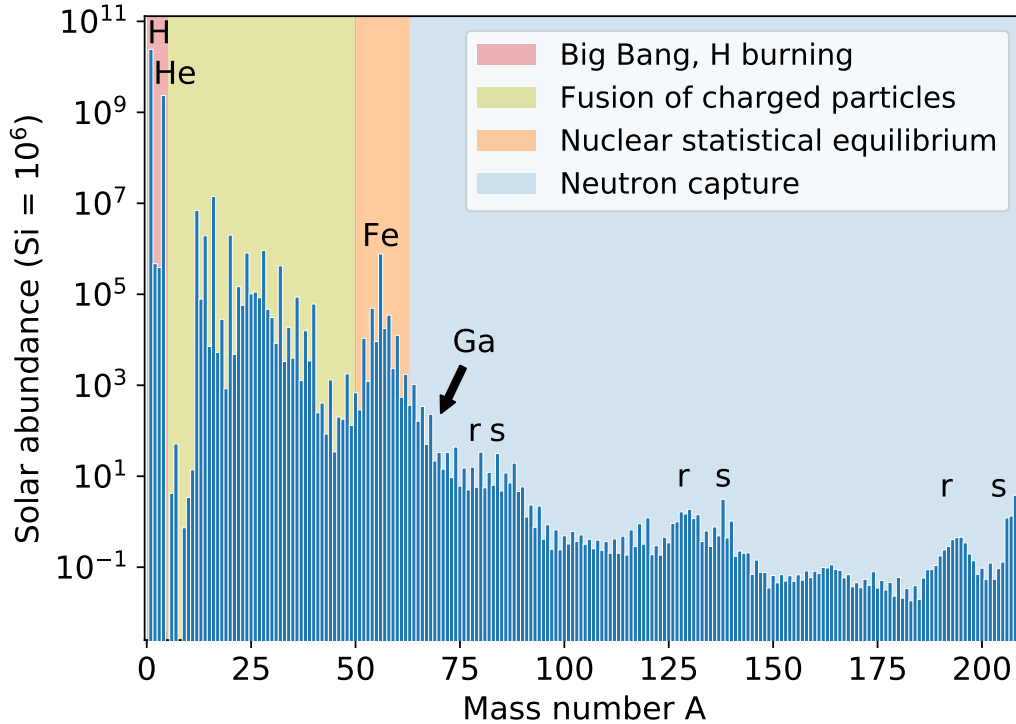


**Figure 1.1.:** Solar abundance distribution extracted from Lodders *et al.* [2], normalized to the Si abundance. The different (main) production mechanisms and phases of the mass regions are marked, alongside the r- and s-process abundance peaks, and the mass region of the two gallium isotopes relevant for this work in the weak s process.

Big Bang. Through the cooling of the universe and gravitational forces, these initial building blocks continued to form the first stars. These stars then produced energy through several types of fusion reactions, counteracting the gravitational pressure of their own mass. The first of these fusion reactions is burning hydrogen to helium, until all hydrogen in the core is exhausted. The lack of thermal outward pressure causes the star to contract, compressing and heating up the helium core until its ignition temperature is reached, at which point the helium burning again produces enough energy to stabilize the compression. This sequence of phases repeats itself, depending on the initial mass of the star, for the burning of helium, carbon, oxygen, neon and silicon, each time creating a core of the new "fuel", and an onion-like structure of layers surrounding it. Each successive burning phase occurs at a higher temperature, and has a shorter duration, starting from billions of years for H-burning in light stars, all the way to the order of one day for Si-burning in massive stars [3]. There are no freely occurring fusion processes for higher mass numbers in heavy stars, due to the fact that the nuclei in the iron region (Figure 1.1) have the highest



binding energy per nucleon. Further fusion reactions would not produce additional energy, and thus fail to stabilize the star against its gravitational pressure. This leads to an accumulation of elemental abundance in the mass region around iron [3].

### 1.1.2. Neutron capture beyond fusion

Due to this boundary, and Coulomb repulsion between charged particles, the probability for their fusion reactions occurring decreases drastically. Other processes have to take place in the interior of stars to explain the observable abundances of heavier nuclei. A series of successive neutron capture reactions were postulated as an explanation. The *s process* for slow neutron capture reactions at lower neutron densities and the *r process* for rapid neutron capture reactions at higher neutron densities also explain the double-peak structures at the neutron shell closures  $N = 50, 82, 126$  (Figure 1.1). Other processes like the *p process* of photo-disintegration reactions are needed to explain the production of about 35 nuclei that are shielded from being produced through neutron capture and successive  $\beta$ -decay [1], but the majority of all nuclear abundances can be produced through the s and r process, which will be further explained below.

In general, the change in abundance over time  $\frac{dN}{dt}$  of a nucleus  ${}^A_ZX$  in a stellar environment can be expressed as

$$\begin{aligned} \frac{dN(A, Z)}{dt} = & \lambda_n(A-1, Z)N(A-1, Z) + \lambda_\beta(A, Z \pm 1)N(A, Z \pm 1) \\ & - (\lambda_n(A, Z) - \lambda_\beta(A, Z))N(A, Z), \end{aligned} \quad (1.1)$$

with  $\lambda_n$  and  $\lambda_\beta$  the respective neutron capture- and decay rates. The classical form of such an approach by Burbidge *et al.* [1], due to lack of detailed knowledge of the stellar environments, assumed constant temperature and neutron density. Using more accurate neutron cross sections, Seeger *et al.* [4] showed that the s process had to take place in more than one stellar scenario, namely the main (Section 1.1.2) and weak (Section 1.1.2) component. These differ in their characteristic parameters neutron fluence, seed abundance, neutron density and temperature [5]. From those parameters, the s process and its resulting abundances can be constructed.

In a stellar scenario at given temperature  $T$ , the *neutron exposure*  $\tau$  can be defined as

$$\tau = v_T \int n_n(t) dt, \quad (1.2)$$

where the neutron density  $n_n$  is integrated over time, and scaled by the temperature-dependent average thermal velocity of the neutrons  $v_T$ . Differentiating Eq.(1.2), using the definition of the Maxwellian Averaged Cross Section (MACS, Section 2.1.2) to rewrite  $\lambda_n$ , and assuming no  $\beta$ -decay on a competitive time scale, Eq.(1.1) leads to

$$\frac{dN(A, Z)}{d\tau} = \langle \sigma \rangle_{(A-1, Z)} N(A-1, Z) - \langle \sigma \rangle_{(A, Z)} N(A, Z). \quad (1.3)$$

Since a dynamic system strives towards equilibrium, i.e.  $\frac{dN(A, Z)}{d\tau} = 0$ , this is equivalent to

$$\langle \sigma \rangle_{(A-1, Z)} N(A-1, Z) = \langle \sigma \rangle_{(A, Z)} N(A, Z), \quad (1.4)$$

meaning the abundance flow into and out of the nucleus is in *local equilibrium*. This approximation holds between neutron shell closures, and motivates the so-called  $\sigma N_s$  curves ([4]), which show good agreement between the main component prediction and observed solar abundances for  $A > 90$ .

However, this model of the classical main component fails to properly describe the observable abundances for  $A \leq 90$ , underestimating them by a large margin. Adding the produced abundances from the aforementioned weak s process, which is further explained in Section 1.1.2, does again lead to a good agreement in this mass region.

### The s-process main component

The main component of the s process takes place in *asymptotic giant branch* (AGB) stars of initial mass  $1 M_\odot - 5 M_\odot$ . These stars have left the main sequence, and are in the advanced stages of He shell burning. All He in the core has already been exhausted, but the temperatures are not yet high enough to start carbon burning, resulting in an inert carbon-oxygen core, a thin surrounding layer of helium and a convective hydrogen envelope [5]. H burning in the envelope increases the amount of

He in the intershell over a time of around  $10^4$  years, raising its temperature, density and pressure. Upon reaching critical conditions, the He ignites in an explosive thermal pulse, the *helium flash*, with a duration in the order of years [6, 7]. This alternation between H- and He-burning phases leads to the designation *thermally pulsating asymptotic giant branch* (TP-AGB). Upon ignition, the He-shell expands, and the H-burning is extinguished. The now occurring convective energy transport mixes H into the upper layer of the He-intershell, producing  $^{13}\text{C}$  through  $^{12}\text{C}(p, \gamma)^{13}\text{N}(\beta^+)^{13}\text{C}$ . The produced  $^{13}\text{C}$  pockets cause the first mode of neutron production in the s process main component via



These reactions occur during the relatively long periods between thermal pulses at temperatures around  $0.9 \cdot 10^8$  K and reach neutron densities  $n_n \approx 10^6 \text{ cm}^{-3} - 10^7 \text{ cm}^{-3}$  [5].

The second mode of neutron production occurs during the thermal pulses, when the temperatures in the convective zone reach  $2.5 \cdot 10^8$  K, via



Although a higher flux of  $10^{10} \text{ cm}^{-3}$  is reached during this phase, it only contributes around 5% to the total time-integrated neutron flux in the TP-AGB star due to its comparatively short duration in the order of years.

Overall, the described production modes result in neutron capture rates that are relatively slow compared to the competing  $\beta$ -decays, resulting in a reaction path close to the valley of stability.

### The s-process weak component

The main component of the s process fails to describe the abundances in the mass region  $A \leq 90$ . A second part of the s process, the *weak component*, provides the missing additional abundances in this mass region to explain the observable quantities. It takes place in massive stars with  $M \geq 8 M_{\odot}$  and at smaller time-integrated neutron flux. They end their existence in an explosive type II supernova, the ejecta carrying material with the s-process signature into the interstellar medium [8].

The neutron source in these stars is the reaction



taking place in convective core He burning and again in shell C burning. The necessary  ${}^{22}\text{Ne}$  is produced from  ${}^{14}\text{N}$ , which in turn originates from the CNO cycle during H burning. During He burning, the convective core reaches temperatures of  $3 \cdot 10^8 \text{ K}$  ( $k_{\text{B}}T \approx 25 \text{ keV}$ ) and neutron densities of  $n_n \approx 10^6 \text{ cm}^{-3}$  [5, 9]. Once all He in the core has been exhausted, the neutron production reaction Eq.(1.7) is reactivated with the remaining  ${}^{22}\text{Ne}$  [10] during shell C burning at temperatures upwards of  $10^9 \text{ K}$  ( $k_{\text{B}}T \approx 90 \text{ keV}$ ) and neutron densities of  $n_n \approx 10^{11} \text{ cm}^{-3} - 10^{12} \text{ cm}^{-3}$  [5, 8].

Unlike its main component, the weak s process does not possess high enough neutron fluence to fulfill Eq.(1.4) and thus achieve reaction flow equilibrium. As a consequence, variations in neutron capture rates do not just have an effect on the abundance of the respective isotope, but affect all subsequent, heavier isotope abundances as well. An example of this is given in Figure 1.2 for the case of the two stable isotopes of gallium.

### The r process

The rapid neutron capture process is responsible for the production of the other  $\sim 50\%$  of all elemental abundances heavier than iron. It is characterized by the time-scales of those neutron captures being significantly smaller than the competing decay time scales of the capture products, leading to successive neutron captures onto stable nuclei and the production of isotopes further away from the valley of stability.

Initially, the stellar site of the r process was assumed to be explosive supernova scenarios of stars with  $M \geq 8 M_{\odot}$ . However, further studies showed that not all r-process abundances up to Uranium could properly be explained by this. The production of lighter heavy elements such as Sr, Y and Zr by neutrino-driven winds originating from core-collapse supernova explosions [11] led to the term *weak r process* in these scenarios.

Currently, the most likely main r process site is assumed to be neutron star mergers [12], with recent observational evidence from GW170817 [13] supporting this model.

Nevertheless, direct simulation and quantitative description of the r process remain difficult and computationally complex. In addition, many nuclear reaction rates for such high energy scenarios are still impacted by rather large uncertainties.

Therefore, r-process abundances are oftentimes indirectly determined via difference method by subtracting s-process from solar abundances. This increases the importance of exact quantitative knowledge of the s process and its produced abundances even more.

## 1.2. The case of gallium

Gallium, with its two stable isotopes with mass  $A = 69$  and  $A = 71$ , is mostly produced in the weak s process. Nucleosynthesis simulations by Pignatari *et al.* [8] have shown gallium to be among the most overabundant elements with respect to the solar abundance at the end of C shell burning.

As previously mentioned in Section 1.1.2, the comparatively low neutron fluence in the weak s process and the resulting lack of reaction flow equilibrium increase the effect of variations in the specific neutron capture rates onto gallium, by propagating to all subsequent elemental abundances. This was illustrated using the NETZ code [9], a tool that simulates s-process nucleosynthesis by solving a system of differential equations. It uses profiles of temperature, neutron and electron density over time, as well as initial seed distribution as input parameters. Especially the neutron pulse enables simulating the main and weak component of the s process independently. Figure 1.2 was produced for a massive star model with solar metallicity, varying the respective neutron capture cross sections of  $^{69}\text{Ga}$  and  $^{71}\text{Ga}$  from [14] by a factor of 2.0 up and down. The *propagation effect* is clearly visible.

## 1.3. Goals of this work

In order to achieve more accurate weak s process abundance predictions from nucleosynthesis simulations, and given gallium's high impact on those, it is important to reduce uncertainties and resolve discrepancies of its neutron capture cross sections at astrophysically relevant energies from  $k_{\text{B}}T = 25 \text{ keV}$  to  $k_{\text{B}}T = 100 \text{ keV}$ . Most of the previous data were determined from activation measurements for quasi-stellar

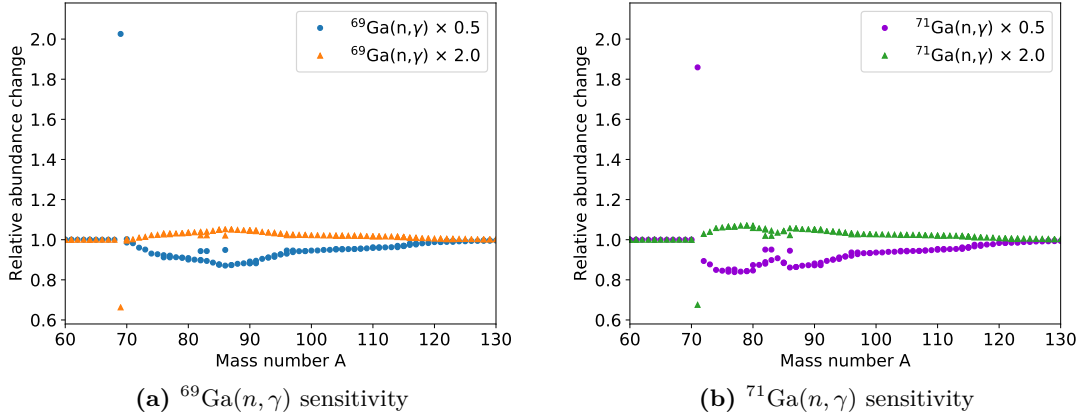


**Figure 1.2.:** Sensitivity of isotopic abundances in the weak s process to variations of the respective gallium neutron capture cross sections. The abundances were produced using the NETZ tool [9].

spectra at singular energies, with the inherent limitations towards the shape of the spectra and uncertainties on the integrated cross sections this entails.

Time of flight measurements, on the other hand, produce neutron-energy-resolved yields and cross sections, showing resonance properties and enabling the comparison with integral measurements (MACS, see 2.1.2) at any point within the large neutron energy range. They are therefore the method of choice to determine the cross sections at all desired energies.

The n\_TOF facility (Section 4) provides high-intensity neutron pulses in the energy range from thermal energies of 10 meV up to around 500 keV. Its long flight path enables a good resolution in time, and thus, neutron energy resolution of  $\Delta E/E \leq 10^{-3}$  up to 10 keV, and  $\leq 5 \cdot 10^{-3}$  up to 100 keV [15].

A measurement campaign was conducted to determine the differential cross section of both gallium isotopes, using enriched samples.

## 2.1. Neutron capture reactions

This work aims at determining the neutron capture cross section of  $^{69}\text{Ga}$  and  $^{71}\text{Ga}$  in astrophysical scenarios. To that end, a short overview of the theoretical concepts necessary for both understanding and measuring the relevant interactions will be presented in this chapter.

### 2.1.1. Q-value

The so-called *Q value* is defined as the difference in the total energy of the initial reactants and the final products, i.e. in the case of a  $(n, \gamma)$  reaction

$$Q = E_{\text{initial}} - E_{\text{final}} = c^2 \cdot \left[ m({}^A_Z\text{X}) + m(\text{n}) - m({}^{A+1}_Z\text{X}) \right]. \quad (2.1)$$

A positive value of  $Q$  thereby denotes an exothermic reaction. The target nucleus  ${}^A_Z\text{X}$  and the neutron  $\text{n}$  form the product nucleus  ${}^{A+1}_Z\text{X}$ , and release the energy

$$E^* = Q + \frac{A}{A+1} E_n, \quad (2.2)$$

$E_n$  being the energy of the incident neutron. The total detectable energy caused by the capture reaction would therefore be  $E^*$ .

### 2.1.2. Cross section

#### Geometric cross section

The *cross section* of a reaction between particles quantitatively describes the probability of their interaction. It is measured in units of area. The simplest model is interpreting their interacting probability as the overlap of their cross-sectional areas. In the approximation of two spherical particles, this leads to the *geometric cross section*

$$\sigma_{geo} = \pi(R_1 + R_2)^2. \quad (2.3)$$

Herein, the radius of the respective nuclei can be estimated by

$$R = R_0 \cdot A^{1/3}, \quad (2.4)$$

with  $R_0 = 1.21$  fm [16]. Since the nuclear radii range in the order of fm, the unit 1 b (Barn)  $\cong 10^{-24}$  cm<sup>2</sup> is used for nuclear reaction cross sections. Owing to the quantum mechanical nature of these reactions, Eq.(2.3) is modified to

$$\sigma = \pi \cdot \lambda^2, \quad (2.5)$$

with the de Broglie wavelength  $\lambda$ . This means that the cross section is usually not constant, but shows dependence on both the type of interaction force, and the relative velocity  $\nu$  between the interacting particles,  $\sigma = \sigma(\nu)$ .

#### Non-resonant neutron capture

Neutron capture reactions, which are the main focus of this work, can occur in two different modes, non-resonant and resonant. The non-resonant reactions only involve two particles in the exit channel [17] and can be written as





where the excited nucleus directly decays into the product nucleus,  $x$  being any number of possible particles like  $\gamma, p$  or  $\alpha$ . In this case, the cross section can be written as

$$\sigma_n(E_n) \simeq \lambda_n^2 \Gamma_n(E_n) \Gamma_x(Q + E_n). \quad (2.7)$$

For most relevant neutron energies,  $Q \gg E_n$ , and thus  $\Gamma_x(Q + E_n) \simeq \Gamma_x(Q) = \text{const.}$  The cross section  $\sigma_n(E_n)$  is therefore only dependent on the de Broglie wavelength term,  $\lambda^2 \propto 1/\nu_n^2$ , and the partial width of the entrance channel,  $\Gamma_n(E_n)$ . It can be shown [17] that these capture events are dominated by s-wave neutrons, leading to  $\Gamma_n(E_n) \propto \nu_n$  and finally

$$\sigma_n(E_n) \propto \frac{1}{\nu_n^2} \nu_n = \frac{1}{\nu_n} = \frac{1}{\sqrt{E_n}}. \quad (2.8)$$

### Resonant neutron capture

The mode of *resonant* neutron capture occurs when the neutron and target nucleus form an excited *Compound Nucleus* in the entrance channel, which then decays to lower-lying states. This process is contingent on the energy of the entrance channel,  $Q + E_R$  matching the energy  $E_r$  of a possible excited state of the compound nucleus. The probability of this capture is given by the Breit-Wigner formula [17]

$$\sigma_{n,\text{res}}(E_n) = \pi \lambda^2 \frac{2J + 1}{(2J_n + 1)(2J_X + 1)} \frac{\Gamma_n \Gamma_\gamma}{(E_n - E_R)^2 + (\Gamma/2)^2}, \quad (2.9)$$

with  $J_n$  and  $J_X$  the spins of the incident neutron and target nucleus  $X$ ,  $J$  the angular momentum of the excited state in the compound nucleus.  $\Gamma_n$  and  $\Gamma_\gamma$  are the partial width of the respective production and decay of the compound nucleus, and  $\Gamma$  the total width.  $E_R$  is defined through the aforementioned necessary equality  $Q + E_R = E_r$  for the resonant capture to occur.

The resulting neutron capture cross sections are a superposition of the  $1/\nu$  baseline and the resonant structures. They can be divided into three regions [5]:

- The resolved resonance region, where individual resonances can clearly be separated.

- The unresolved resonance region, where the level spacing is still larger than the resonance widths, but the cross section cannot be described in terms of individual resonances.
- The continuum region, where the level spacing grows so small that the overlapping resonances form a continuous cross section.

### Reaction rate

In a stellar gas with particle densities  $N_X$  and  $N_Y$  of particle types  $X$  and  $Y$  with relative velocity  $\nu$ , any of the two types can be assumed to be at rest, and the other moving at velocity  $\nu$ , without loss of generality. Let the nuclei  $Y$  be at rest, then the effective reaction area they present towards one nucleus  $X$  is the nucleus-nucleus cross section  $\sigma(\nu)$  multiplied by the number density  $N_Y$  [17]. In order to scale this up to all moving nuclei  $X$ , one has to multiply with the flux  $N_X \nu$ . This leads to the total rate of nuclear reactions per volume

$$r = N_X N_Y \nu \sigma(\nu). \quad (2.10)$$

In the general context of projectiles  $P$  interacting with a target sample  $T$ , and emitting ejectile(s)  $E$ , the cross section  $\sigma$  as probability of their interaction can be written as

$$\sigma = \frac{N_E}{N_T \cdot N_P / A} = \frac{N_E}{N_T \cdot \phi}. \quad (2.11)$$

Here,  $N_E$  and  $N_T$  denote the respective numbers of nuclei,  $N_P$  the number of projectiles per time, and  $A$  the cross-sectional area of the target. The last two quantities can be combined into the flux  $\phi$  of incident projectiles.

Up until this point,  $\nu$  was treated as a constant. However, in a stellar environment, it follows a probability distribution  $\phi(\nu)$ . The  $\nu\sigma(\nu)$  term in Eq.(2.10) needs to be folded with the distribution of the velocity, resulting in the averaged value of  $\nu\sigma(\nu)$  over  $\phi(\nu)$ :

$$\langle \sigma \nu \rangle = \int_0^\infty \phi(\nu) \nu \sigma(\nu) d\nu. \quad (2.12)$$

This *reaction rate per particle pair*,  $\langle\sigma\nu\rangle$ , combined with accounting for identical particle types  $X = Y$ , transforms Eq.(2.10) to

$$r = N_X N_Y \langle\sigma\nu\rangle (1 + \delta_{XY})^{-1} . \quad (2.13)$$

The next step of interest is finding an explicit velocity distribution for the particles in stellar environments. The *Maxwell-Boltzmann distribution*

$$\phi(\nu) = 4\pi\nu^2 \left(\frac{m}{2\pi k_B T}\right)^{3/2} \exp\left(-\frac{m\nu^2}{2k_B T}\right), \quad (2.14)$$

holds for nondegenerate stellar matter moving at nonrelativistic velocities in thermal equilibrium [17].

The maximum of the velocity distribution is found via  $\frac{d\phi(\nu)}{d\nu} \stackrel{!}{=} 0$  to be

$$\nu_T = \sqrt{\frac{2k_B T}{m}}, \quad (2.15)$$

with an equivalent energy  $E_T = k_B T$ .

Inserting the Maxwell-Boltzmann distribution Eq.(2.14) and the reduced mass  $\mu = \frac{m_X m_Y}{m_X + m_Y}$  of the two interacting particles into Eq.(2.12) leads to

$$\langle\sigma\nu\rangle = 4\pi \left(\frac{\mu}{2\pi k_B T}\right)^{3/2} \int_0^\infty \nu^3 \sigma(\nu) \exp\left(-\frac{\mu\nu^2}{2k_B T}\right) d\nu. \quad (2.16)$$

Using the center-of-mass energy  $E = \frac{1}{2}\mu\nu^2$ , one finally obtains the reaction rate per particle pair

$$\langle\sigma\nu\rangle = \left(\frac{8}{\pi\mu}\right)^{1/2} \frac{1}{(k_B T)^{3/2}} \int_0^\infty \sigma(E) E \exp\left(-\frac{E}{k_B T}\right) dE. \quad (2.17)$$

Eq.(2.8) shows that  $\sigma\nu$  and by extension,  $\langle\sigma\nu\rangle$  are constant for a reaction that only follows the  $1/\nu$  law. In that case, measuring  $\sigma_n(E_n)$  for just one energy  $E_n$  would automatically determine the cross section at all other energies as well. Since the  $1/\nu$  assumption does not strictly hold across all  $E_n$ , measurements across wider energy ranges are often necessary.

### Maxwellian Averaged Cross Section (MACS)

For applications in the context of stellar environments, it is useful to scale the reaction rate per particle pair Eq.(2.17) by the most probable velocity  $\nu_T = \sqrt{k_B T / \mu}$  of the Maxwell-Boltzmann distribution [5]:

$$\langle \sigma \rangle = \frac{\langle \sigma \nu \rangle}{\nu_T} = \left( \frac{4}{\pi} \right)^{1/2} \frac{1}{(k_B T)^2} \int_0^\infty \sigma(E) E \exp\left(-\frac{E}{k_B T}\right) dE. \quad (2.18)$$

This *Maxwellian Averaged Cross Section* (MACS) denotes an effective cross section value for a star at an average temperature  $T$ . For the different parts of the s process that take place in a range  $k_B T = 8 - 90$  keV,  $\sigma(E)$  needs to be determined up to several hundred keV in order to calculate the necessary MACS.

## 2.2. The time of flight technique

The time of flight (*ToF*) method (Figure 2.1) enables neutron-energy-resolved cross section measurements by performing in-beam  $\gamma$ -ray spectroscopy on the prompt cascade emitted from the de-excitation of the compound nucleus (Section 2.1.2). Knowledge of the flight path length  $L$ , neutron mass  $m_n$  and flight time  $t$  calculates the neutron energy as

$$E_n = m_n c^2 (\gamma - 1), \quad (2.19)$$

with a relativistic correction factor

$$\gamma = \left( \sqrt{1 - \frac{(L/t)^2}{c^2}} \right)^{-1}. \quad (2.20)$$

For the measured neutron energies of interest, this factor can be neglected, and Eq.(2.19) reduces to

$$E_n = \frac{1}{2} m_n \left( \frac{L}{t} \right)^2. \quad (2.21)$$

The flight time *tof* for any particle is determined via

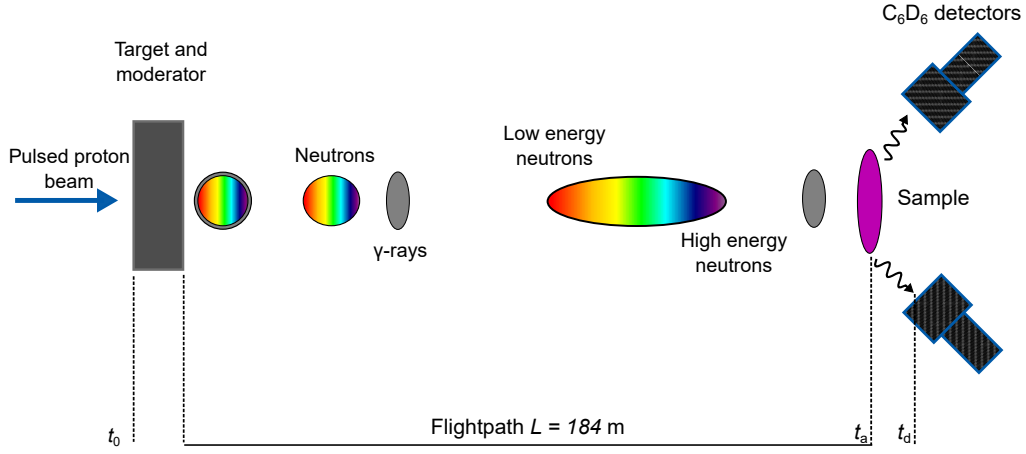


**Figure 2.1.:** The time of flight technique, from neutron production at the spallation target, along the beamline with the broadening of the neutron bunch, all the way to the capture sample and detection setup.

$$tof = t_a - t_0, \quad (2.22)$$

with  $t_a$  time of arrival at the sample when the nuclear reaction takes place, and  $t_0$  the time of particle production at the spallation target, where both neutrons and photons are produced. These simultaneously created photons and other particles moving at a speed of  $c$  (Section 4.1.2), being detected at time  $t_\gamma$ , therefore have a flight time

$$tof_\gamma = t_\gamma - t_0 = \frac{L}{c}. \quad (2.23)$$

The time of detection  $t_d$  of the  $\gamma$  resulting from the neutron capture in the sample, while in principle distinct from  $t_a$ , cannot be resolved with a timescale for nuclear processes of  $10^{-15}$  s, so we can safely set  $t_d = t_a$ .

With Eq.(2.22) and Eq.(2.23), and the general time of flight of a particle detected at time  $t_d$ , it follows

$$tof_d = t_d - t_0$$

$$t_d - t_\gamma = (tof_d + t_0) - (tof_\gamma + t_0) = tof_d - tof_\gamma = tof_d - \frac{L}{c}. \quad (2.24)$$

This leads to the calculation of the neutron time of flight,  $tof_n$ , as

$$tof_n = t_d - t_\gamma + \frac{L}{c}, \quad (2.25)$$

and Eq.(2.21) is modified to

$$E_n = \frac{1}{2}m_n \left( \frac{L}{t_d - \left(t_\gamma - \frac{L}{c}\right)} \right)^2. \quad (2.26)$$

The relative resolution of the neutron energy  $E_n$  is given by

$$\frac{\Delta E_n}{E_n} = 2 \cdot \sqrt{\left(\frac{\Delta t}{t}\right)^2 + \left(\frac{\Delta L}{L}\right)^2}. \quad (2.27)$$

A long flight path therefore improves the resolution directly (through  $\Delta L/L$ ) and indirectly, through  $\Delta t/t$ , which is also influenced by the time resolution of the detection system as well. However, this comes at the cost of the total neutron flux, which is proportional to  $1/L^2$ , so a balance between the two parameters needs to individually be considered for each measurement [5].

## 2.3. Radiation detection

Measuring the prompt or delayed radiation of a nuclear reaction with a radiation detector requires knowledge of the type of desired particle that has to penetrate the matter, and how the radiation interacts with said matter. The interactions and detector types relevant for this work will be briefly discussed [18, 19].

### 2.3.1. Photon interactions with matter

The interaction of photons with matter can mainly occur via three different mechanisms. The energy of the incident photon and the atomic number of the absorbing nuclei determine which interaction channel is the dominant one.

### Photoelectric effect

The *photoelectric effect* occurs when a photon transfers its complete energy to a bound electron, being completely stopped in the process, and the electron is ejected from the atom. This can only occur if the energy of the incident photon is higher than the binding energy of the respective electron. The photo effect is the dominant interaction for higher  $Z$  nuclei, primarily at photon energies up to around 100 keV [19].

### Compton scattering

Compton scattering is dominant for photons of energies  $100 \text{ keV} < E_\gamma < 10 \text{ MeV}$ . The incident photon scatters on a bound electron, transferring only a part of its energy. The transferred energy  $\Delta E$  from a photon of energy  $E$  depends on the scattering angle  $\theta$ :

$$\Delta E = E_\gamma \left( 1 - \frac{1}{1 + \frac{E_\gamma}{m_e c^2} (1 - \cos \theta)} \right). \quad (2.28)$$

While  $\Delta E$  reaches its maximum for  $\theta = 180^\circ$ , meaning the photon transferring the maximum amount of energy when scattering in a backward direction, it will still be smaller than the incident energy  $E_\gamma$ . Barring another interaction with the detector material, the remaining energy of the scattered photon will not be deposited, resulting in a continuous spectrum of deposited energy up to the maximum achievable  $\Delta E$ , the *Compton edge* at energy

$$E_{\text{Compton}} = \frac{2E_\gamma^2}{2E_\gamma + m_e c^2}. \quad (2.29)$$

### Pair production

The third type of interaction can only occur above a photon energy of 1022 keV, twice the electron mass  $m_e$ , upon which the photon might interact with the electric field of the nucleus to produce an electron-positron pair. The excess photon energy is distributed between the two newly formed particles in the form of kinetic energy. While the electron will be stopped in the material, the positron will annihilate with another electron in the detector material after having been slowed down sufficiently,

producing two photons of energy 511 keV. Depending on whether both, one or none of these photons interact with the detector material and deposit their energy, the total deposited energy will either be the full energy of the original photon, or be reduced by 511 keV or 1022 keV, respectively, resulting in additional peaks at these reduced energies.

### 2.3.2. Neutron interactions

Neutrons, as chargeless particles, mainly interact with other nuclei via the strong force. The small range of the strong force ( $\approx 10^{-13}$  cm) enables the neutrons to penetrate comparatively deeply into matter before interacting via several possible reaction types:

- Elastic scattering (n,n) on nuclei: This is more likely to occur for faster neutrons, which lose energy at each scattering interaction and are slowed down (*moderation*).
- Inelastic scattering: If the neutron energy is high enough, the recoil nucleus receives enough energy to be elevated to an excited state, from which it then de-excites under photon emission.
- Radiative neutron capture: The capture process already described in Section 2.1.2 and Section 2.1.2 with its characteristic  $1/v$  cross section, emitting the excitation energy in the form of  $\gamma$ -rays.
- Charged particle emitting reactions: Similar to the radiative neutron capture, but with other particles like p,  $\alpha$  etc. in the exit channel.
- Fission: The created compound nucleus splits into lighter nuclei, and emits neutrons and photons.

All these reactions can have vastly differing cross sections, depending on the energy of the interacting neutron. This needs to be considered when trying to increase the ratio between the reaction of interest and other, interfering reactions [18].

### 2.3.3. Scintillation detectors

Scintillation Detectors consist of a scintillating material and a photomultiplier (PMT). The *luminescent* material absorbs the energy of passing particles and reemits it in the form of light, which is amplified by the PMT and transformed to a voltage



signal. One of the main benefits of these kind of detectors are their fast response and recovery time in the order of nanoseconds, making them ideal for the time of flight measurements performed in this work.

### Organic scintillators

The subcategory of organic scintillators contain aromatic hydrocarbon compounds (benzene rings). The delocalized, free valence electrons in the molecules are excited to a higher level by incident radiation. In the order of ns, they decay to the ground state, emitting a light pulse corresponding to the transition energy. In addition to the good time resolution, they exhibit a low sensitivity to scattered neutrons due to their low atomic number, which makes a good choice for detecting time of flight neutron capture events.

### Total energy detectors

The method used in this measurement to detect the  $\gamma$ -ray cascade following neutron capture events and the subsequent decay of the compound nucleus is the *Total Energy Detection technique* [20]. It is based on the premise of a  $\gamma$ -ray detector with a detection efficiency  $\varepsilon_\gamma$  that is proportional to the energy of the incident photon,  $E_\gamma$ ,

$$\varepsilon_\gamma = kE_\gamma. \quad (2.30)$$

If the detection efficiency is low enough that no more than one  $\gamma$  out of any cascade is detected, the efficiency of detecting the capture event that caused the cascade only depends on the excitation energy of the compound nucleus (see Eq.(2.2))  $E^* = Q + E_{CM}$ :

$$\varepsilon_C = 1 - \prod_i (1 - \varepsilon_i) \approx \sum_i \varepsilon_i \quad (2.31)$$

$$\varepsilon_C = \sum_i \varepsilon_i = \sum_i kE_i = k \sum_i E_i = k(Q + E_n). \quad (2.32)$$

Moxon and Rae [21] developed a detector that fulfilled this proportionality. It consists of a  $\gamma$ -ray to electron converter, and a thin plastic scintillator that detects

the produced electrons. However, due to their detection efficiency of less than a few percent [20], and their insensitivity to low energy  $\gamma$ -rays, they are considered suboptimal for measuring neutron capture events on non-radioactive samples.

The next approach was eliminating the converter, and using an organic hydrogen-free scintillator. Macklin and Gibbons [22] utilized  $C_6F_6$ , which was later replaced by  $C_6D_6$  (deuterated benzene). A shortcoming of these setups is the loss of the linearity in detection efficiency (Eq.(2.32)). Maier-Leibniz proposed [22] an *a posteriori* treatment of the detected pulse heights by applying an energy-dependent weighting function to them (*Pulse height weighting technique*, further discussed in Section 5.6), reintroducing the desired relation between  $E_\gamma$  and  $\varepsilon_\gamma$  [20].

### **$C_6D_6$ detectors**

Such total energy detectors, in combination with Pulse Height Weighting, have been extensively used for neutron time of flight measurements, given their benefits of great time resolution, comparatively high efficiency and low cost. The drawback of the low atomic number detector material is the deposition of incident photon energy almost exclusively through Compton scattering (Section 2.3.1), leading to a superposition of many continuous spectra as the total detector response.

Studies by Koehler *et al.* [23] and Gruber *et al.* [24] showed that the background contribution of scattered neutrons had often been underestimated in these measurements, leading to overestimated capture cross sections. This led to several improvements in design and used materials in this kind of detector, based on Monte Carlo simulations and test measurements to characterize those designs.

The *Legnaro-type* detectors [25] used in this measurement continue the improvements of the *FZK* detectors [26]. They are almost completely made out of carbon fiber, and contain a small PMT (see Figure 2.2). This overall leads to very low neutron sensitivities of  $\varepsilon_n/\varepsilon_\gamma \approx 3 \cdot 10^{-5}$  [20].

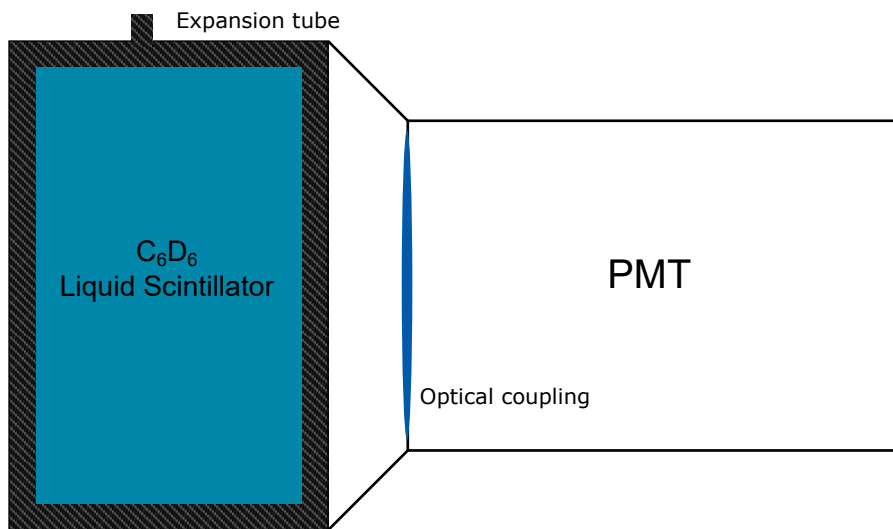


**Figure 2.2.:** Schematic of Legnaro type  $C_6D_6$  detector. The detection volume contains deuterated benzene as a liquid scintillator, and is completely encased by carbon fiber.



The samples used in this work were approximately 1 g each of highly isotopically enriched  $^{69}\text{Ga}$  and  $^{71}\text{Ga}$ . Due to its mechanical properties and restraints in compatible materials, a new method of shaping it into the desired dimensions for the experiment had to be developed.

### 3.1. Properties of gallium

The element gallium has two stable isotopes,  $^{69}\text{Ga}$  and  $^{71}\text{Ga}$ . It is a rather soft metal with a Mohs hardness of 1.5, and a melting point of  $29.76^\circ\text{C}$ . This low melting point causes it to become liquid when handled by hand for too long, or stored under warm conditions. In its liquid form, it is wetting to most materials (Teflon being one exception), and *undercools* below its freezing point, meaning that it needs to be cooled further than the melting temperature would suggest to achieve solid form.

When brought in contact with aluminium, it diffuses into its metal lattice, making it very brittle, and creating an AlGa alloy that reacts with water to form hydrogen gas, aluminium oxide and gallium. This means that no components made out of aluminium can be used to work on the samples, and an alternative to the commonly used Al sample holder rings used in nuclear physics experiments needs to be found as well.

The two enriched samples were supplied by *ISOFLEX USA*. Their isotopic distributions between the two stable isotopes can be seen in Table 3.1.

Isotope	$^{69}\text{Ga}$	$^{71}\text{Ga}$	Isotope	$^{69}\text{Ga}$	$^{71}\text{Ga}$
Content (%)	99.48	0.52	Content (%)	0.2	99.80
(a) enriched $^{69}\text{Ga}$ sample			(b) enriched $^{71}\text{Ga}$ sample		

**Table 3.1.:** Isotopic cross contaminations in the two samples.

Other impurities contained in the sample are all below 50 ppm. A detailed listing can be found in the chemical analyses [27] and [28], see Table A.1 and Table A.2.

## 3.2. Sample production

The two enriched samples were supplied as ovoid shapes of about 1 g each. Count rate estimates and the experimental setup at n\_TOF led to an intended cylindrical sample geometry with radius 1 cm and thickness 0.5 mm. To that end, a frame assembly (Figure 3.1) was constructed from stainless steel. Two thick blocks at the top and bottom encompass a steel sheet of thickness 0.5 mm, with a 2 cm circular cutout in the center. The gallium ovoid is placed in the middle of the cutout, and isolated from the upper and lower block by a thin Kapton foil. Four screws at the corner are repeatedly tightened, pressing the upper and lower block together, while slowly heating the assembly to above the melting point of gallium. Through the continuous pressure from both sides, the melting gallium ovoid slowly takes on the form of the cutout. Afterwards, the assembly is carefully lowered into liquid nitrogen to undercool and solidify the gallium disc in the desired shape.

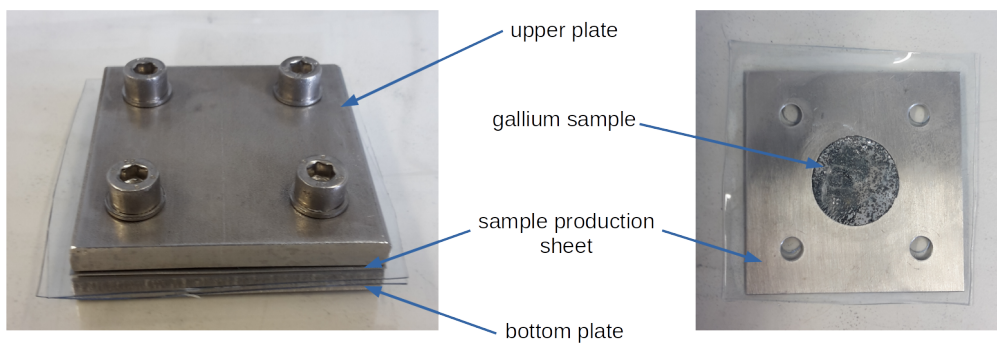


**Figure 3.1.:** The gallium sample production frame, made out of stainless steel. The plates on the top and bottom flatten the melted gallium to an even thickness, while the sheet in the center restrains it to the desired diameter.

Isotope	<sup>69</sup> Ga	<sup>71</sup> Ga
Mass (g)	0.97250(15)	0.99042(15)

**Table 3.2.:** Masses of the enriched gallium samples after production, weighed at Goethe University Frankfurt.

The samples were then removed from the assembly, weighed (see Table 3.2), and stored in an argon atmosphere, to negate the possibility of even small oxidation effects.

### 3.3. Capture target assembly

In order to place the produced samples at a reproducible, centered position with regard to the neutron beam at n\_TOF, they were mounted inside a carbon fiber frame (Figure 3.2). Due to concerns about possible melting of the gallium, a PVC ring of the same 0.5 mm thickness, 20 mm inner and 30 mm outer diameter, was placed snugly around the sample. Mylar foil of 6 μm was glued onto the front and back, connecting the carbon fiber frame with the inner part, and completely enclosing the sample within the ring, so no material would be able to escape even if it did melt. Special care was taken to use as little glue as possible and to accurately center each of the samples, in order to reduce interactions between the neutron beam and other components than the actual gallium.

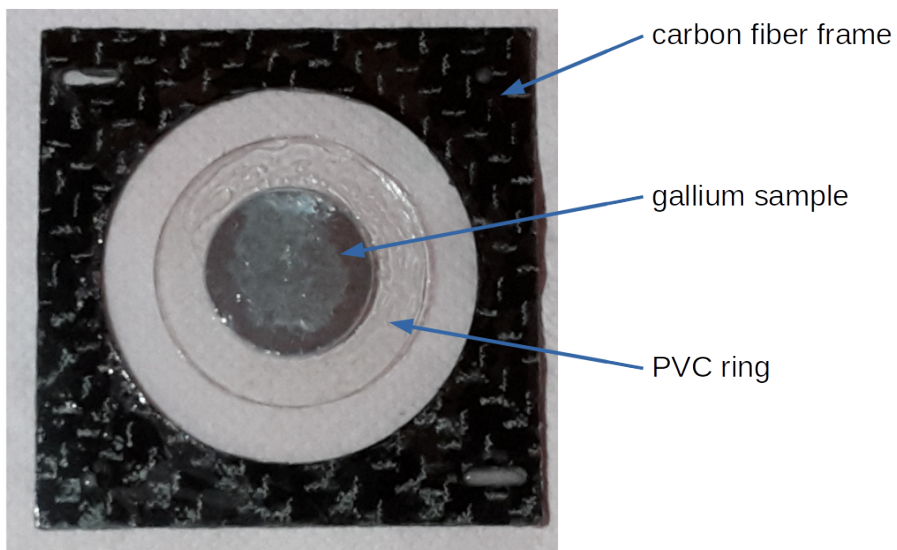


**Figure 3.2.:** Carbon fiber frame used in the capture setup, covered in the front and back by thin Mylar foil. The gallium sample is placed in the center, surrounded by a thin PVC ring. Only the ring is glued to the foil, holding the gallium in position and minimizing the amount of glue in the beam spot.



The n\_TOF experimental facility at CERN uses a pulsed neutron source to conduct *neutron time of flight* measurements. Its long flight path enables cross section measurements across a wide energy range from thermal up to several hundred keV, with high neutron energy resolution and luminosity.

## 4.1. Facility overview

At n\_TOF, a pulsed proton beam impinges on a thick lead target, creating neutrons through spallation reactions. The protons are initially accelerated in the *Proton Synchrotron (PS)* (Figure 4.1) to 20 GeV/c, and concentrated in short pulses with a width of 7 ns (rms) and a repetition rate of 0.8 Hz [29, 30]. These pulses are delivered either at full intensity (*dedicated*) of  $7 - 8 \cdot 10^{12}$  protons or low intensity of  $3 \cdot 10^{12}$  protons, remaining from not fully used proton bunches sent to other facilities (*parasitic*). The comparatively long time between pulses, dictated by the supercycle structure of the PS, is beneficial, since it guarantees that there will be no overlap between two consecutive neutron pulses, even for a long flight path and a large neutron energy range from meV to MeV.

The n\_TOF facility uses two different flight paths. The first was commissioned in 2001, with a length of approximately 185 m, ending in *Experimental Area 1* (EAR-1), while the second (EAR-2) started operation in 2014, built vertically above the spallation target at a distance of about 19 m [30]. The measurements in this work

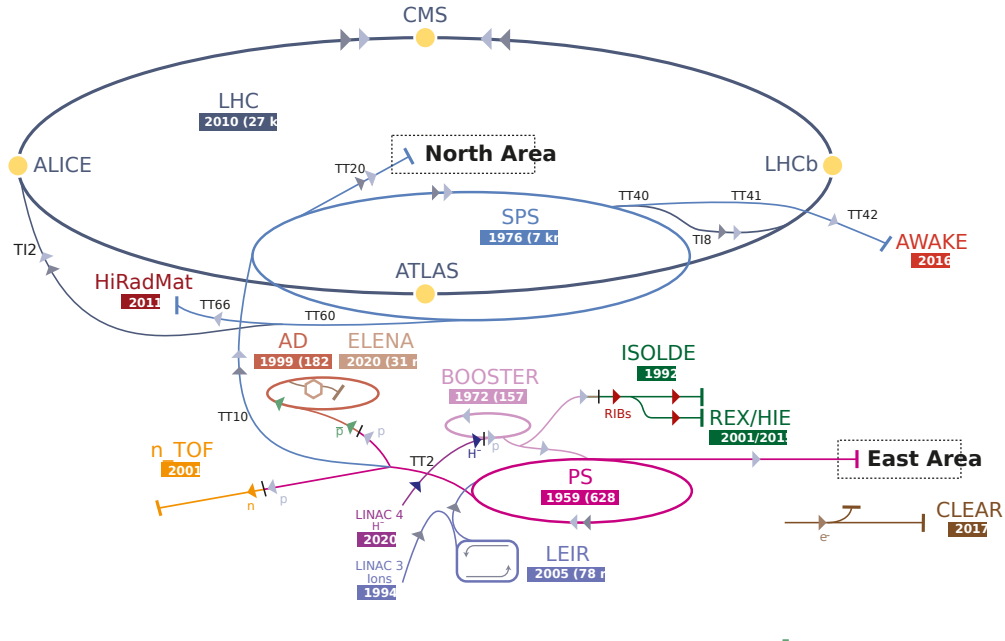
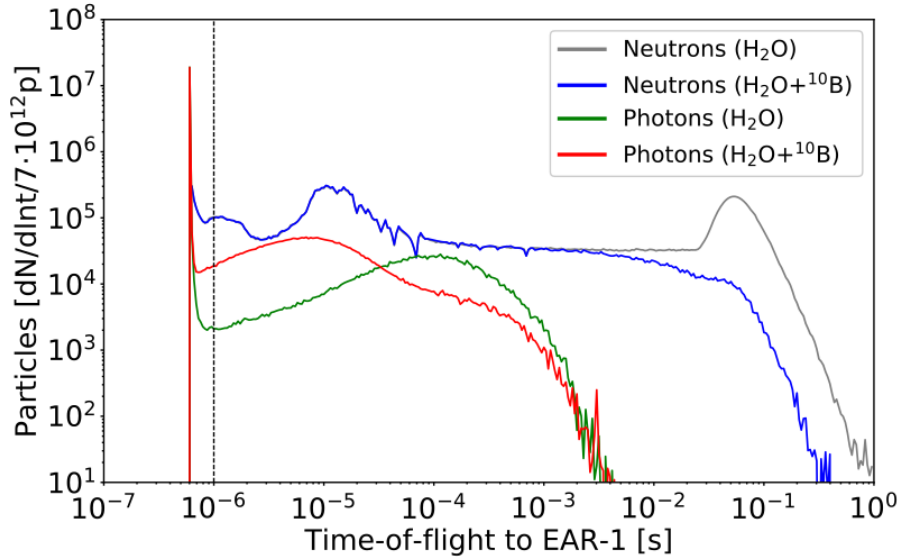


Figure 4.1.: Overview of the CERN accelerator complex, extracted from [31].

were performed during n\_TOF's *Experimental Phase 3*, which lasted from 2014 to 2018.

#### 4.1.1. Neutron production through spallation

The n\_TOF spallation target used during this measurement was in operation from 2008 to 2018. It consists of a cylindrical lead target with a diameter of 60 cm and length of 40 cm. The cylinder is surrounded by a 1 cm layer of water for cooling purposes, followed (along the relevant beam direction towards EAR-1) by 4 cm of borated water, which acts as a moderator [15, 32]. Each of the impinging high-energy protons creates around 300 fast spallation neutrons [32] in the lead cylinder. These are then partially moderated to extend the range of the neutron energy distribution down to the thermal region, creating a so called "white neutron source". The borated water additionally influences the shape of the low-energy neutron spectrum (Figure 4.2), as well as reducing the 2.223 MeV  $\gamma$ -ray background from neutron captures onto hydrogen (Figure 4.3) [29].



**Figure 4.2.:** Arrival time of in-beam photons, primarily from the spallation target, at EAR1, obtained from Monte Carlo simulations. The prompt component below  $10^{-6}$  s and delayed component above  $10^{-6}$  s can be observed. The addition of  $^{10}\text{B}$  to the moderator further reduces this background component for low neutron energies (extracted from [29]).

#### 4.1.2. The $\gamma$ -flash

Besides neutrons, the spallation process creates many other highly energetic particles, chiefly among them photons. While most charged particles produced in this way can be removed by sweeping magnets in the beamline, the same cannot be applied to the gamma rays and other uncharged particles. Their contribution to the background can be separated into the *prompt* and *delayed* component, as illustrated in Figure 4.2, which have both been studied in detail through Monte Carlo simulations [33].

The photons and other high-energy particles of the prompt component, also commonly called the  $\gamma$ -flash, arrive at EAR-1 after 617 ns, their travel time for the beamline length at the speed of light. They possess high energies, causing a large signal in and saturating the  $\gamma$ -ray detectors in the experimental area. The  $\text{C}_6\text{D}_6$  detectors used in this measurement typically return to the baseline signal after 3 ns, effectively providing an upper neutron energy limit of approximately 10 MeV for the detection of events. The  $\gamma$ -flash with its sharp onset is used both as a start signal for the time of flight calculation ( $t_\gamma$  in Eq.(2.25)) and for the calibration of the ToF to energy conversion (Section 5.3).

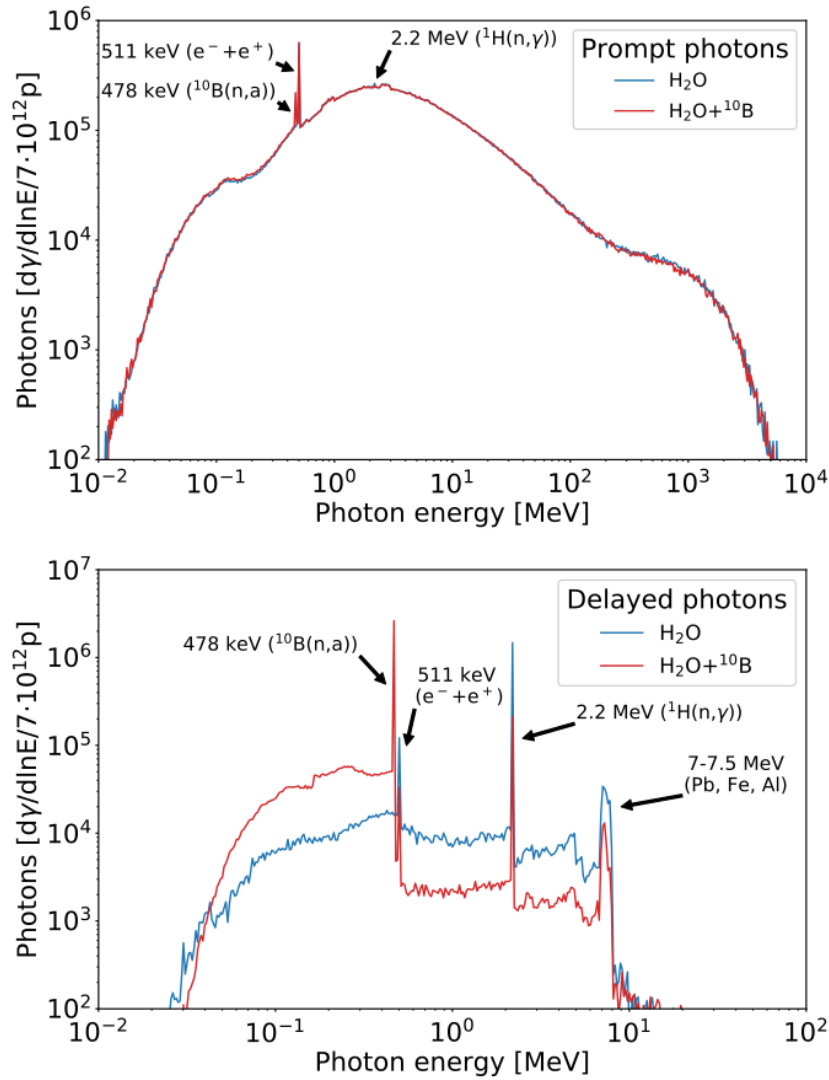


**Figure 4.3.:** Energy distribution of the in-beam prompt (top panel) and delayed (bottom panel)  $\gamma$ -ray background (extracted from [29]).

The delayed component originates from interactions of the initially produced neutrons and muonic atoms [34] with the moderator and beamline components (Figure 4.3), and subsequent emission of photons along the flight path into the experimental area. Since these particles are decoupled from the ToF to energy relation, they cannot be distinguished from capture events on the sample and removed from the data via a cut on the time of flight, effectively presenting a background component across a wide neutron energy range. The use of borated water shifts their distribution to lower photon energies, making it possible to exclude them by cuts on the data.

## 4.2. Experimental Setup

The capture setup in EAR-1 (Figure 4.4) is optimized to reduce the amount of neutron interactions with any materials besides the capture sample. All components in the direct vicinity (detectors, sample exchanger, beamline pipes) are primarily made out of carbon fiber, minimizing the amount of higher mass nuclei and probability of capture events. The main remaining background contribution are scattered neutrons, whose effect is explored in further detail in Section 2.3.3 and Section 5.5.

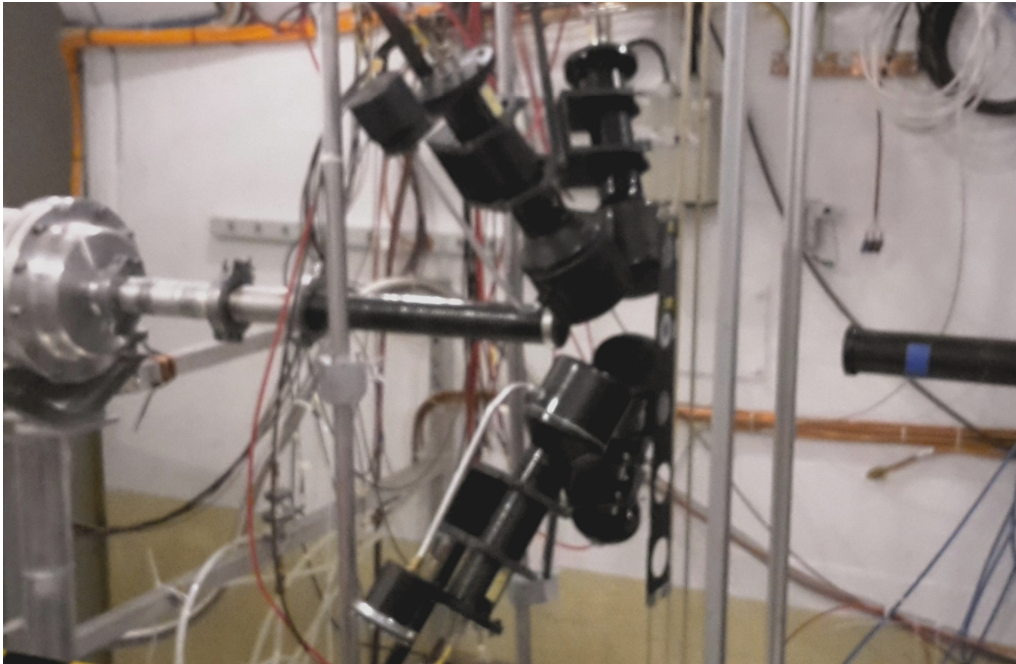


**Figure 4.4.:** The capture setup in EAR1. The neutron beam enters the experimental area from the left, and interacts with the sample in the sample exchanger. The four  $\text{C}_6\text{D}_6$  detectors are mounted at a backward angle.

The four  $\text{C}_6\text{D}_6$  detectors are positioned at a backward angle with regard to the neutron beam direction (Figure 4.4), reducing interactions with beam particles and reaction products that retain their forward momentum direction.

The sample exchanger (Figure 4.5) enables switching between different samples without having to access the experimental area, as well as the exact and reproducible positioning of multiple samples at the same position with respect to the neutron beam. The high positional accuracy ensures that even if there was a slight offset between the beam center and sample position, this offset would be identical between all samples, and cancel out in the analysis.

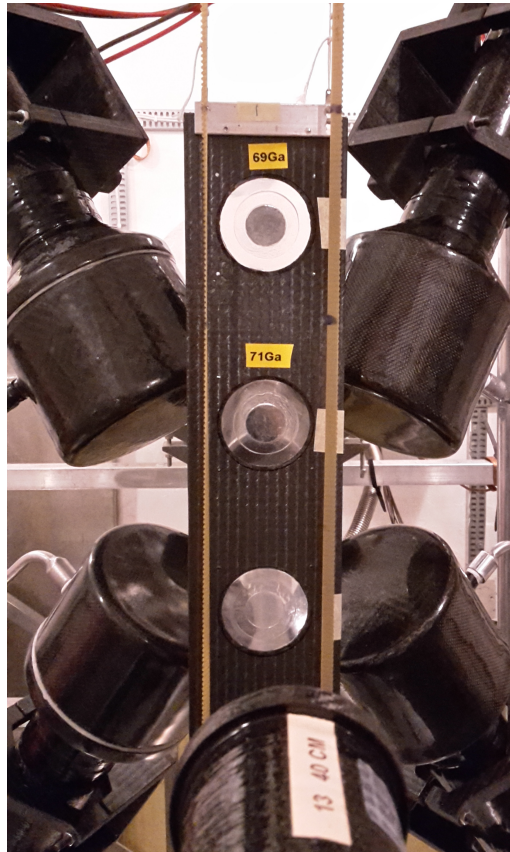


**Figure 4.5.:** The carbon fiber sample exchanger in EAR1, from a point of view facing upstream towards the neutron beam. Both gallium samples and the empty target frame are inserted.

#### 4.2.1. Beam position and profile

Several systems are used to focus the beam onto the capture position, and remove as many unwanted particles that were created alongside the neutrons in the spallation target or along the flight path. A first collimator removes the beam halo, followed by a sweeping magnet to remove any charged particles. In a last step, the small collimator with a diameter of 18 mm is used to shape the beam to the required size at the capture position.

The exact beam position is crucial to maximize the amount of neutrons the sample can interact with, while minimizing the interactions of the beam with surrounding materials. Figure 4.6 shows the simulated distribution around the beam center when using the small collimator, which again justifies the sample dimension with a diameter of 2 cm (Section 3).

Before the actual measurements started, a gafchromic film [35] was placed at the estimated beam position in the capture setup sample exchanger, and exposed to the neutron beam for about one day. It was scanned, and the contrast increased using a dedicated software, resulting in Figure 4.6. This allowed a correction of the capture position setting of the sample exchanger.

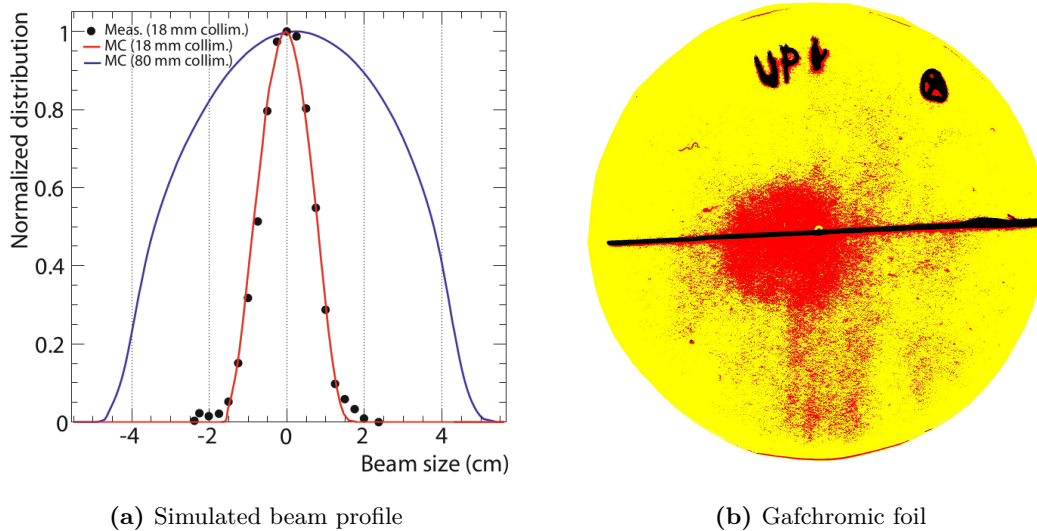


**Figure 4.6.:** Characterization of beam profile using the small collimator from simulations (left panel), extracted from [15]. The beam position was verified and adjusted using gafchromic foil (right panel).

#### 4.2.2. Auxiliary samples

Several additional samples were used for auxiliary measurements during the experimental campaign. All of them intentionally had the same diameter of 20 mm as the sample.

- Empty target: Identical to the  $^{69}\text{Ga}$  and  $^{71}\text{Ga}$  samples (Figure 3.2) in production and materials used, just lacking the gallium disc in the center. Its purpose was to determine background components from interactions of the beam with surrounding materials and the sample assembly, as well as electronic noise in the data acquisition. The only background components that cannot be estimated from this are caused by scattering or other secondary effects within the gallium samples.
- Gold: The sample (ID 157 in the  $n_{\text{TOF}}$  material database) is 0.1 mm thick, with mass 644.1 mg. It is mounted on a circular PCB frame, covered on each

side by 6  $\mu\text{m}$  Mylar foil. It is used to determine the total neutron flux, using the saturated resonance method (Section 5.7)

- Carbon: ID 107 in the database, with mass 2.646 g and 5 mm thickness. It is mounted on a circular Al support, and glued to 6  $\mu\text{m}$  Mylar foil on one side. Both the carbon and lead samples are used to estimate the contributions of scattering effects in the sample, as examples of low and high Z nuclei.
- Lead: ID 184 in the database, with mass 7.281 g and 2.1 mm thickness. It is mounted on a circular Al support, and glued to 6  $\mu\text{m}$  Mylar foil on one side.

### 4.2.3. Neutron flux

The neutron flux is a critical part of the neutron capture yield and cross section calculation (Eq.(2.11)). It does not suffice to just know the total number of neutrons, instead, its relative distribution across the neutron energy must be known as well. This is accomplished by using the previously measured flux profile (Figure 5.23) for this experimental area [36], and scaling it with a correction factor from the Saturated Resonance Method (further discussed in Section 5.7) on the well known 4.9 eV gold resonance.

There are several systems in place to monitor the proton and neutron beam. Given the large number of proton bunches over the course of the whole measurement, and the identical energy distribution of each produced neutron pulse, the proton and neutron numbers should on average have a constant ratio. Once this scaling factor has been determined, any of these relative parameters can be used to determine the absolute neutron flux at the sample, with the possibility of consistency checks between the monitoring systems across the duration of the entire experimental campaign.

- BCT: A Beam Current Transformator placed 6 m ahead of the spallation target. It provides the total number of protons in each pulse delivered from the PS, and gives the start signal for the n\_TOF data acquisition system.
- SiMon: A thin Mylar foil with a  $^6\text{Li}$  deposit is placed into the neutron beam, 1 m upstream of the capture position. The products of the  $^6\text{Li}(n,\alpha)^3\text{H}$  reaction are detected within four surrounding silicon detectors [37].



## 5.1. Detector calibration

The  $C_6D_6$  detectors, as described in Section 2.3.3, almost exclusively detect incident photons through Compton scattering interactions. Their channel to energy calibration must therefore be applied to the position of the Compton edge of the respective calibration source energy. The four sources used (Table 5.1) cover almost the complete expected energy range of this measurement, with  $^{69}Ga$  having the higher Q-value of 7.65 MeV.

The AmBe source contains  $^{241}Am$  as an  $\alpha$  emitter, which in turn react with  $^9Be$  via



Calibration source	$\gamma$ -energy [keV]	Compton energy [keV]
$^{137}Cs$	661.66	477.34
$^{88}Y$	898.04	699.13
	1836.06	1611.81
AmBe	4440	4198.40
CmC	6130	5884.72

**Table 5.1.:** Radioactive sources used for  $\gamma$ -energy calibration. The position of the Compton edge is determined from Eq.(2.29). Note that the  $^{88}Y$  source emits two distinct  $\gamma$ -rays in coincidence.

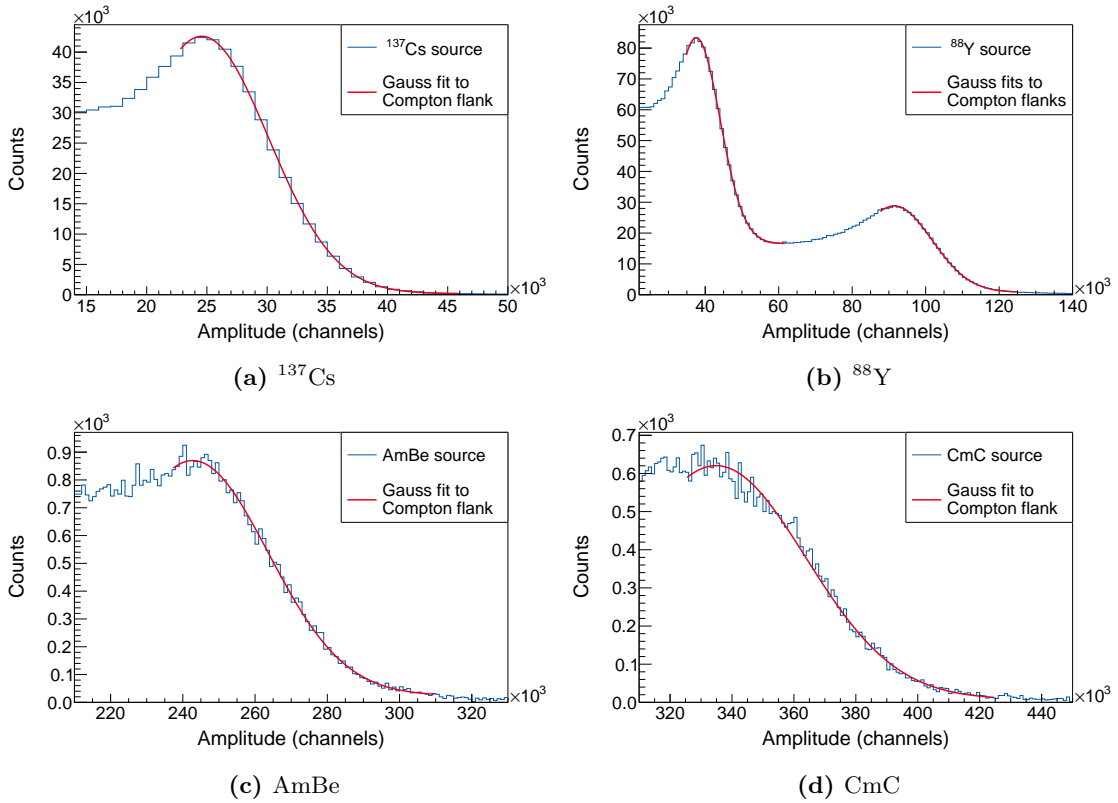


**Figure 5.1.:** Gaussian fit to calibration source Compton edges of detector 1. The channel at half maximum is used as input for the channel to energy fit. The width  $\sigma$  of the gaussian denotes the resolution (in channels) at this energy.

The excited  $^{12}\text{C}^*$  nucleus decays under emission of a 4.44 MeV  $\gamma$ -ray [38].

Similarly, the  $^{244}\text{Cm}$  in the CmC source emits an  $\alpha$ , which then reacts with the contained  $^{13}\text{C}$ :



The  $^{16}\text{O}^*$  nucleus has an excited state at 6.13 MeV, which directly decays to the ground state. It has a rather long half-life of 18.4 ps, avoiding any Doppler broadening of the emitted line [39, 40].

In order to determine the respective channels of the Compton energies, a gaussian fit was applied to the edges in the calibration source spectra (Figure 5.1). The channel corresponding to the mean  $\bar{x}$  plus half of the FWHM,  $\Delta x$  of each fit was used as data point for the respective Compton edge,  $x_{Comp}$

$$x_{Comp} = \bar{x} + \frac{\Delta x}{2}. \quad (5.3)$$

Several types of functions to describe and fit the channel to energy conversion are commonly used (linear, linear through zero, second order polynomial). The respective fits including error bars are compared in Figure 5.2. Since all three types of fit functions match the data points very well, with their ratios being very close to 1, the linear fit through zero was chosen as

$$E_\gamma(\text{channel}) = c_1 \cdot \text{channel}. \quad (5.4)$$

It should remain numerically stable beyond the highest calibration source energy, and matches the expected physical behaviour of the detectors by intercepting the origin.

The  $\gamma$ -energy resolution  $r$  of each detector can also be determined from the Gaussian fit to the calibration source spectra (Figure 5.1).

Herein, half of the full width at half maximum, in calibrated energy, is taken as the broadening of the theoretically vertical Compton edge at that energy:

$$r(E) = \sqrt{2 \ln 2} \cdot \sigma(E), \quad (5.5)$$

with the standard deviation of the Gaussian fit  $\sigma(E)$  at energy  $E$ . Two possible functions to fit the energy resolution were considered,  $k \cdot \sqrt{E}$  and  $k_1 \cdot \sqrt{E} + k_2 \cdot E$ . Figure 5.3 shows that the latter provides a much better fit to the data points, and was therefore selected.

## 5.2. Detector consistency

### 5.2.1. Neutron beam monitors

Beam monitors (Section 4.2.3) are used to determine the integrated neutron flux, either directly (SiMon) or indirectly through the proportional number of protons on the spallation target(BCT). This flux is used for normalising the counting rate spectra

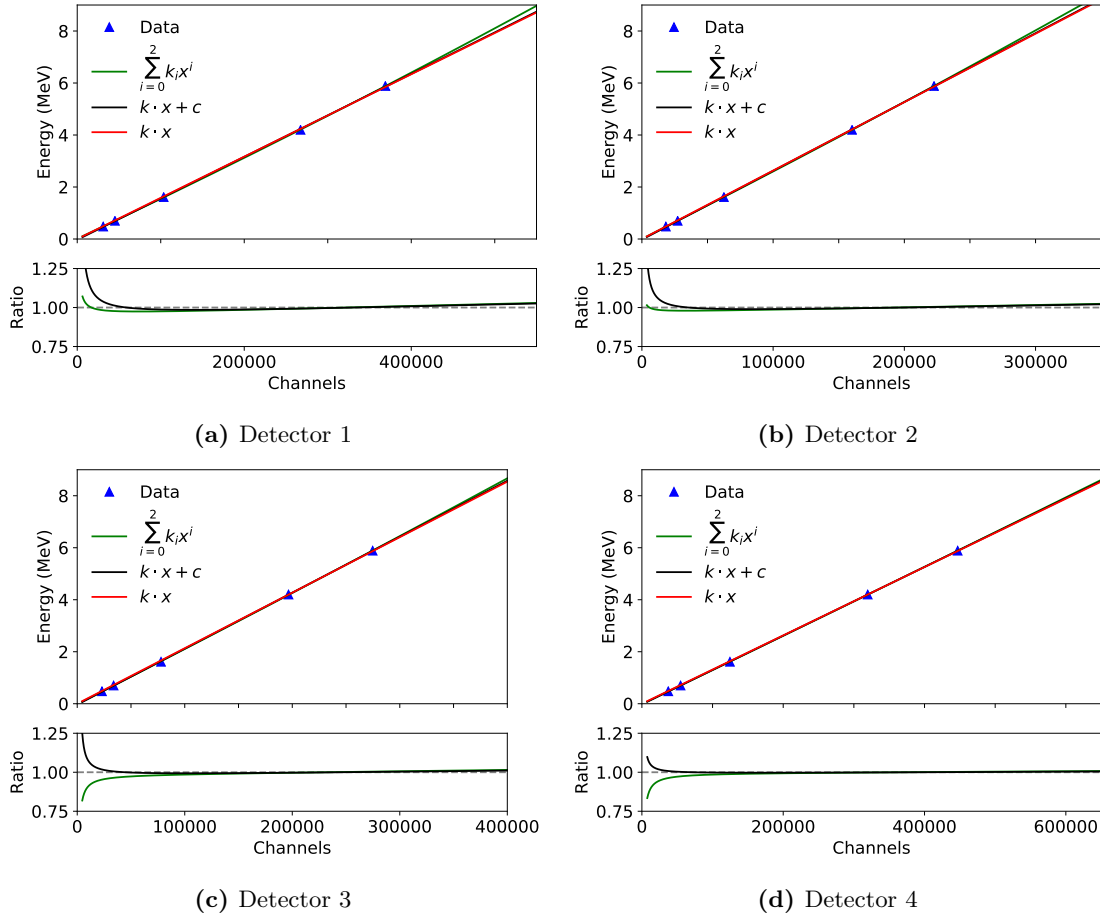


**Figure 5.2.:** Channel to energy conversion from calibration source data. The lower panels show the respective ratios of the quadratic (green) and linear (black) fit to the ultimately chosen linear fit through the origin (red).

for background subtraction, and later in the yield and cross section calculation. Their consistency across the duration of the experimental campaign needs to be checked.

To that end, the ratio between protons on target and integrated counts of the SiMon (SILI) detectors were determined for each measured sample ( $^{69}\text{Ga}$ ,  $^{71}\text{Ga}$ ,  $^{197}\text{Au}$  and empty target sample, used for background subtraction). This ensures no systematic deviations between the normalization of the different samples. Figure 5.4 shows the ratios of the four individual SiMon detectors to the protons on target for each  $^{69}\text{Ga}$  run, normalized with the average across all runs. One of the SILI detectors shows large deviation from the expected values close to unity, and was therefore excluded from the analysis. By the same approach, individual runs for each sample that showed the largest deviations (between run 14 and 19 in the figure on the top)

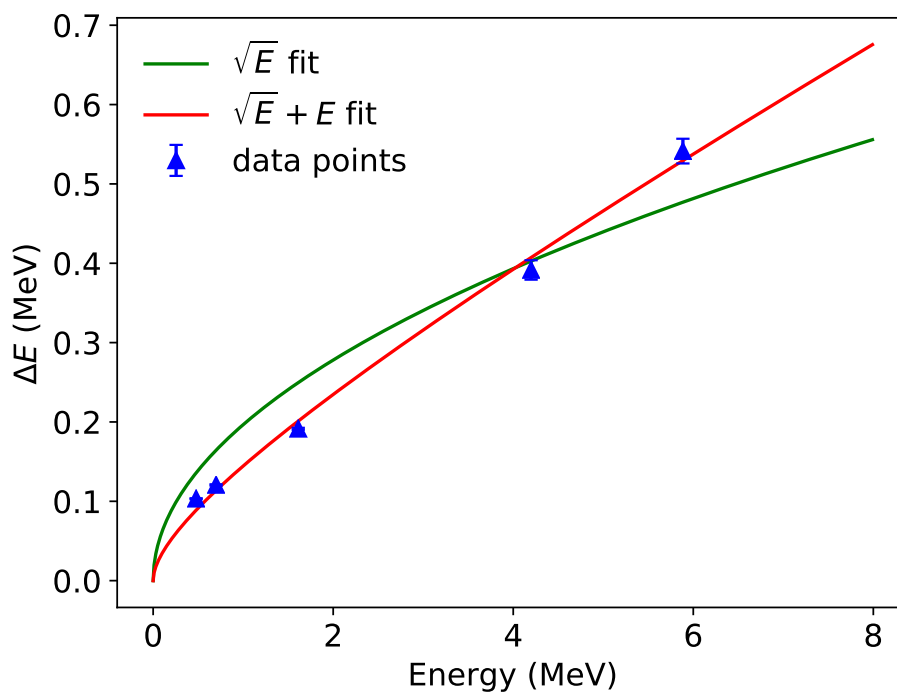
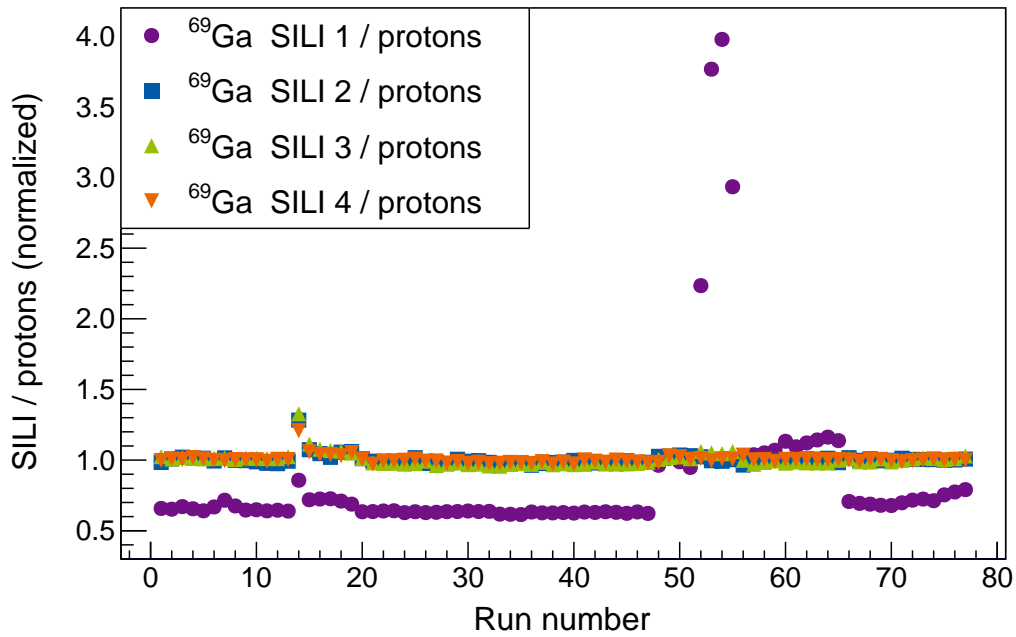
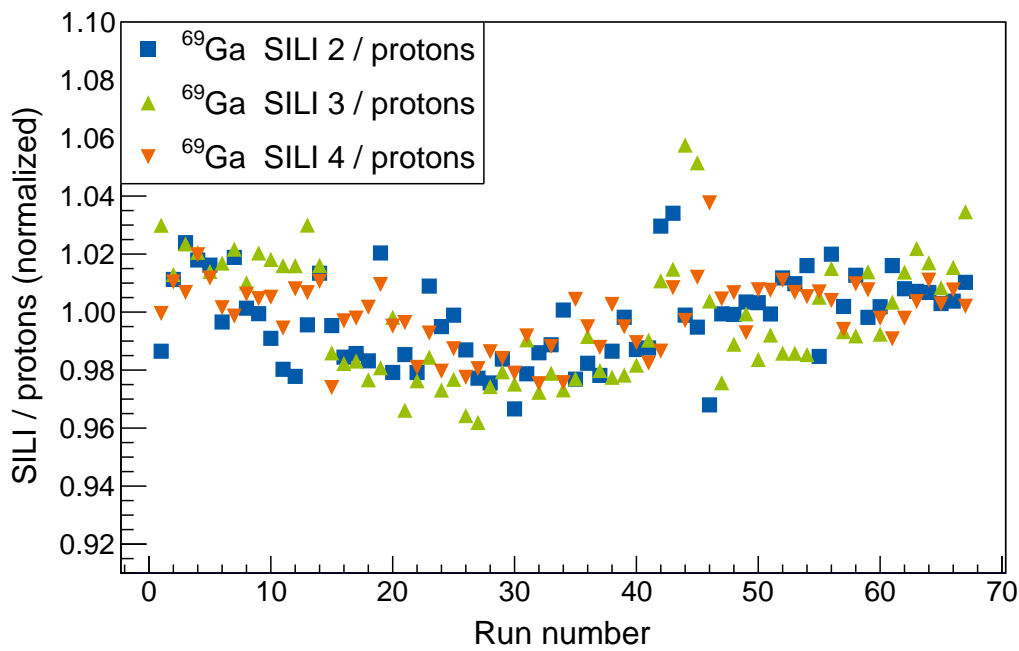


**Figure 5.3.:** Fit of the energy resolution, derived from the broadening of the Compton edges of the calibration source data. The  $\sqrt{E} + E$  fit was chosen due to its much better agreement with the data.

were identified and excluded from the final analysis. The figure in the bottom shows the expected good agreement of the remaining runs.



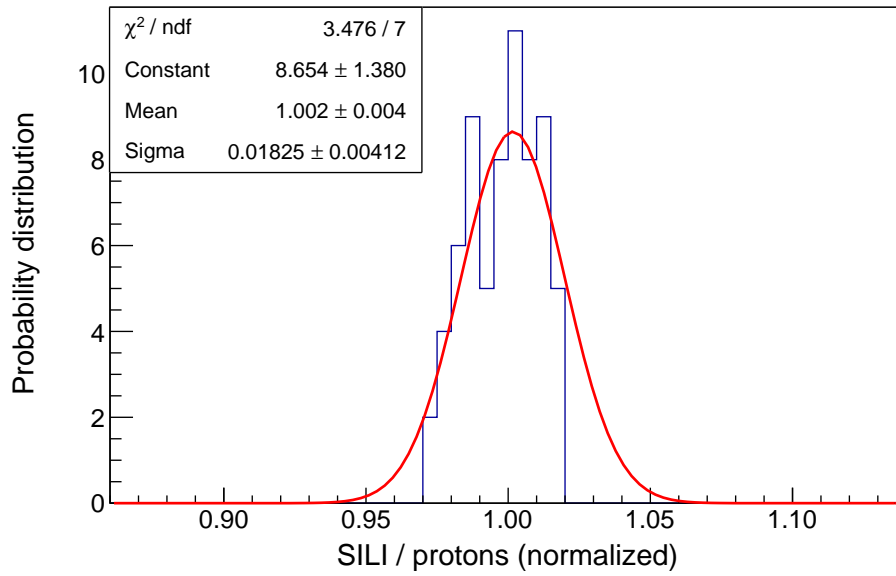
(a) Ratios for 4 SILI detectors



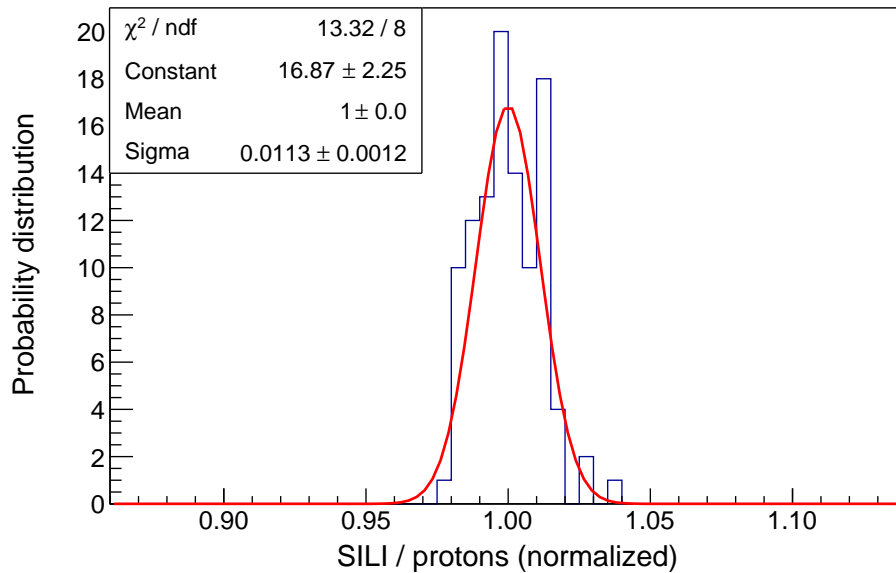
(b) Ratios for 3 SILI detectors

**Figure 5.4.:** Ratios of beam monitor counts across all  $^{69}\text{Ga}$  runs, normalized to the respective average across all runs. One SILI detector showed large deviations (top) and was removed from the analysis (bottom).

The distributions of normalized beam monitor ratios for all selected runs of each gallium sample are displayed in Figure 5.5. The Gaussian fits through them show the uncertainty in the beam monitor stability to be  $\leq 2\%$ .



(a) Ratio distribution for  $^{69}\text{Ga}$  runs.



(b) Ratio distribution for  $^{71}\text{Ga}$  runs.

**Figure 5.5.:** The distribution of normalized beam monitor ratios of both gallium samples for all runs that were used in the analysis. The Gaussian fits through the distributions show variations  $\leq 2\%$ .

### 5.2.2. $C_6D_6$ stability

One important quality check during the experiment is the gain stability of the detectors. Changes in the detector gain for a given energy have a linear correlation with the weighted counts derived from the pulse height weighting (Section 5.6) [41].

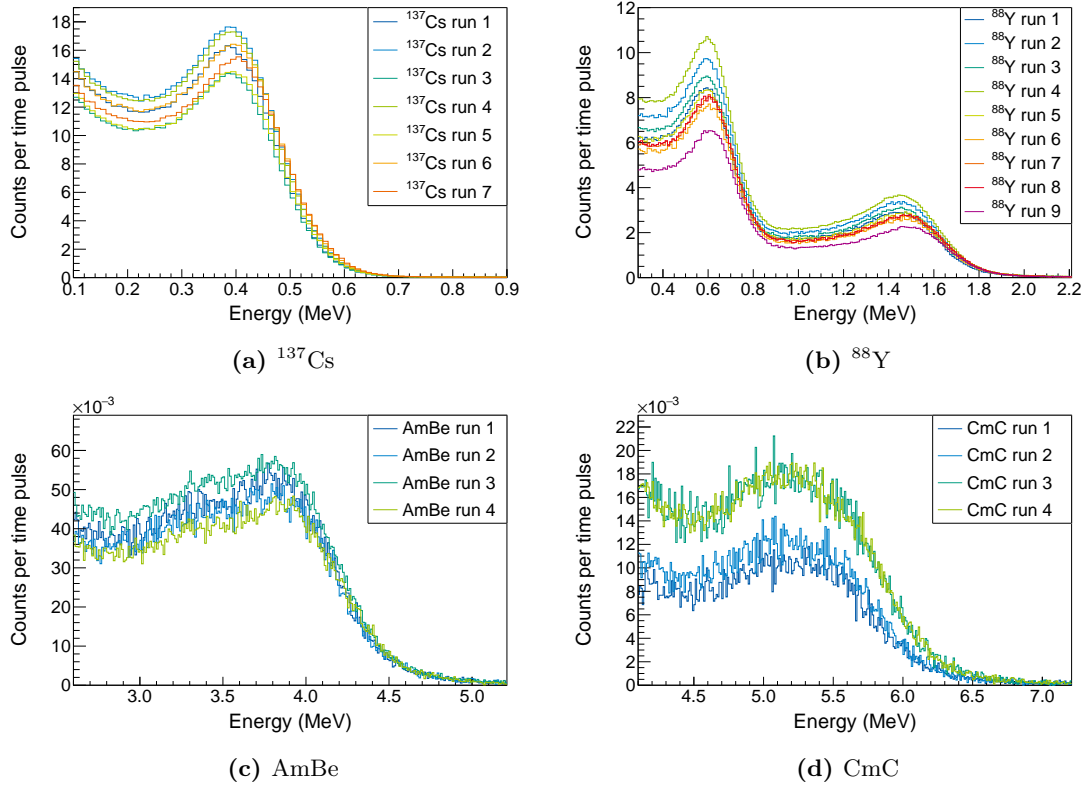


**Figure 5.6.:** Calibrated amplitude spectra of detector 1 for several calibration measurements across the whole campaign, normalized to the respective measurement times. The relevant Compton edges remain at the same x-position, indicating stability of the detector gain over time. The differences in normalized counts are discussed in the text.

Measurements with all calibration sources were performed in weekly intervals across the whole experimental campaign to determine possible changes in the detector gain, meaning that the same deposited  $\gamma$ -energy would cause different voltage outputs of the detector and be attributed to different channels in the data acquisition. This was checked with the position of the Compton edges of the sources in Figure 5.6.

Since the half lives of the used calibration sources are significantly longer than the duration of the experimental campaign, the number of events per detector after normalizing for each measurement duration should be the same for all calibration measurements with a source. In contrast, Figure 5.6 shows deviations in the am-



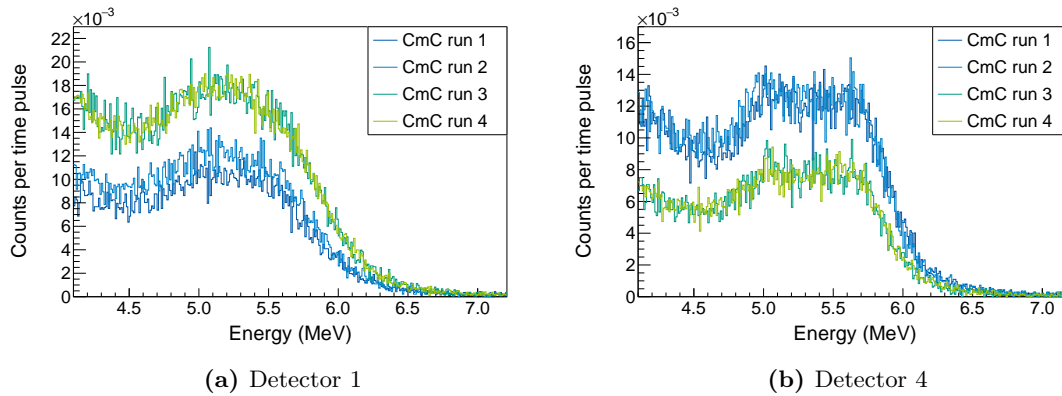


**Figure 5.7.:** Comparison of the CmC runs for detectors 1 and 4. A clear switch between the count rates in the detectors for respective runs can be observed here, and in many other cases (Figure A.4), making the positioning of the calibration source the most likely explanation.

plitudes of all sources and detectors. However, two important observations can be made:

- There is no continuous trend across time for the increase or decrease of count rate in any detectors. This makes it unlikely that a continuous change in the detection efficiency took place, see also Figure 5.7.
- Furthermore, certain correlations and anticorrelations when comparing pairwise runs between different detectors can be observed (Figure 5.7).

When keeping in mind both the dimensions of the calibration sources (Figure A.1) and the large variation of the sample position by attaching the calibration source holder by hand without a reference frame for each calibration measurement, these observations in all likelihood do not indicate a change in detector efficiency across the campaign and can be ignored.

To demonstrate the gain stability of the detectors, the spectra were normalized to the integral in the relevant region around the Compton edge, instead of the measurement duration. Figure 5.8 shows the good agreement of the Compton edge position between all measurements for detector 1, with the other 3 detectors showing the same agreements (Figure A.6), so the determined channel to energy conversion formulas can be applied to all runs of the measurement.

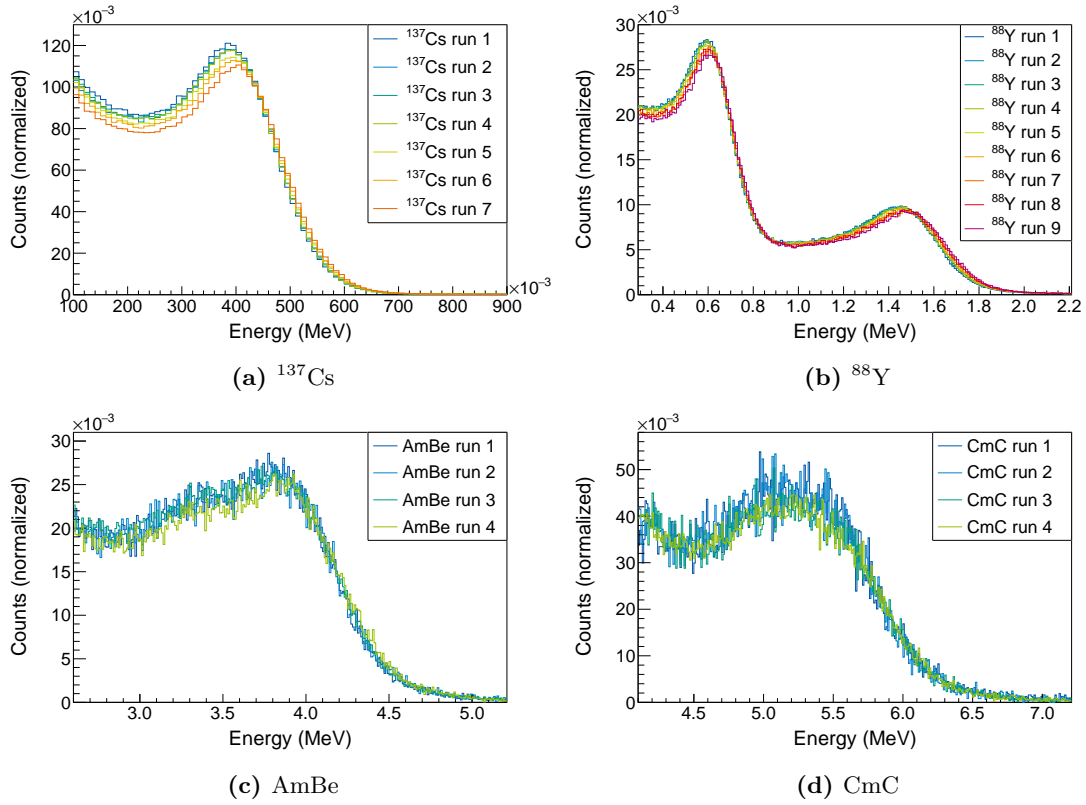


**Figure 5.8.:** Calibration source measurements across experimental campaign for detector 1, normalized to number of counts. The good agreement of the calibrated Compton edge positions can be clearly observed.

### 5.3. ToF to energy conversion

The calculation of a differential cross section for the neutron capture reaction requires the transformation of the time of flight data into the corresponding neutron energy. Eq.(2.25) describes the general calculation, however, there are a few additional effects that need to be considered:

- The width of the proton beam of 7 ns rms [29, 30]. This effect cannot be compensated for, and provides a lower bound for the time resolution  $\Delta t$ .
- The moderation of neutrons in and around the spallation target (Section 4.1.1) increases their total distance traveled (*moderation distance*). This results in both a broadening of the time-of-flight distribution, and a systematic shift towards lower neutron energies. The moderation distance increases with neutron energy, which can be expressed as a time equivalent constant offset  $t_t$  [42].

Resonance energy [keV]	ToF position [ns]	Resonance energy [keV]	ToF position [ns]
60.291	$1.714 \cdot 10^6$	864.277	$4.522 \cdot 10^5$
78.501	$1.502 \cdot 10^6$	879.536	$4.483 \cdot 10^5$
107.033	$1.286 \cdot 10^6$	1092.610	$4.021 \cdot 10^5$
144.410	$1.107 \cdot 10^6$	1207.240	$3.826 \cdot 10^5$
151.393	$1.081 \cdot 10^6$	1450.360	$3.489 \cdot 10^5$
190.032	$9.651 \cdot 10^5$		

**Table 5.2.:**  $^{197}\text{Au}$  resonances and corresponding time of flight positions used for flight path length and moderation distance fitting.

- The time response of the detectors, leading to a broadening of the time-of-flight distribution. Figure 5.10 shows the distribution of the  $\gamma$ -flash events in time, with a width of approximately 7 ns, which is the width of the incident proton pulse. This means that there is no noticeable broadening due to the time response of the detectors, which can therefore be neglected.

Including the moderation distance extends Eq.(2.25) to

$$tof_n = t_d - t_\gamma - t_t + \frac{L}{c}. \quad (5.6)$$

The parameters  $L$  and  $t_t$  can be determined by matching well known resonances to their corresponding time of flights in the data. This was done for the  $^{197}\text{Au}$  data, using resonances from [43] in the 100 eV and 1 keV region (Table 5.2). These were fitted using Eq.(5.6) to determine the two fit parameters  $L = (184.147 \pm 0.026)$  m and  $t_t = (-24.502 \pm 55.099)$  ns, see Figure 5.9. These uncertainties of the individual parameters do not yet take into consideration their correlation and the total uncertainty of the neutron energy calculation from the time of flight values, which will be further discussed in Section 5.8 and Section 6.2.

## 5.4. Dead time correction

Detector dead time is an effect where two signals occur in the detector within a certain time interval  $\tau_d$ , but cannot be distinguished as two individual signals. The literature [19] describes two different models to characterize the dead time behaviour of a system:

- In a *paralyzable* system, the second signal overlaps with the first one, extending the dead time.

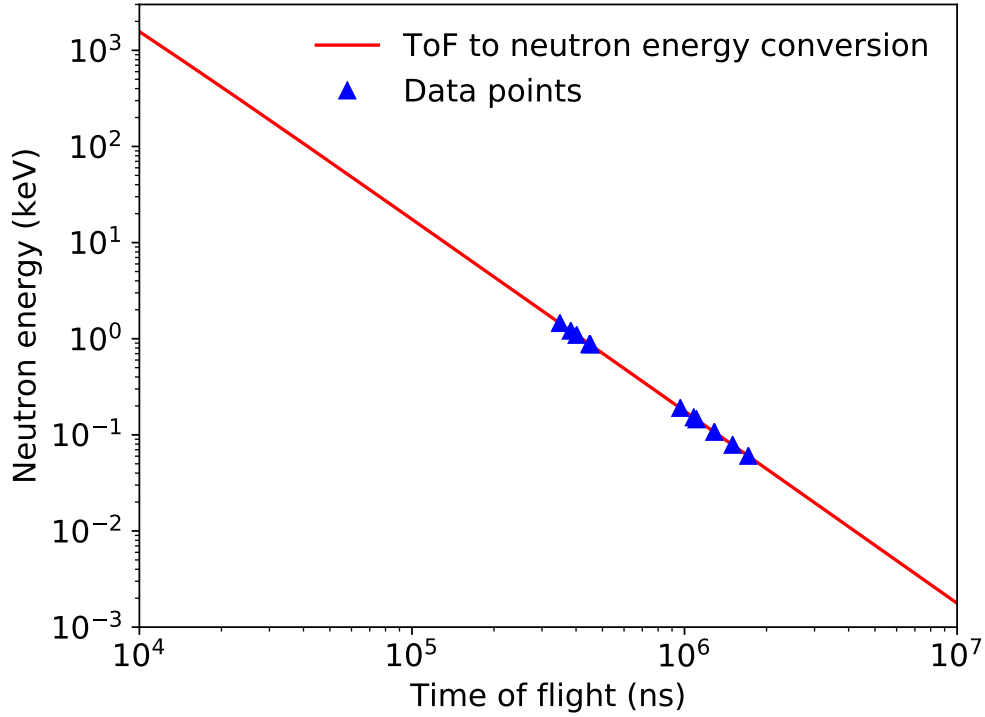


**Figure 5.9.:** Fit through  $^{197}\text{Au}$  resonances, using Eq.(5.6). The uncertainties of the determined neutron energies are  $< 1\%$  and therefore too small to properly display in the figure.

- In a *nonparalyzable* system, on the other hand, the detector is completely blind for the occurrence of the second signal within the dead time duration of the first.

This leads to two different relations between the recorded counting rate  $C_{det}$  and the true interaction rate  $C$ . For the nonparalyzable model, we get

$$C = \frac{C_{det}}{1 - C_{det}\tau_d}, \quad (5.7)$$

and for the paralyzable model, which is the case for the used detection system,

$$C_{det} = C \cdot e^{-C\tau_d}. \quad (5.8)$$

Fortunately, for low counting rates  $C \ll 1/\tau_d$ , which holds true for this detector setup and measurement, both Eq.(5.7) and Eq.(5.8) can both be approximated by

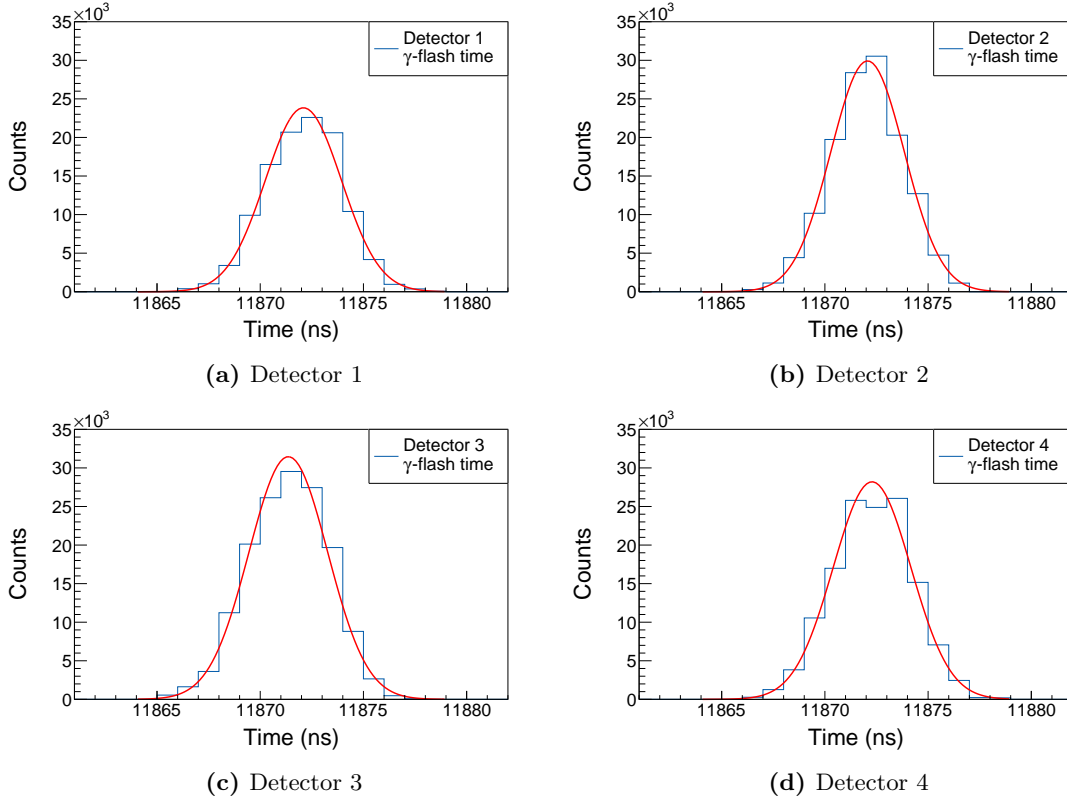


**Figure 5.10.:** Distribution of time of flight values of the  $\gamma$ -flash for  $^{69}\text{Ga}$  and parasitic bunches. The width of the distribution is of similar scale as the width of the proton pulse, with a standard deviation of the Gaussian fit through the distribution of  $\leq 2$  ns. This implies that there are no additional broadening effects in time due to detector time resolution.

$$\text{Nonparalyzable } C_{det} = \frac{C}{1 + C\tau_d} \cong C(1 - C\tau_d), \quad (5.9)$$

$$\text{Paralyzable } C_{det} = C \cdot e^{-C\tau_d} \cong C(1 - C\tau_d),$$

so Eq.(5.7) can be used for the dead time correction of the data, using the correction factor  $f_{dt}(E_n) = \frac{1}{1 - C_{det}(E_n)\tau_d}$  in

$$C(E_n) = f_{dt}(E_n)C_{det}(E_n). \quad (5.10)$$

Now all that remains to be determined is the dead time  $\tau_d$  of the system itself. To that end, the distribution of the time difference  $\Delta t$  between consecutive events in each detector was shown in Figure 5.11. The lack of any entries below and sharp rise

towards 20 ns gives the value  $\tau_d = 20$  ns for the calculation of the deadtime correction factor  $f_{dt}(E_n)$  in Figure 5.12.

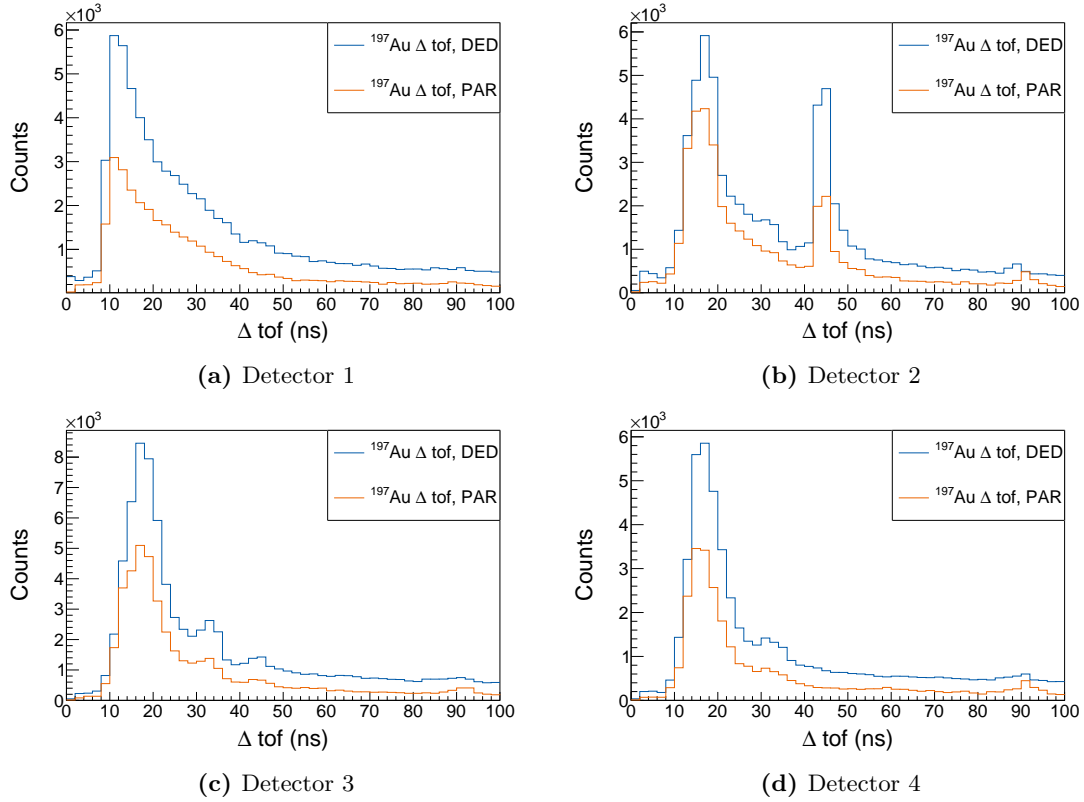


**Figure 5.11.:** Distribution of time difference between consecutive events for  $^{197}\text{Au}$  data in each  $\text{C}_6\text{D}_6$  detector, with a clear lower bound at 20 ns. A rebound signal is noticeable, especially in detector 2.

In the consecutive event distributions, especially in detector 2, a second peak at  $\Delta t \approx 45$  ns can be observed. Since the independent capture events should follow an exponentially decreasing Poisson distribution, further investigation of this signal, which can be seen in all detectors and for all samples to different degrees, was performed. The fact that they occur for all samples, including the empty sample, at exactly the same  $\Delta t$ , certainly excludes the deposition of photons from physics effects as a cause; instead, the most likely explanation are signal rebound effects within the detector itself.

To identify a possible correlation between the respective first and second signals leading to the peak, the energy distribution of all signals within a  $\Delta t$  window of 42 ns - 48 ns was plotted in Figure 5.13.

There appears to be no correlation between the events, and thus no way of removing them specifically with a combined cut on  $\Delta t$  and ratio of deposited energies. Therefore

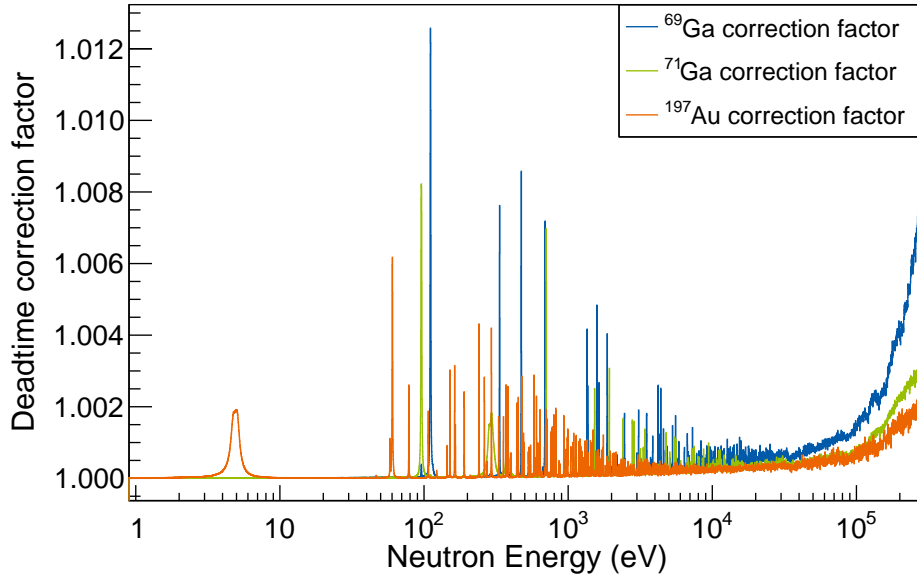


**Figure 5.12.:** Neutron energy dependent dead time correction factors  $f_{dt}(E_n)$  for  $^{69}\text{Ga}$ ,  $^{71}\text{Ga}$  and  $^{197}\text{Au}$  data, for a fixed dead time of 20 ns. The impact of the correction increases for higher neutron energies, which translates to smaller times of flight.

the decision was made to set a cut of 100 keV on the deposited energy in all detectors. Most of these low-energy events originate from background effects, and would therefore be eliminated during the background subtraction in any case. Additionally, due to the efficiency correction using pulse height weighting (Section 5.6), the relative number of counts of events with low deposited energy is strongly reduced in any case, so the application of this cut was approximated by a 5% uncertainty on the count statistics.

## 5.5. Background subtraction

There are several contribution to the experimental data that do not originate from neutron capture events onto the sample, but other effects that lead to energy depositions in the  $\text{C}_6\text{D}_6$  detectors. An important part of the analysis is the determination and subtraction of these background components, mainly through auxiliary measurements.

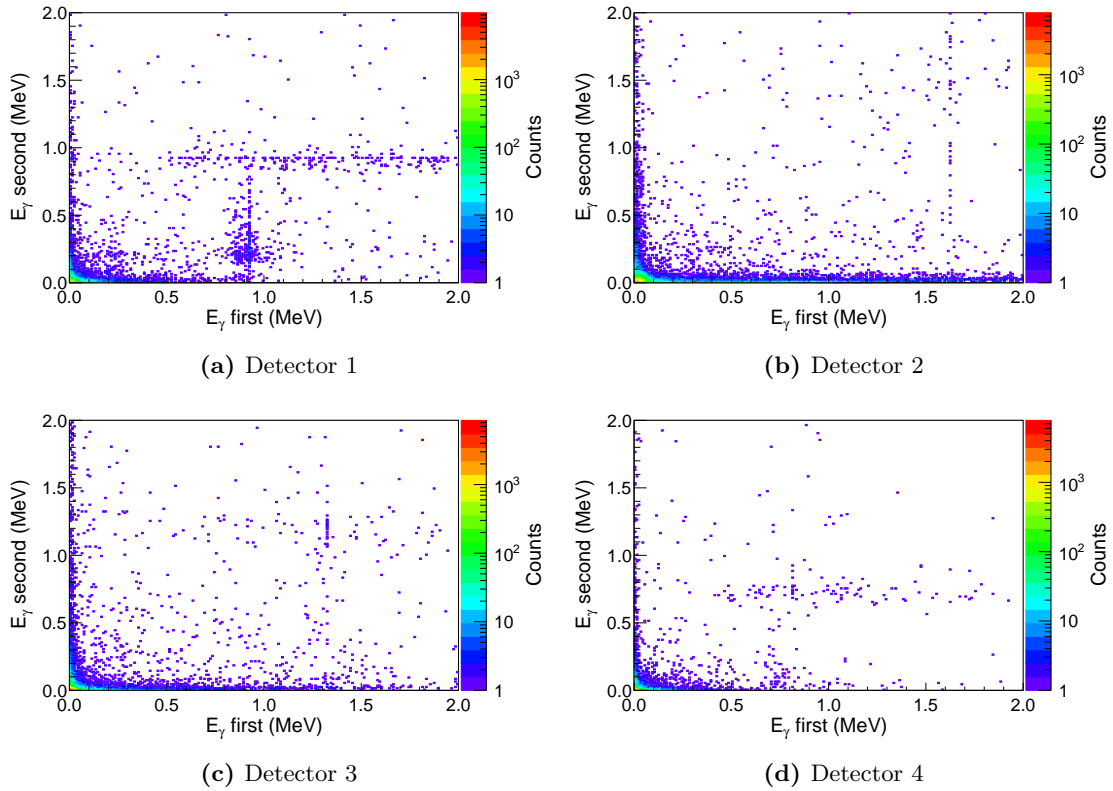


**Figure 5.13.:** Deposited  $\gamma$ -energy for the example of  $^{69}\text{Ga}$  events in the  $\Delta t$ -window of interest. No correlation between the first and second event's energy can be seen, making it impossible to remove the rebound signals through cuts on such a correlation.

### 5.5.1. Ambient component

The ambient or beam off component is caused by surrounding effects which occur even when the beam is turned off. Among these are activated samples and setup components, as well as environmental background. All those signals occur at a constant rate, and therefore need to be scaled with time to properly subtract them from the experimental data. This also justifies the separate treatment of dedicated and parasitic bunches in the analysis up to this point, since the two types of pulses have the same duration, but different neutron fluxes. Figure 5.15 shows that once the time-scaled ambient background component has been subtracted, the data from dedicated and parasitic pulses show good agreement. The ambient background was therefore subtracted from all other sample data, including the empty sample.

The ambient background, when converted into equivalent neutron energy, is the dominant component in the low eV range (Figure 5.16).



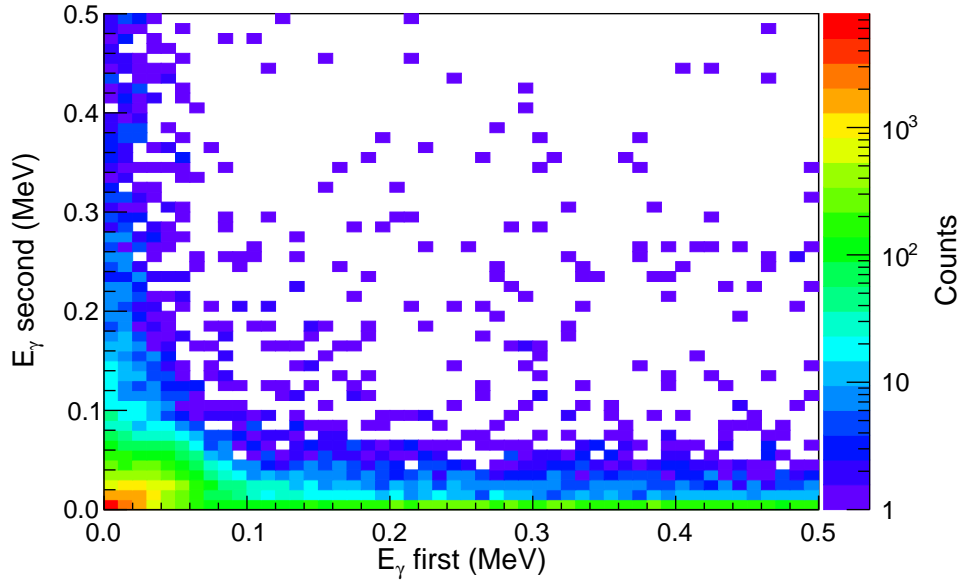


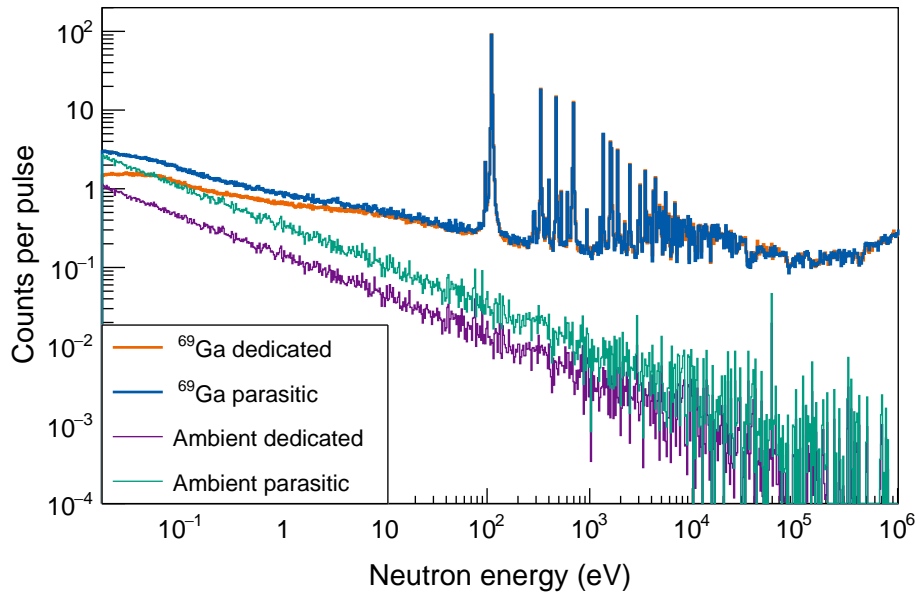
**Figure 5.14.:** Zoom on low energy region of the  $^{69}\text{Ga}$   $\Delta t$ -window for detector 2, which had the strongest rebound effects. A  $\gamma$ -energy threshold of 100 keV would remove the majority of these rebound and other background effects, and was therefore applied to all data.

### 5.5.2. Beam related component

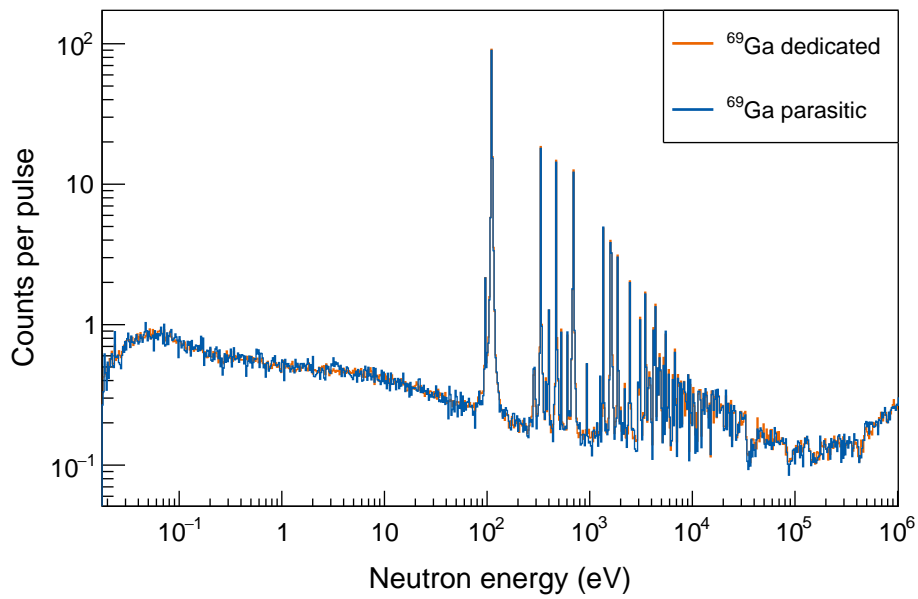
The empty or dummy sample (Section 4.2.2) reproduces all neutron beam induced background which was created independently of the gallium samples. These originate mainly from neutrons and  $\gamma$ -rays scattering in the beam line, vacuum windows and the sample frame itself, including the PVC ring right around the gallium samples.

The empty background component subtraction is performed by scaling the spectra to the number of protons on target, which is equivalent to the integrated number of neutrons.

Especially at higher energies in the keV range (Figure 5.16), the empty background component is a significant fraction of the total counts, meaning that its subtraction results in a non-negligible worsening in count statistics.



(a) Gallium data before ambient background subtraction, and ambient background components.



(b) Gallium data after ambient background subtraction.

**Figure 5.15.:** Comparison of normalized  $^{69}\text{Ga}$  weighted count histograms from dedicated and parasitic pulses before (top) and after (bottom) ambient background subtraction. After the removal of this component, which scales with time instead of number of incident neutrons, the data for both pulse intensities show good agreement.

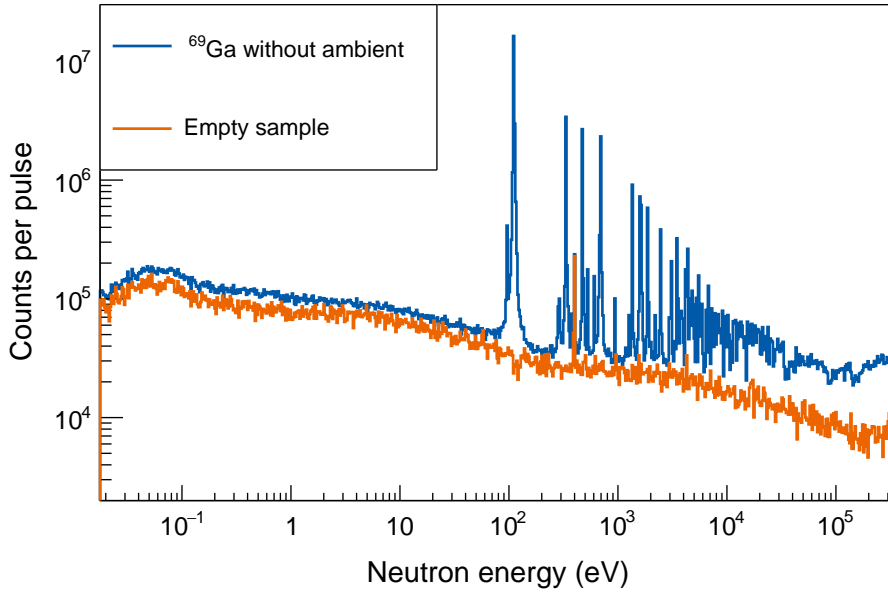


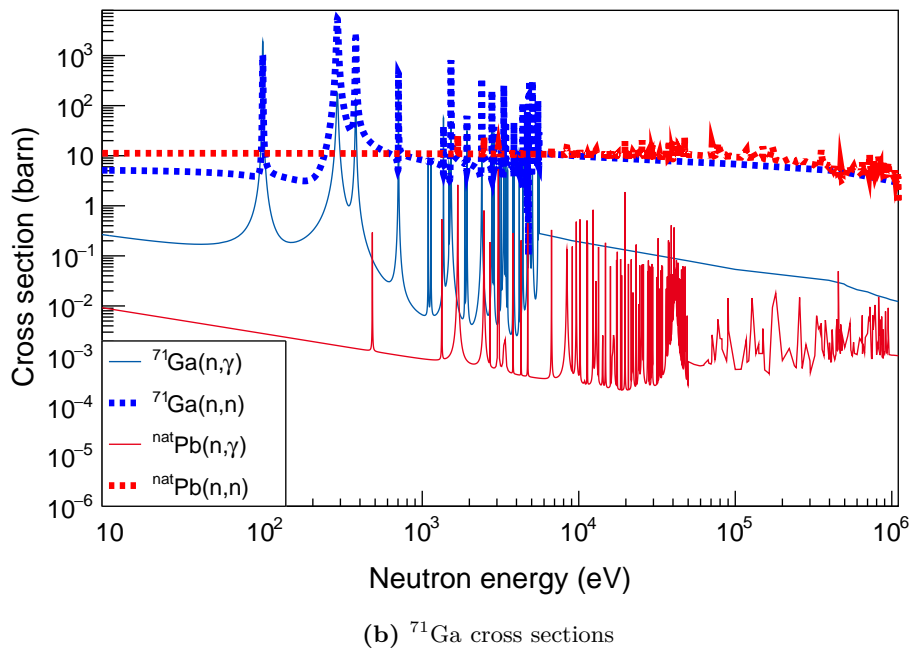
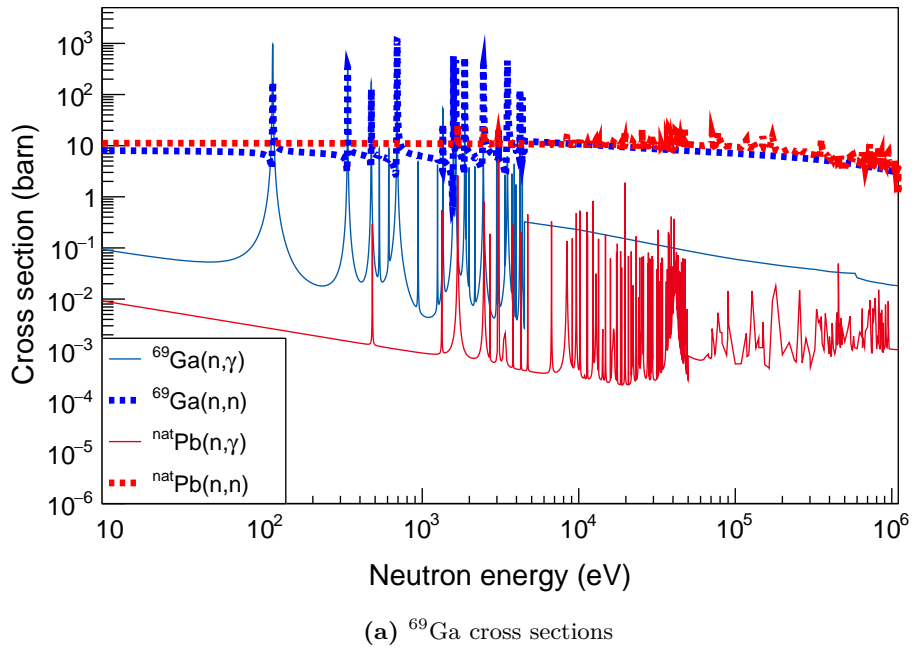
**Figure 5.16.:** Comparison of weighted  $^{69}\text{Ga}$  count spectra with the empty sample, normalized to nominal pulses. The empty sample data are used to subtract all beam-on background effects that do not originate from the sample itself, like interactions of the neutron beam with the sample frame and detection setup.

### 5.5.3. Scattering component

The next background component to consider is caused by neutrons which undergo elastic scattering in the gallium samples, and are then captured in the  $\text{C}_6\text{D}_6$  material or surrounding experimental area.

These scattering effects cannot be directly measured, instead, data from measurements with a  $^{nat}\text{Pb}$  sample (Section 4.2.2) are used for an estimation. Figure 5.17 shows the motivation for this approach, as lead with its high atomic number predominantly interacts through scattering. The neutron elastic scattering and capture cross sections were taken from [43]. For the  $^{nat}\text{Pb}$  sample, the individual cross sections for all stable Pb isotopes were averaged according to their mass fractions.

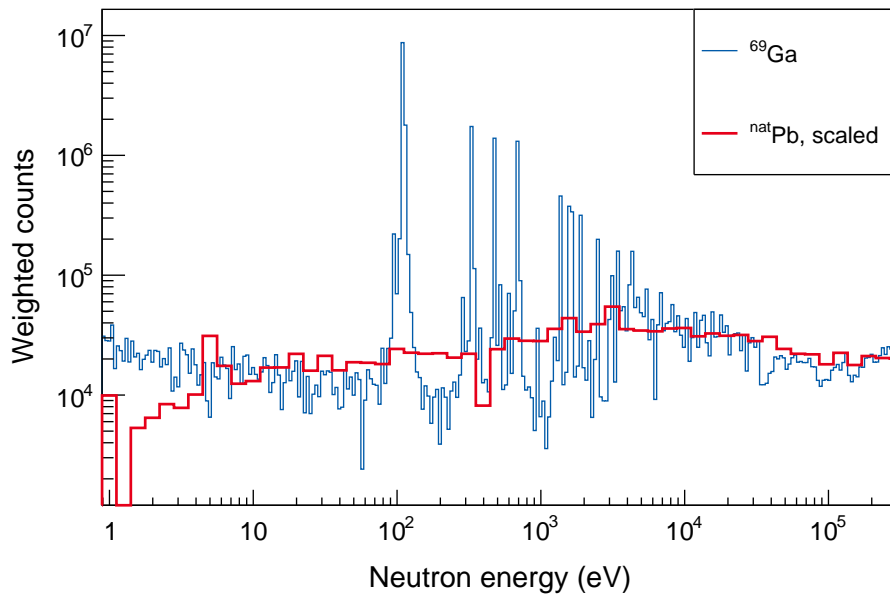
It is apparent from Figure 5.17 that  $^{nat}\text{Pb}$  has a much larger scattering to capture cross-section ratio, when compared with the gallium isotopes, by about 1 to 2 orders of magnitude. The  $^{nat}\text{Pb}$  data were scaled to the  $^{69}\text{Ga}$  data by number of protons and number of atoms in the respective samples in Figure 5.18. When combining the low neutron sensitivity  $\varepsilon_n/\varepsilon_\gamma \approx 3 \cdot 10^{-5}$  of the  $\text{C}_6\text{D}_6$  detectors (Section 2.3.3), coupled with the aforementioned smaller scattering to capture cross-section ratio of



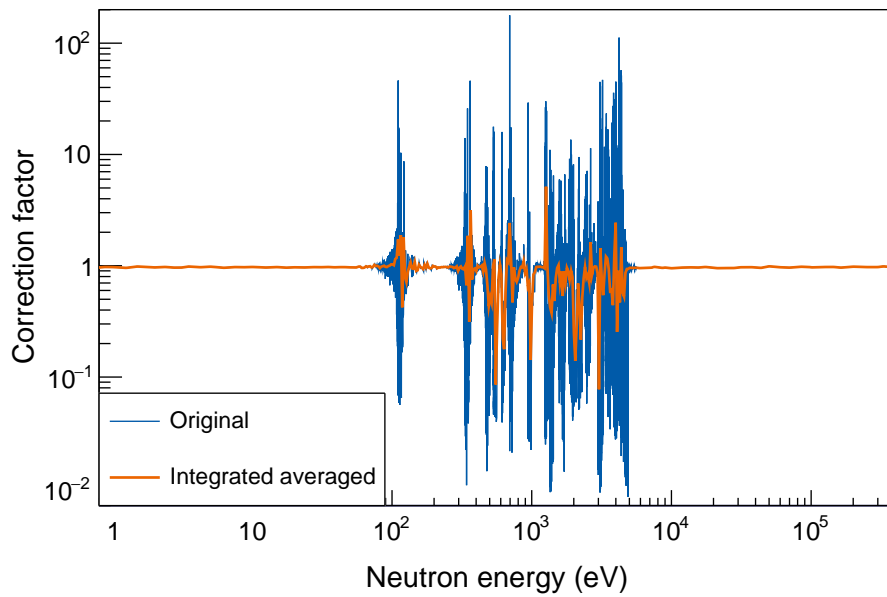
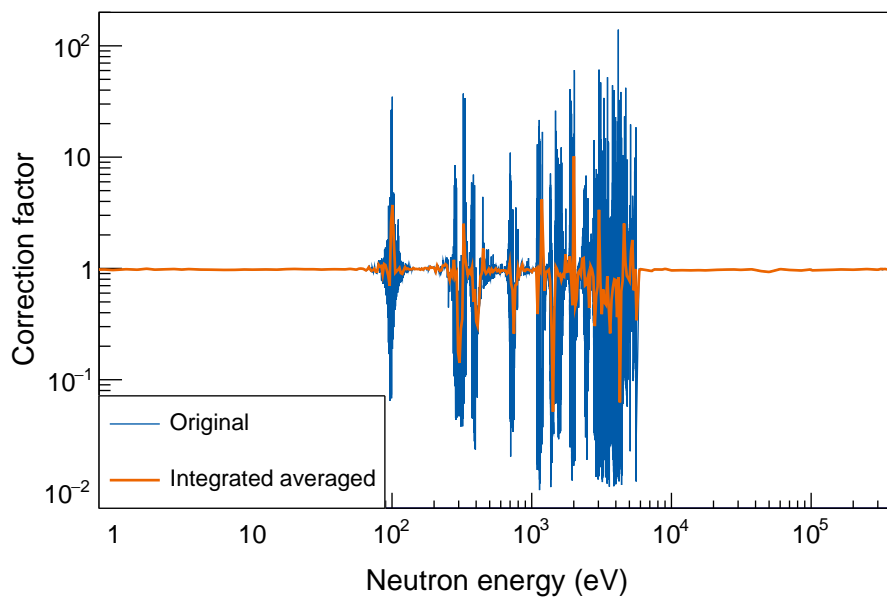
**Figure 5.17.:**  $^{69}\text{Ga}$ ,  $^{71}\text{Ga}$  and  $^{nat}\text{Pb}$  cross sections (from [43]) for neutron capture and elastic scattering. While the scattering cross sections are very similar, the ones for capture differ by several orders of magnitude across all energies.

the gallium isotopes, it is feasible to conclude that the majority of detected events were indeed caused by neutron capture events.

In order to approximate the quantitative contribution of the scattering events to the calculated cross sections, the gallium samples were simulated using the evaluated cross sections from ENDF/B-VIII.0 [43] for neutron capture and scattering. This resulted in neutron energy dependent correction factors to be applied to the measured data. These correction factors were interpolated, integrated over the range of each neutron energy bin of the experimental data, and normalized by the width of the bin (Figure 5.19). The operations of applying the correction factors and averaging the (corrected) counts are not commutative. However, the experimental data cannot feasibly be brought to the binning of the correction factors, which follows the ENDF adaptive binning; very fine within the resonances, and much broader in between. The effect of applying the largest correction factors in the resonances to finely binned experimental data with resulting higher statistical uncertainties would dominate any quantitative insights gained from the scattering correction itself. To verify the validity of this approach, it was performed for binnings of 100 and 1000 bins per decade in the original time of flight data. The differences between the two (Figure 6.4) were negligible,  $< 1\%$  for all  $k_B T$  of interest.



**Figure 5.18.:** Comparison of weighted  $^{69}\text{Ga}$  count spectra with scaled  $^{nat}\text{Pb}$  data. The  $^{nat}\text{Pb}$  data were scaled both to the total number of atoms and number of protons.

(a)  $^{69}\text{Ga}$  correction factors(b)  $^{71}\text{Ga}$  correction factors

**Figure 5.19.:** Correction factors for scattering effects, using simulations with ENDF cross sections. The orange line are the averaged correction factors adapted to the neutron energy binning of the experimental data.

## 5.6. Pulse height weighting technique

The next step in the analysis is the application of a detection efficiency correction to the count spectra. Since the incident photon energy is mostly deposited through Compton scattering, there is no immediate direct correlation between the energy of the incident photon and the energy deposited in the detector. Instead, the total energy detection technique (Section 2.3.3) requires determining a posteriori weighting factors of the  $C_6D_6$  detector responses [44].

The efficiency  $\varepsilon(E_\gamma)$  of a detector to detect a  $\gamma$ -ray of energy  $E_\gamma$  can be determined by

$$\varepsilon(E_\gamma) = \int_0^\infty R(E_d, E_\gamma) dE_d, \quad (5.11)$$

for the detector response  $R(E_d, E_\gamma)$ , which is defined as the fraction of all photons with energy  $E_\gamma$  which deposit energy  $E_d$  in the detector. In accordance with Eq.(2.32), the weighting function  $W(E_d)$ , which is to be applied to all deposited energies  $E_d$  such that

$$\int_0^\infty R(E_d, E_\gamma) W(E_d) dE_d = k E_\gamma, \quad (5.12)$$

i.e. the linear proportionality between incident  $\gamma$ -energy and detection efficiency holds after the application of the weighting function. The proportionality constant  $k$  is set to 1/MeV.

In order to be applied to the actual experimental data, the above expressions need to be adapted to discrete energies from the experimental spectra, such that

$$\begin{aligned} E_d &\rightarrow E_j \\ E_\gamma &\rightarrow E_i \\ R(E_d, E_\gamma) &\rightarrow R_{ij} \\ W(E_d) &\rightarrow W_j, \end{aligned} \quad (5.13)$$

and the integrals in the formulas above become finite sums. Combining the discrete form of Eq.(5.12) and Eq.(2.32) leads to the efficiency of detecting a  $\gamma$ -ray cascade,  $\varepsilon_c^w$

$$\varepsilon_c^w = \sum_i \sum_j W_j R_{ij} = \sum_i E_i = E_c = S_n + E_n. \quad (5.14)$$

This means that the weighting function can be applied to all counts at a certain time of flight (*tof*) and energy  $E_\gamma$ , leading to the total weighted number of counts at that time of flight

$$C^w(\text{tof}) = \sum_j W_j C(\text{tof}, E_j). \quad (5.15)$$

### 5.6.1. Monte Carlo detector simulation

Since the distribution of incident  $\gamma$ -energies in the experimental spectra is unknown, these cannot be used to determine the weighting function through Eq.(5.14). In the past, measurements with mono-energetic  $\gamma$ -ray sources were used to determine the needed detector responses. The lack of such sources across the whole energy range of interest and in sufficiently fine spacing caused high uncertainties in the calculated weighting function and thus, the yield.

Abbondanno *et al.* [41] showed that deriving the detector responses from Monte Carlo simulations of the experimental setup in the GEANT4 framework [45] reduced those uncertainties. The GEANT4 implementation of the Legnaro-type  $C_6D_6$  detectors and the capture setup in EAR1 [46, 47] was adapted to the exact geometry and distances between detectors and gallium sample position during this experimental campaign, visualized in Figure 5.20.

The simulated energies went from 100 keV to 1 MeV in steps of 100 keV, and then up to 12 MeV in steps of 1 MeV. The responses, normalized to the number of simulated photons for each energy, and broadened with the detector resolution (Figure 5.3), can be seen in Figure 5.21.



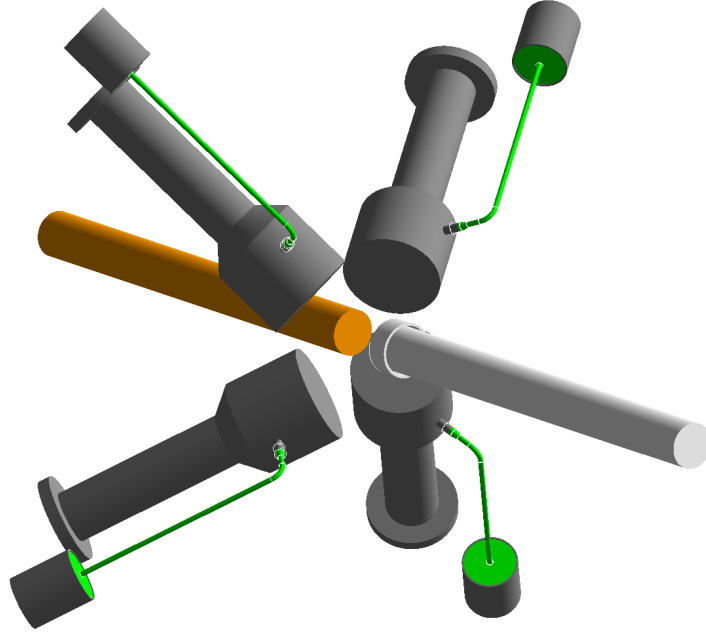


**Figure 5.20.:** Visualization of the GEANT4 [45] detector setup simulation. The  $C_6D_6$  detectors are mounted at a  $55^\circ$  backwards angle with regard to the neutron beam, which moves from the top left to bottom right.

### 5.6.2. Determination the weighting function

Using Eq.(5.14) and the simulated detector responses, the weighting function  $W_j$  can now be determined. It is implemented as a polynomial of degree  $k$ ,

$$W_j = \sum_k a_k E_j^k. \quad (5.16)$$

The parameters  $a_k$  are then determined by minimising the  $\chi^2$  of a least square fit for all simulated incident  $\gamma$ -energies  $E_i$  and their detector responses  $R_{ij}$

$$\chi^2 = \sum_i \left( E_i - \sum_{E_l}^{E_h} W_j R_{ij} \right)^2. \quad (5.17)$$

Here,  $E_h = 12$  MeV was chosen, which is much higher than the Q-values of the gallium isotopes, with the intent of reducing the effect of numerical instabilities at the upper edge of the fit.  $E_l$  was chosen to be set as the energy threshold that was applied to the experimental data as well, 100 keV. This means that the parts of the simulated detector responses  $< 100$  keV are not considered for the purposes of the minimization, which results in higher deviations from the desired linear proportionality, especially

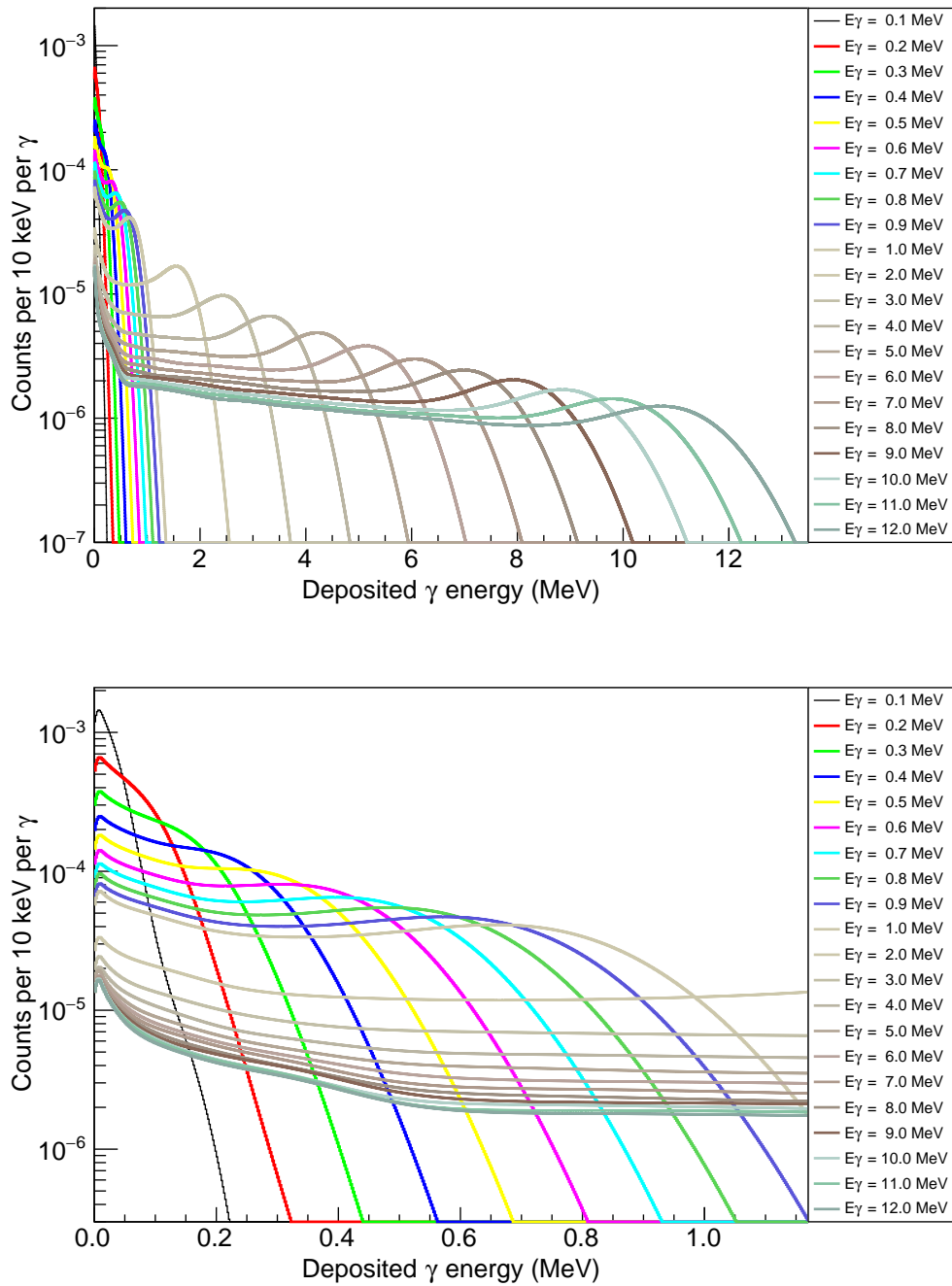


**Figure 5.21.:** Simulated  $C_6D_6$  responses for homogenous emission of monoenergetic  $\gamma$ -rays from the gallium sample, broadened with the detector resolution (Section 5.1, Figure 5.3).

closer to the threshold energy. The main advantage comes from not having to correct for the counts that are removed from the experimental data by applying the

threshold, which would require additional simulations of capture cascades of the relevant isotopes, and provides its own uncertainties.

The quality of the fit can be quantified by comparing the application of the weighting function to the detector response with the expected linear proportionality with the incident  $\gamma$ -energy of the simulation. For a perfect fit, their ratio  $Q$  should equal 1,

$$Q = \frac{\sum_j W_j R_{ij}}{E_i}. \quad (5.18)$$

The calculated weighting function and quality of the solution for detector 3 are displayed in Figure 5.22. The best fit was achieved for a polynomial weighting function of degree  $k = 3$ . The expected larger deviations close to the threshold energy can be seen, but are acceptably close to unity, resulting in a total uncertainty introduced by the pulse height weighting technique of 3.47% for  $^{69}\text{Ga}$  and 3.65% for  $^{71}\text{Ga}$  (Section 5.8.3).

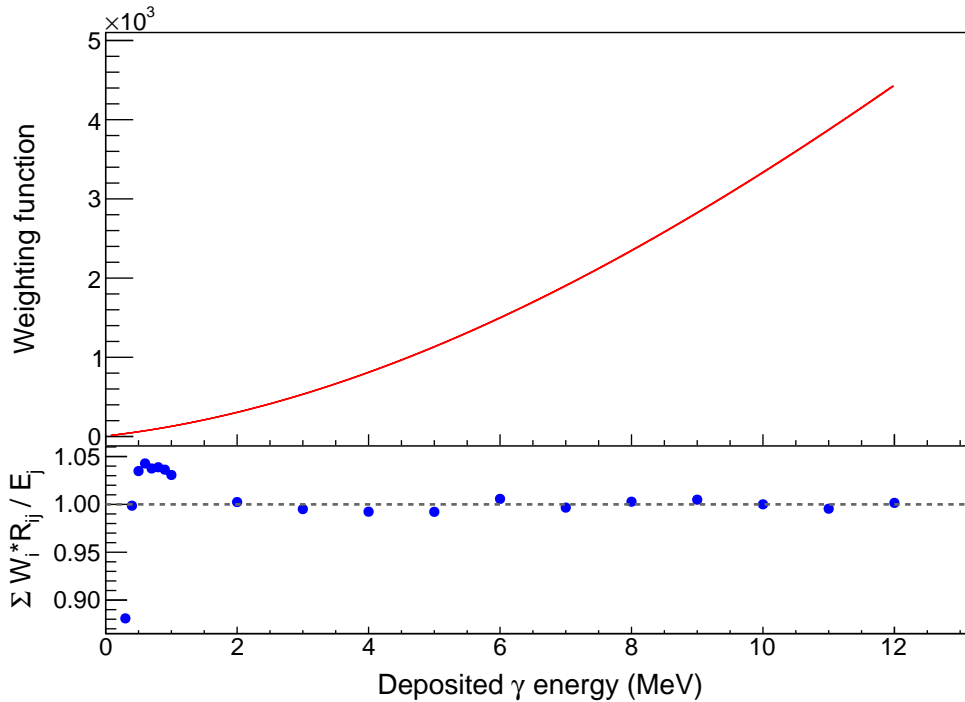


**Figure 5.22.:** Calculated weighting function (top panel) and quality check parameter  $Q$  (bottom panel) for detector 3. The ratio of detector responses with applied weighting function and the known number of simulated particles should ideally equal 1, indicated by the dashed line.

## 5.7. Determination of the neutron flux

In a time of flight experiment, the quantity measured is the number of reactions per incident projectile, the *reaction yield*  $Y_{n\gamma}$  in the case of neutron capture reactions,

$$Y_{n\gamma} = \frac{C - B}{\varepsilon\phi}, \quad (5.19)$$

with the initial detected number of counts  $C$ , background counts  $B$ , detection efficiency  $\varepsilon$  and neutron flux  $\phi$  [48]. The quantity of interest, the cross section for the neutron capture in the sample,  $\sigma_{n\gamma}$ , is related to the reaction yield by

$$\sigma_{n\gamma} = \frac{Y_{n\gamma}}{n}, \quad (5.20)$$

with the areal number density  $n$ .

The background subtraction (Section 5.5) and efficiency correction (Section 5.6) in Eq.(5.19) have already been performed in the previous sections, so the one remaining step is to determine the neutron flux each sample was exposed to.

### 5.7.1. Evaluated n\_TOF flux

The neutron flux in n\_TOF EAR1 follows an energy dependence proportional to  $1/E_n$ . It was evaluated in a dedicated measurement campaign, combining the data of several detection systems [36], resulting in a flux profile in isoethargic units,  $d\Phi/d\ln(E)/\text{pulse}$  (Figure 5.23), with the nominal pulse of  $7 \cdot 10^{12}$  protons at n\_TOF. Its uncertainties for different neutron energy ranges are listed in Table 5.3.

Neutron energy range	Uncertainty
0.025 eV - 100 eV	1%
100 eV - 10 keV	2%
10 keV - 100 keV	4 - 5%
100 keV - 10 MeV	~2%

**Table 5.3.:** Uncertainties of the n\_TOF phase II evaluated flux, extracted from [36].

While the measurement in this work was performed during n\_TOF phase III, no evaluated flux exists for this time period. Simulations and measurements confirmed,

however, that the differences to the phase II flux are negligible, with the recommendation of using the evaluated phase II flux [49].

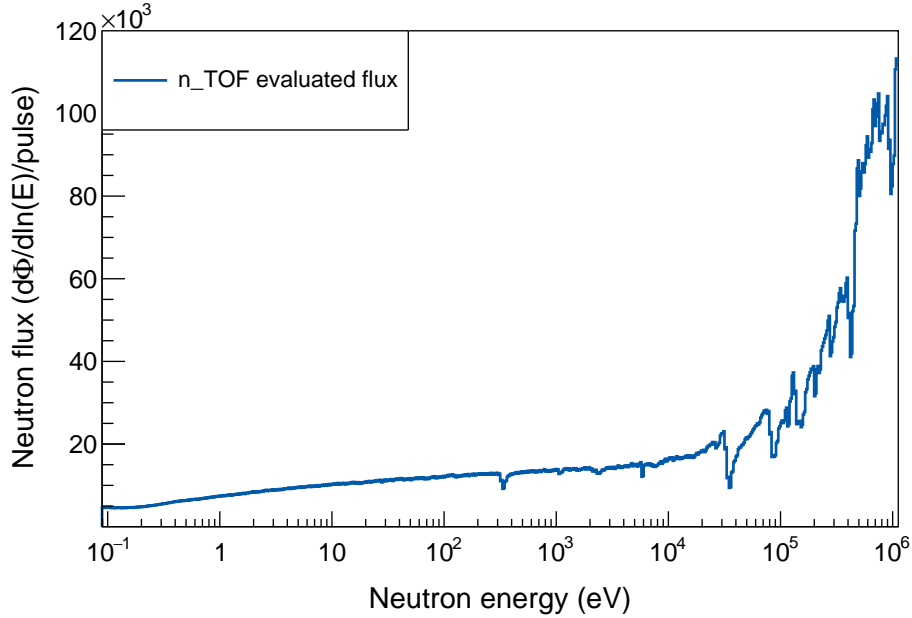


**Figure 5.23.:** The evaluated n\_TOF EAR1 phase II neutron flux in isolethargic units,  $d\Phi/d\ln(E)/\text{pulse}$ , in 100 bpd binning.

The background-subtracted and efficiency-corrected count spectra are then normalized in each neutron energy bin with the corresponding neutron flux value, scaled with the number of proton pulses on the respective sample. Due to the differences in bin widths between count spectra and evaluated flux, the latter are adapted to the bin width of the former, with a local  $1/E_n$  approximation to correct for the comparatively large bin widths of the evaluated flux at high neutron energies.

### 5.7.2. Saturated resonance technique

While all components of Eq.(5.19) are now included, there is a caveat with regard to the normalization to the neutron flux. The evaluated flux was determined as a total number of neutrons arriving in the experimental area. However, specifics in the sample geometry and positioning cause only a certain fraction of the total neutron flux to actually interact with the sample, and therefore be considered for the yield calculation. This correction factor, also known as *beam interception factor*, is determined using the saturated resonance method [50].

In this method, the  $^{197}\text{Au}$  resonance at 4.9 eV is saturated, meaning that all neutrons passing the sample interacted with it. This can be seen by the characteristic plateau shape of the resonance at this energy in the data (Figure 5.24).

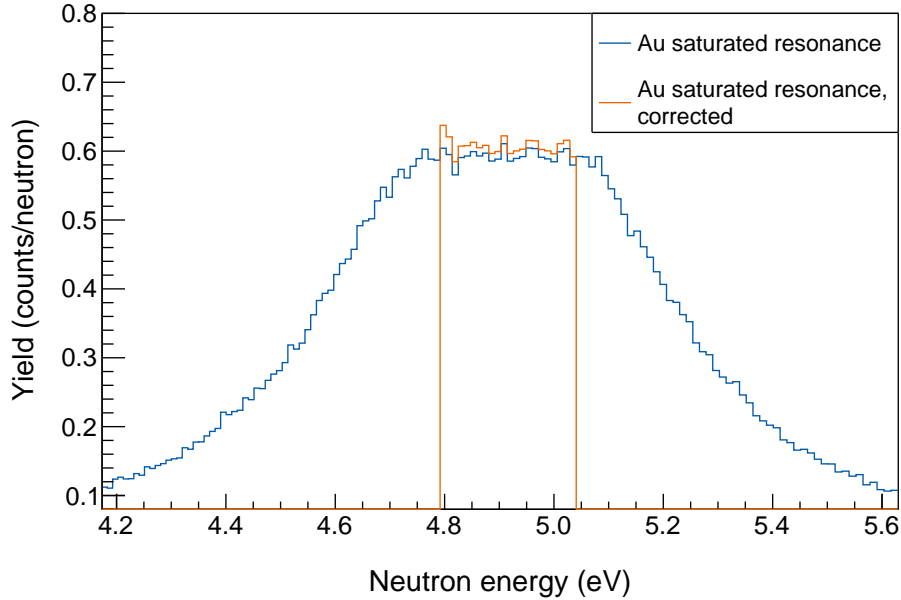


**Figure 5.24.:** The plateau of the saturated 4.9 eV  $^{197}\text{Au}$  resonance in the experimental data (blue). Included is also the correction for scattered neutrons from simulations (orange).

The total number of neutrons of this specific energy range impinging on the gold target needs to be corrected, however, for the fraction of neutrons that interact through scattering effects instead of capture. Using both well known cross sections [43], the exact sample geometry was simulated in GEANT4 [45] to determine this correction factor. Since the neutron capture reaction is dominant in this energy region - which is why we are using the saturated resonance method exactly there -, the correction only amounts to about 2%.

The beam interception factors are then calculated from the assumption that the yield, the number of reactions per incident article, should equal 1 in the plateau of the saturated resonance. Table 5.4 shows the final calculated beam interception factors, by which the entire yield is scaled across all neutron energies.

	Detector 1	Detector 2	Detector 3	Detector 4
Correction factor	0.6066	0.5263	0.6968	0.5684

**Table 5.4.:** Beam interception factors for all four  $\text{C}_6\text{D}_6$  detectors, calculated from the saturated resonance technique.

## 5.8. Uncertainties

The uncertainties in this analysis were treated according to the standard methods regarding the propagation of uncorrelated (Eq.(A.1)) and correlated (Eq.(A.2)) uncertainties, further elaborated in Section A.1.

The end results determined in this work are yields, differential and integrated neutron capture cross sections. Some of their contributing uncertainties, like those of the sample geometry and mass, as well as the application of the pulse height weighting, are independent of the neutron energy. Others, like the ToF to energy conversion, background subtraction and neutron flux normalization, vary for different neutron energies, and need to be calculated accordingly.

### 5.8.1. ToF to energy conversion

The two parameters which are needed to calculate the neutron energy from the measured time of flight are the flight path length  $L$ , and the time offset  $t_t$ , see Section 5.3. They are determined from a fit to well known Au resonances. While both have individual uncertainties from the fit, the relevant value is the total uncertainty when determining neutron energy using Eq.(2.26) and Eq.(5.6). Both parameters are correlated, so the covariance matrix of the fit is used as input for Eq.(A.2). The total uncertainty is displayed as error bars in Figure 5.9 for several example energies, and is found to be  $< 1\%$  even for neutron energies around 1 MeV, which extends beyond the neutron energy region of interest. Therefore, a fit was applied to the energy dependent neutron energy uncertainty values, and included in the total uncertainty calculation of the MACS.

### 5.8.2. Background subtraction

The uncertainty due to background subtractions (Section 5.5) is statistical in its origin. The ambient and empty sample data that were used for background subtractions had lower count statistics than the gallium data. The statistical errors for each bin were added up correctly (Eq.(A.1)) and carried through the complete analysis. This provides the final yields and cross sections with statistical uncertainties for each neutron energy bin and the calculated MACS with a total statistical uncertainty, which is provided in Section 6.2.

### 5.8.3. Pulse height weighting

The uncertainty caused by applying the weighting function to the counts of each deposited energy is of a systematic nature. It is therefore feasible to apply the interpolated offset of the weighting function to the weighted counts for each energy, and compare the total number of counts across the whole energy range. Since there is no direct correlation between incident neutron energy and the energy the produced photon deposits in the detector, it can be assumed that the difference in weighted counts, and the resulting uncertainty, is the same regardless of neutron energy.

The quality ratio between applied weighting function and simulated data,  $Q$  in Eq.(5.18), was interpolated across the whole energy range of experimental data, 0.1 MeV - 10 MeV. The determined weighting functions were applied to each detector individually, once directly, and once scaled by  $Q$ , to reproduce the effect of the imperfect weighting function. The resulting weighted amplitude count spectra of all added detectors are shown in Figure 5.25 and Figure 5.26. The resulting systematic uncertainties from comparing the total counts are 3.47% for  $^{69}\text{Ga}$  and 3.65% for  $^{71}\text{Ga}$ .

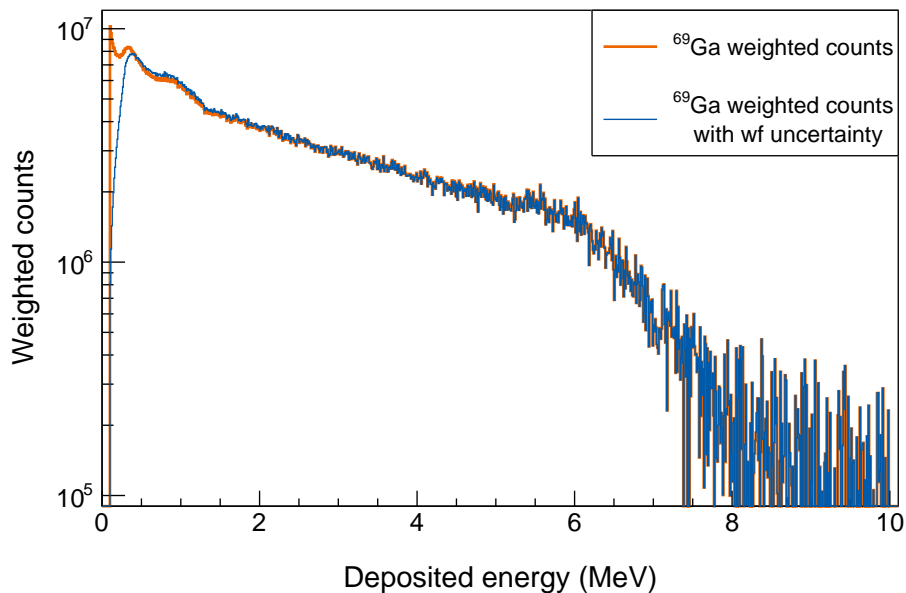


**Figure 5.25.:** Weighted counts of  $^{69}\text{Ga}$  runs plotted over the deposited energy. The orange line is with the respective weighting function applied, while the blue line shows the change in weighted counts when applying the uncertainty of the determined weighting function.



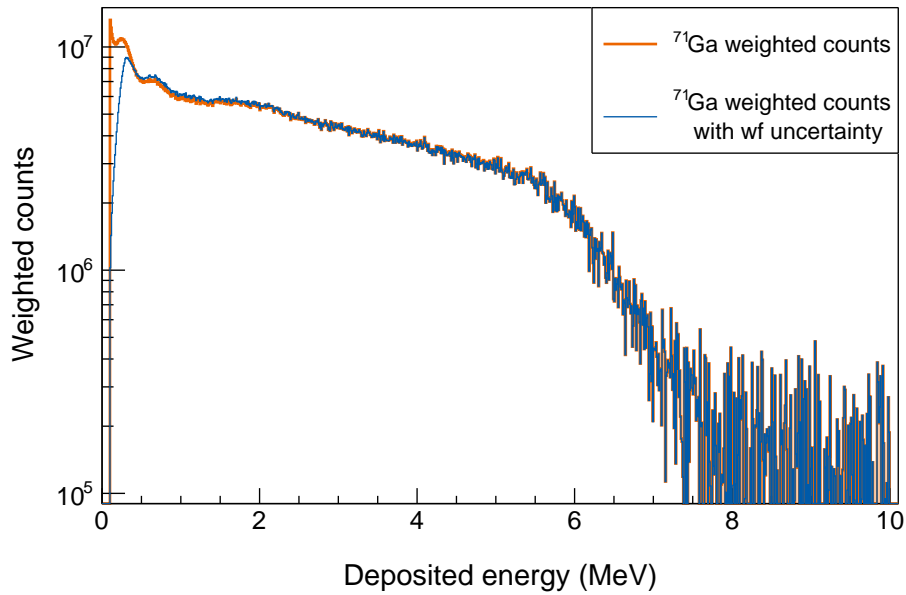


**Figure 5.26.:** Weighted counts of  $^{71}\text{Ga}$  runs plotted over the deposited energy. The orange line is with the respective weighting function applied, while the blue line shows the change in weighted counts when applying the uncertainty of the determined weighting function.

#### 5.8.4. Neutron flux normalization

The count spectra were normalized using the evaluated n\_TOF flux, Section 5.7.1. The uncertainties in Table 5.3 from [36] are treated as systematic. While their value for a specific neutron energy is provided, the calculation of MACS values across the different neutron energy ranges requires an additional step. It was decided to individually calculate an average uncertainty value for each  $k_{\text{B}}T$ , using the same Maxwell-Boltzmann factors (Eq.(2.18)) as weights that are applied to the cross section data in the integration process for that specific  $k_{\text{B}}T$ .

#### 5.8.5. Sample mass and geometry

The uncertainties of the sample mass and geometry (in this case, diameter) directly translate to uncertainties in the total number of target nuclei, and the areal number density, see Eq.(5.20). The mass uncertainties are listed in Table 3.2, while the uncertainty of the sample diameter was 0.5%, determined from measurements of both the sample diameter and sample production frame (Figure 3.1). This leads to a total uncertainty of the areal density of 1.0%.

### 5.8.6. Sample contamination correction

The two gallium samples, despite their high level of enrichment, still contain low amounts of the respective other stable gallium isotope, see Table 3.1. This means that the experimental data, and thus, calculated yields and cross sections, contain contributions of the other isotope as well. This is illustrated in Figure 5.27, with a resonance from  $^{71}\text{Ga}$  being visible on top of the  $^{69}\text{Ga}$  data.

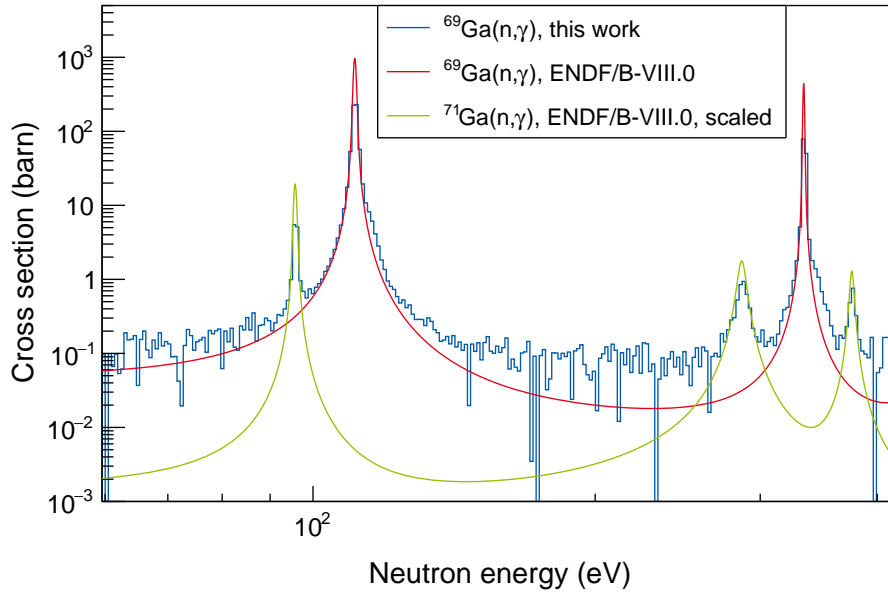


**Figure 5.27.:** The  $^{69}\text{Ga}$  cross section from the measured data. Overlaid are the ENDF cross section data for both  $^{69}\text{Ga}$  and  $^{71}\text{Ga}$  (scaled for visual purpose), showing the  $^{71}\text{Ga}$  resonance at 96 eV in the  $^{69}\text{Ga}$  data.

With the definition of the reaction yield, Eq.(5.19), in mind, the experimental yields calculated from the measurement data,  $Y_{69}^{\text{exp}}$  and  $Y_{71}^{\text{exp}}$  can be written as a combination of the two pure gallium components,  $Y_{69}$  and  $Y_{71}$ :

$$\begin{aligned}
 Y_{69}^{\text{exp}} &= Y_{69} \cdot n_{69\text{in}69} + Y_{71} \cdot n_{71\text{in}69} \cdot \frac{\varepsilon_{71}}{\varepsilon_{69}}, \\
 Y_{71}^{\text{exp}} &= Y_{69} \cdot n_{69\text{in}71} \cdot \frac{\varepsilon_{69}}{\varepsilon_{71}} + Y_{71} \cdot n_{71\text{in}71},
 \end{aligned}
 \tag{5.21}$$

with mass fraction  $n_{i\text{in}j}$  of isotope  $i$  in sample  $j$ . The correction factors  $\varepsilon_{71}/\varepsilon_{69}$  and  $\varepsilon_{69}/\varepsilon_{71}$  are included to compensate for the pulse height weighting technique applying the incorrect efficiency correction to the respective total experimental yields.

The two pure yields  $Y_{69}$  and  $Y_{71}$  can then be extracted from the two equations in Eq.(5.21). The comparison of yields after applying the impurity correction is shown in Figure 5.28. While a reduction of the  $^{71}\text{Ga}$  resonances can be observed, it is not sufficient to completely remove the resonances sitting on top of the  $^{69}\text{Ga}$  data. While it might be possible to find a set of impurity mass fractions that better achieve this removal, this phenomenological approach seems ill advised in the context of too many uncertainties on the experimental data. Furthermore, the reduced yield after the subtraction of the impurity component is compensated by the smaller number of target nuclei in the sample when calculating the cross section, resulting in only small differences in the calculated MACS values. Therefore, the MACS values will be calculated for the case of no impurities, as well as the impurity mass fractions provided by the analysis sheet, Table 3.1. Should a future material analysis provide a different composition of the samples, this can easily be applied to the reaction yields, using the method described above.

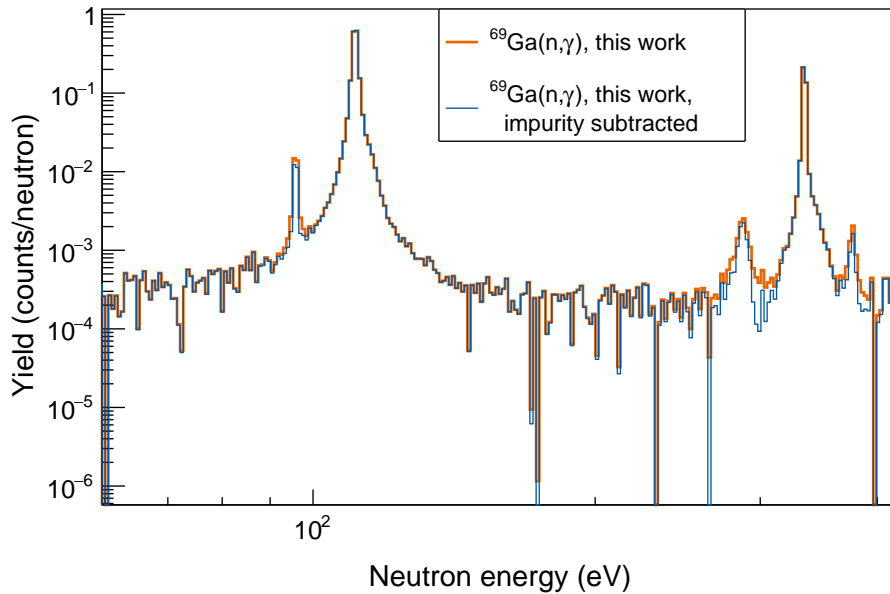


**Figure 5.28.:** The  $^{69}\text{Ga}$  yield before (orange) and after subtracting the  $^{71}\text{Ga}$  contribution (blue). While the heights of the  $^{71}\text{Ga}$  resonances are reduced, they still clearly remain visible in the data. This indicates that the mass fractions of the impurities in the samples are not correct.



## 6.1. Cross section from yields

The differential neutron capture cross sections were determined from the yields using Eq.(5.20) in Figure 6.1 and Figure 6.2, and compared with the evaluated values from ENDF/B-VIII.0 [43]. In the resolved resonance region, the data show good agreement for the resonances, but seem to overestimate the cross sections between resonances. This is indicative of background components that could not accurately be quantified, like the sample impurities (Section 5.8.6) and scattering components (Section 5.5.3). It is likely that if these effects cause observable systematic offsets in the resolved resonance region, they will also occur in the unresolved resonance region.

## 6.2. MACS calculation

The Maxwellian Averaged Cross Sections were calculated from the differential cross sections, using Eq.(2.18), for different  $k_B T$  values of astrophysical interest in Table 6.1 and Table 6.2. The uncertainties were derived from the various methods described in Section 5.8.

The MACS values for the data corrected for the contamination in the sample, as discussed in Section 5.8.6, were calculated in the same manner. They are compared to the data without this correction in Figure 6.3. The small deviations between the

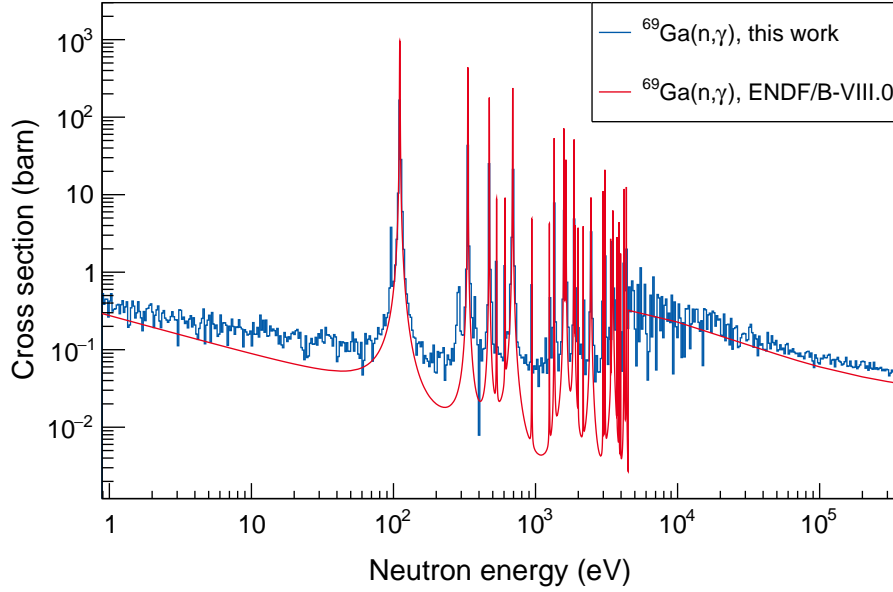


**Figure 6.1.:** The differential  $^{69}\text{Ga}$  neutron capture cross section calculated from the experimental yield.

$k_{\text{B}}T$ (keV)	$\langle\sigma_{69\text{Ga}}\rangle$ (mb)
5 keV	$438.721 \pm 1.486_{\text{stat}} \pm 20.600_{\text{syst}}$
8 keV	$337.477 \pm 1.288_{\text{stat}} \pm 17.208_{\text{syst}}$
10 keV	$297.428 \pm 1.211_{\text{stat}} \pm 15.654_{\text{syst}}$
15 keV	$235.272 \pm 1.088_{\text{stat}} \pm 12.868_{\text{syst}}$
20 keV	$198.749 \pm 0.994_{\text{stat}} \pm 10.956_{\text{syst}}$
25 keV	$174.502 \pm 0.914_{\text{stat}} \pm 9.543_{\text{syst}}$
30 keV	$157.202 \pm 0.847_{\text{stat}} \pm 8.459_{\text{syst}}$
40 keV	$134.125 \pm 0.745_{\text{stat}} \pm 6.935_{\text{syst}}$
50 keV	$119.361 \pm 0.669_{\text{stat}} \pm 5.942_{\text{syst}}$
60 keV	$109.002 \pm 0.609_{\text{stat}} \pm 5.256_{\text{syst}}$
80 keV	$95.156 \pm 0.520_{\text{stat}} \pm 4.382_{\text{syst}}$
90 keV	$90.209 \pm 0.486_{\text{stat}} \pm 4.088_{\text{syst}}$
100 keV	$86.085 \pm 0.459_{\text{stat}} \pm 3.851_{\text{syst}}$

**Table 6.1.:** Calculated MACS values of  $^{69}\text{Ga}(n,\gamma)$ , including systematic and statistical uncertainties, at astrophysically relevant energies.

values are dominated by the larger respective uncertainty ranges. Therefore, only the uncorrected data were used in the following comparisons with other data.

The correction for scattering effects using simulations with the evaluated ENDF/B-VIII.0 [43] cross sections was discussed in Section 5.5.3. Figure 6.4 shows the

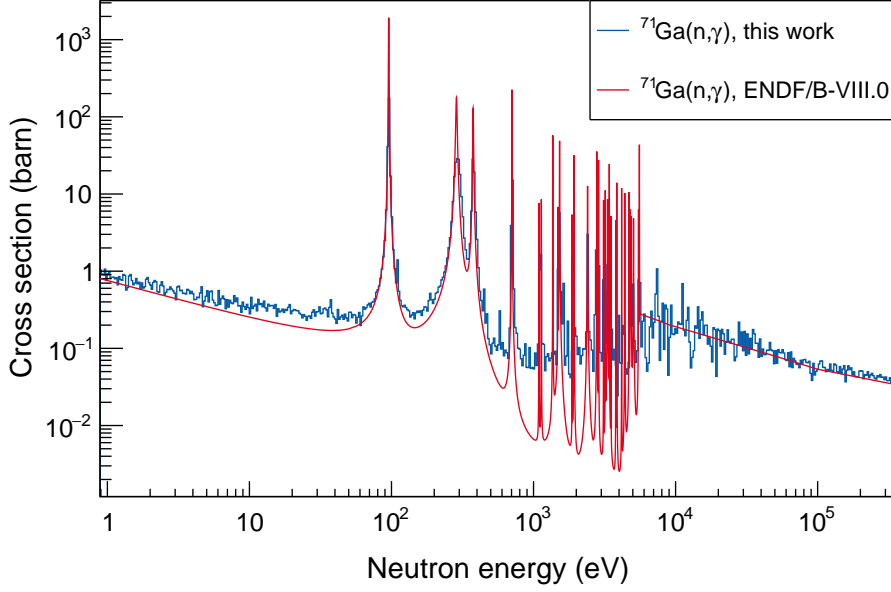


**Figure 6.2.:** The differential  $^{71}\text{Ga}$  neutron capture cross section calculated from the experimental yield.

$k_{\text{B}}T$ (keV)	$\langle\sigma_{71\text{Ga}}\rangle$ (mb)
5 keV	$325.611 \pm 1.627_{\text{stat}} \pm 15.727_{\text{syst}}$
8 keV	$249.283 \pm 1.416_{\text{stat}} \pm 13.021_{\text{syst}}$
10 keV	$220.027 \pm 1.333_{\text{stat}} \pm 11.845_{\text{syst}}$
15 keV	$175.318 \pm 1.205_{\text{stat}} \pm 9.792_{\text{syst}}$
20 keV	$148.924 \pm 1.105_{\text{stat}} \pm 8.381_{\text{syst}}$
25 keV	$131.135 \pm 1.018_{\text{stat}} \pm 7.323_{\text{syst}}$
30 keV	$118.273 \pm 0.944_{\text{stat}} \pm 6.504_{\text{syst}}$
40 keV	$100.911 \pm 0.829_{\text{stat}} \pm 5.341_{\text{syst}}$
50 keV	$89.740 \pm 0.743_{\text{stat}} \pm 4.581_{\text{syst}}$
60 keV	$81.958 \pm 0.675_{\text{stat}} \pm 4.060_{\text{syst}}$
80 keV	$71.882 \pm 0.573_{\text{stat}} \pm 3.409_{\text{syst}}$
90 keV	$68.472 \pm 0.535_{\text{stat}} \pm 3.198_{\text{syst}}$
100 keV	$65.749 \pm 0.503_{\text{stat}} \pm 3.034_{\text{syst}}$

**Table 6.2.:** Calculated MACS values of  $^{71}\text{Ga}(n, \gamma)$ , including systematic and statistical uncertainties, at astrophysically relevant energies.

effects of these corrections on the calculated MACS values. Different binnings of the experimental data, and subsequent averaging of the correction factors to these binnings, show almost no effect. However, the correction for scattering events does cause a systematic decrease of the calculated MACS values,

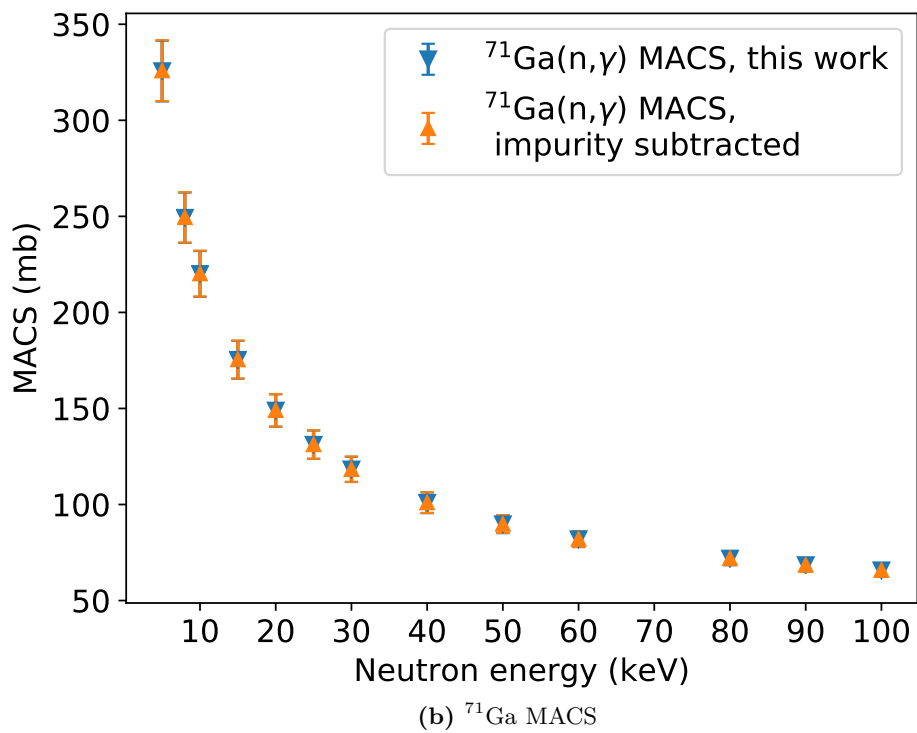
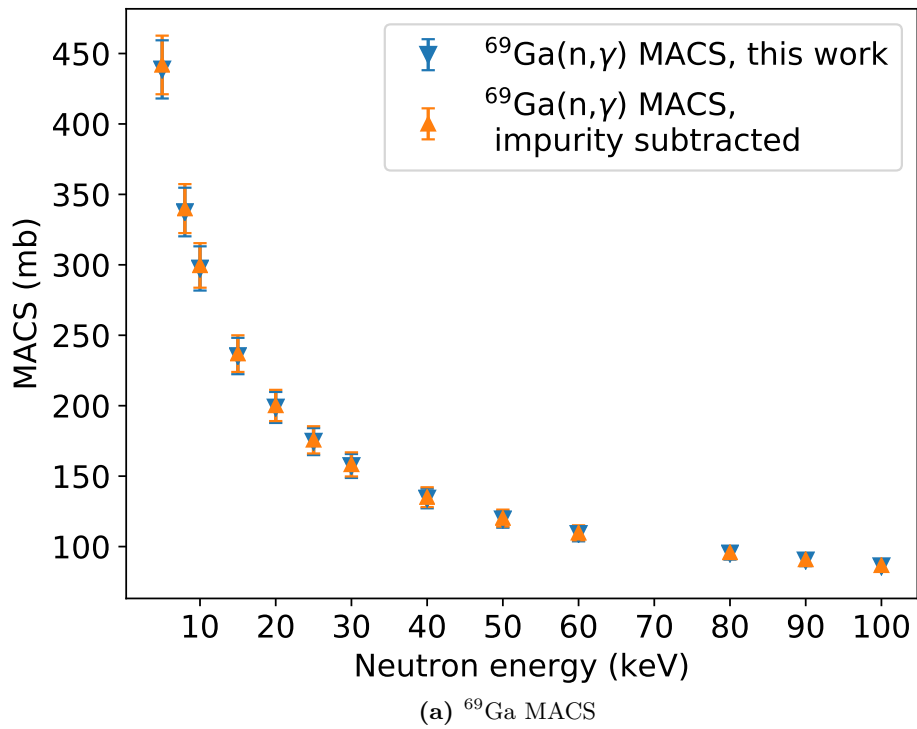


**Figure 6.3.:** The  $^{69}\text{Ga}(n,\gamma)$  and  $^{71}\text{Ga}(n,\gamma)$  MACS values calculated from this work, both for the assumption of a pure sample, and 0.52%  $^{71}\text{Ga}$  impurity. The deviations between the two are overshadowed by the uncertainty bands.



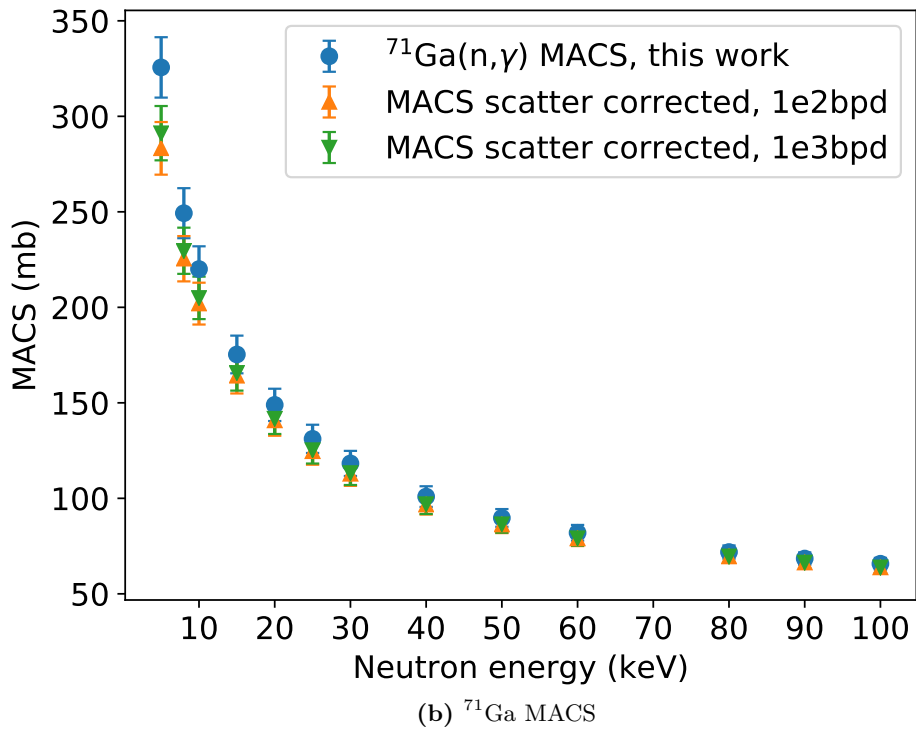
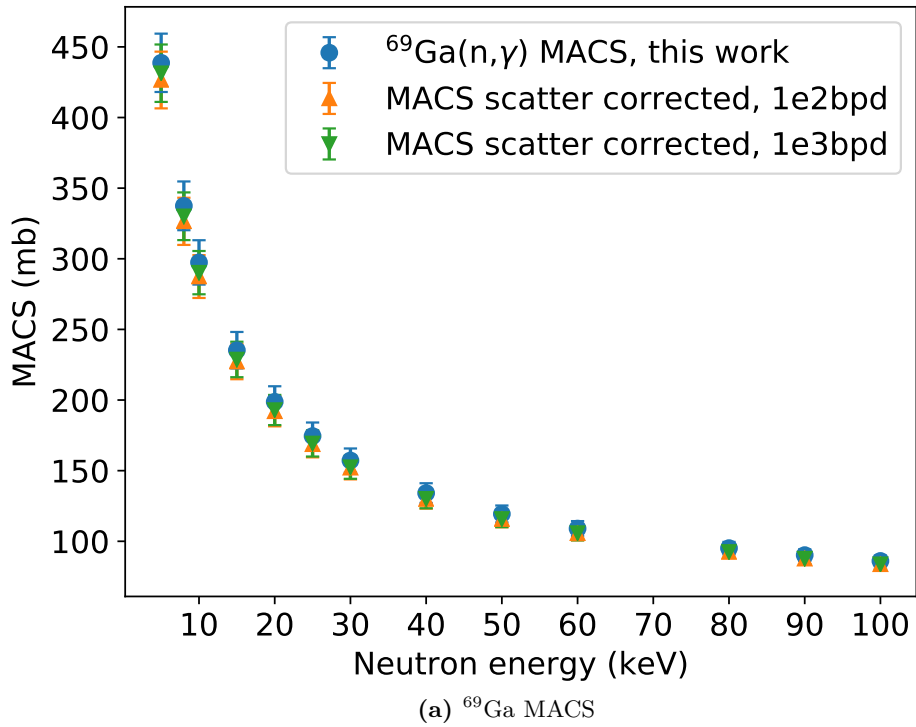


**Figure 6.4.:** The  $^{69}\text{Ga}(n,\gamma)$  and  $^{71}\text{Ga}(n,\gamma)$  MACS values calculated from this work, using the scattering correction factors calculated from the evaluated cross sections. While the application of the scattering shows a systematic reduction, the deviations caused by averaging the correction factors for different neutron energy binnings are negligible.

when compared with the uncorrected values. This effect is to be expected when considering the qualitative approximation of the scattering background in the gallium data through the  $^{nat}\text{Pb}$  data in Figure 5.18.

## 6.3. Comparison of results

### 6.3.1. Previous experimental data situation

Cross section data from several activation measurements exist for both  $^{69}\text{Ga}$  and  $^{71}\text{Ga}$ . Using a nearly mono energetic Sb-Be neutron source with peaks at 23 keV (97%) and 378 keV (3%), two different measurements of  $^{69}\text{Ga}$  determined neutron capture cross sections of  $(148.4 \pm 1.2)$  mb [51, 52] and  $(50 \pm 5)$  mb [53, 52], respectively, showing a disagreement of a factor of three. The same type of Sb-Be neutron source was also used for two activation measurements of  $^{71}\text{Ga}$ . Here, the obtained cross sections were  $(140 \pm 30)$  mb [54, 52] and  $(75 \pm 10)$  mb [53, 52].

Another activation measurement, using a mono energetic neutron beam with  $E_n = 25$  keV, determined the  $^{71}\text{Ga}$  cross section as  $(104 \pm 14)$  mb [55, 52], while an integral measurement with a quasi stellar neutron energy distribution at  $k_{\text{B}}T = 25$  keV by Walter *et al.* obtained the currently recommended  $^{71}\text{Ga}$  cross section of  $(137 \pm 8)$  mb [56, 14].

Dovbenko *et al.* [57, 52] performed a series of activation measurements at several neutron energies. The determined cross sections at 27 keV were  $(172 \pm 49)$  mb for  $^{69}\text{Ga}$  and  $(159 \pm 45)$  mb for  $^{71}\text{Ga}$ , while at 100 keV, they were  $(61 \pm 18)$  mb and  $(61 \pm 22)$  mb, respectively.

The only previous time of flight measurement on gallium was performed on a natural sample, containing both isotopes [58]. Measurements on other samples in the same experimental campaign exhibit strong deviations from more recent results [14].

### 6.3.2. Current data

The MACS data calculated from this work were compared with the evaluated data from the KADoNiS v0.3 database [14] which aggregates and evaluates the previous experimental and theoretical data. Their comparison is displayed in Figure 6.5 and Figure 6.6.

The  $^{69}\text{Ga}(n, \gamma)$  MACS from this work are systematically higher than the values from the database, well beyond the range of the uncertainties. Meanwhile, the  $^{71}\text{Ga}(n, \gamma)$  MACS values show good agreement for energies above 20 keV.

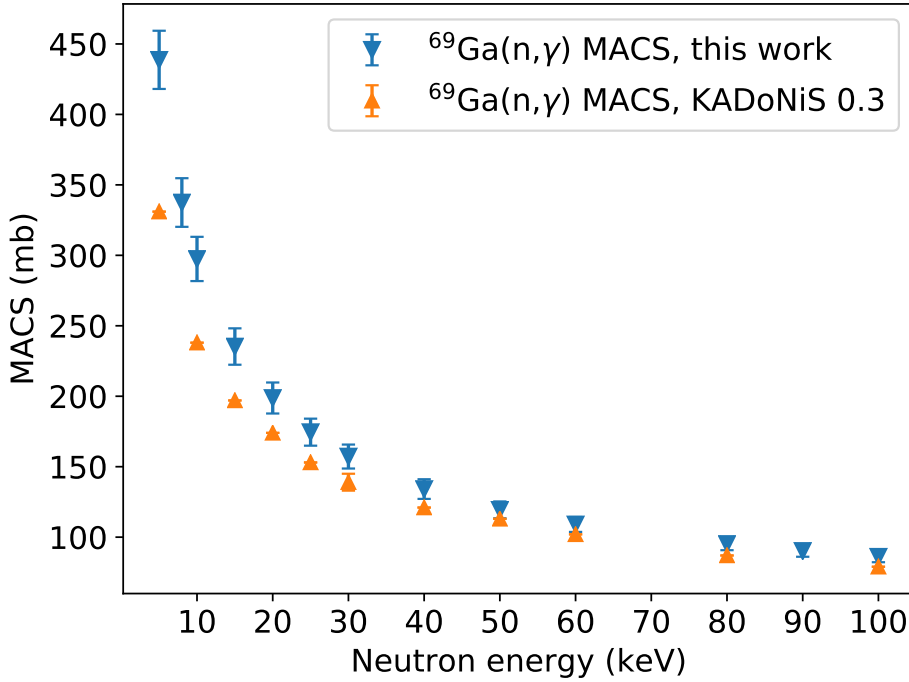


**Figure 6.5.:** The  $^{69}\text{Ga}(n, \gamma)$  MACS values from this work, compared with the evaluation from KADoNiS v0.3 [14].

More recently, activation measurements were performed by Göbel *et al.* [59] and Brückner [60], the latter also including the enriched samples used in this work. Both used the  $^7\text{Li}(p, n)$  reaction at a proton energy of 1912 keV to produce their neutrons, which generates a neutron spectrum that is very similar to the  $k_{\text{B}}T = 25$  keV Maxwell-Boltzmann distribution. Göbel *et al.* [59] calculated their results as *Spectrum Averaged Cross Section* (SACS), and showed that the ratio of gallium to the well-known  $^{197}\text{Au}$  SACS can be directly compared to the corresponding ratio of MACS values from the KADoNiS database for  $k_{\text{B}}T = 25$  keV. Brückner [60] chose a similar approach in calculating the SACS ratios.

To enable comparison with these results, the calculated MACS values and uncertainties at  $k_{\text{B}}T = 25$  keV from this work were divided by the corresponding MACS value from the KADoNiS v0.3 database,  $\sigma_{^{197}\text{Au}, \text{MACS}} = 648$  mb.

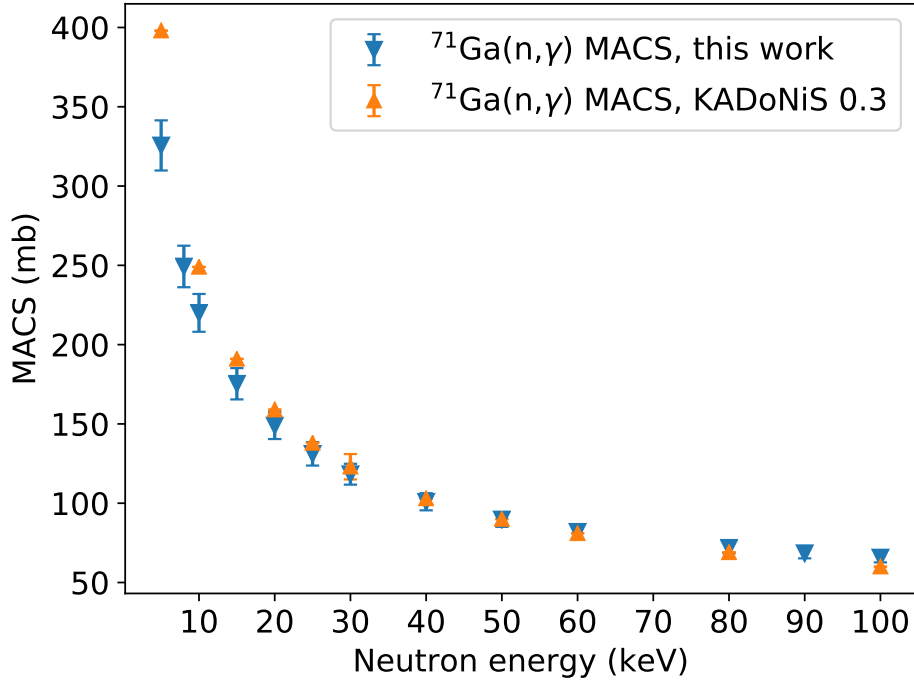


**Figure 6.6.:** The  ${}^{71}\text{Ga}(n,\gamma)$  MACS values from this work, compared with the evaluation from KADoNiS v0.3 [14].

	$\langle\sigma_{69\text{Ga}}\rangle/\langle\sigma_{197\text{Au}}\rangle$ (mb)	$\langle\sigma_{71\text{Ga}}\rangle/\langle\sigma_{197\text{Au}}\rangle$ (mb)
This work	$0.2693 \pm 0.0148$	$0.2024 \pm 0.0113$
Göbel <i>et al.</i>	$0.2862 \pm 0.0192$	$0.1727 \pm 0.0107$
Brückner	$0.2624 \pm 0.0172$	$0.1179 \pm 0.0074$
KADoNiS (from Göbel)	$0.24 \pm 0.01$	$0.21 \pm 0.01$

**Table 6.3.:** Comparison of MACS values for  $k_{\text{B}}T = 25$  keV from this work, normalized to  ${}^{197}\text{Au}$ , with equivalent ratios from [59] and [60].

The results in Table 6.3 show better agreement with the results of Göbel *et al.* and Brückner for  ${}^{69}\text{Ga}$ , but are closer to the KADoNiS values for  ${}^{71}\text{Ga}$ , from which the other two works show larger deviations.

Stellar models of the weak and main s-process component require accurate neutron capture cross sections as inputs. The  $^{69}\text{Ga}(n, \gamma)$  and  $^{71}\text{Ga}(n, \gamma)$  reactions are of importance for the weak s process, with uncertainties and disagreements in the available data so far. Time of flight measurements using enriched samples were performed at the n\_TOF neutron time of flight facility at CERN, in order to determine differential neutron capture cross sections. These cross sections make it possible to compare with with the available MACS data at  $k_{\text{B}}T = 25$  keV, and to calculate the MACS at  $k_{\text{B}}T = 90$  keV, which is relevant for the weak s process in massive stars.

Gallium's low melting point and physical properties, especially its destructive interaction with aluminium, required the development of a new sample production process to ensure no mass losses of the highly enriched gallium samples occurred.

The measurement campaign described in this thesis was performed at the n\_TOF EAR1 facility at CERN. The emitted photons from neutron capture events on the sample were registered using four Legnaro type  $\text{C}_6\text{D}_6$  detectors.

Data analysis included consistency checks on the detectors over time, time of flight to neutron energy calibration, assesment and subtraction of different background components, efficiency correction via the pulse height weighting technique, and neutron flux normalization using the saturated resonance method.

While the subtraction of ambient and beam related background components worked as intended, the background due to scattered neutrons could only be approximated from  $^{nat}\text{Pb}$  data and the evaluated cross sections. A direct measurement of the

scattering or total cross sections would help to further reduce these uncertainties, which become apparent especially between the resonances.

The accuracy of the pulse height weighting technique can be improved by dedicated GEANT4 [45] simulations of the  $^{69}\text{Ga}$  and  $^{71}\text{Ga}$  capture cascades. These cascades need to be generated from known nuclear level properties, using a code like DICEBOX [61], and correct for the effect of the experimental detection threshold, and transitions without emitted  $\gamma$ -rays (electron conversion).

A dedicated resonance analysis using R-matrix codes like SAMMY [62] would improve the accuracy of the saturated resonance method, and the differential cross section in the resolved resonance region. For the purposes of MACS at astrophysical energies, however, these variations should have little impact.

The resulting differential neutron capture cross sections were used to determine the Maxwellian averaged cross section values for a range of astrophysically relevant energies. They show total uncertainties  $< 5\%$ .

At  $k_{\text{B}}T = 25 \text{ keV}$  and  $k_{\text{B}}T = 90 \text{ keV}$ , the two temperatures relevant for the weak s process, the determined cross sections were

$$\sigma_{\text{MACS},^{69}\text{Ga}}(25 \text{ keV}) = (174.502 \pm 0.914_{\text{stat}} \pm 9.543_{\text{syst}}) \text{ mb} ,$$

$$\sigma_{\text{MACS},^{69}\text{Ga}}(90 \text{ keV}) = (90.209 \pm 0.486_{\text{stat}} \pm 4.088_{\text{syst}}) \text{ mb} ,$$

$$\sigma_{\text{MACS},^{71}\text{Ga}}(25 \text{ keV}) = (131.135 \pm 1.018_{\text{stat}} \pm 7.323_{\text{syst}}) \text{ mb} ,$$

$$\sigma_{\text{MACS},^{71}\text{Ga}}(90 \text{ keV}) = (68.472 \pm 0.535_{\text{stat}} \pm 3.198_{\text{syst}}) \text{ mb} .$$

Another time of flight measurement using the two enriched gallium samples from this work, as well as a natural gallium sample, was conducted at the Lujan Neutron Scattering Center of the Los Alamos Nuclear Science Center (LANSCE). Its analysis could lend further credence to one of the disagreeing previous results, and provide an explanation for the discrepancy in measured cross sections between enriched and natural samples described in [59, 60, 63]. Furthermore, stellar nucleosynthesis network calculations could be performed with the results of this work, to determine their effect on the stellar abundances in the weak s process.

Im Rahmen dieser Arbeit wurden die differentiellen Neutroneneinfangwirkungsquerschnitte von  $^{69}\text{Ga}$  und  $^{71}\text{Ga}$  vermessen. Die beiden stabilen Gallium Isotope werden in der schwachen Komponente des astrophysikalischen s-Prozess in massiven Sternen gebildet, bei Temperaturen von  $k_{\text{B}}T = 25 \text{ keV}$  und  $k_{\text{B}}T = 90 \text{ keV}$ . Netzwerkrechnungen haben gezeigt, dass bei Verwendung der bisherigen evaluierten Datenlage Gallium zu den am stärksten überproduzierten Elementen im Vergleich zu den solaren Häufigkeiten gehört. Außerdem zeigen Sensitivitätsstudien, dass Variationen in den Wirkungsquerschnitten auch Auswirkungen auf die nachfolgenden elementaren Häufigkeiten im schwachen s-Prozess haben.

Da die bisherige experimentelle Datenlage größtenteils aus Aktivierungsmessungen bei  $k_{\text{B}}T = 25 \text{ keV}$  entstanden ist, und einzelne Messungen zueinander Abweichungen bis zu einem Faktor von drei aufzeigen, wurde das in dieser Arbeit beschriebene Experiment stattdessen an der n\_TOF Anlage am CERN mit der Flugzeitmethode durchgeführt. Diese ermöglicht die Bestimmung differentieller Neutroneneinfangwirkungsquerschnitte. Die in einer Spallationsquelle produzierten Neutronenpulse interagieren nach ungefähr 180 m Flugweg mit der jeweiligen Gallium Probe. Die prompten Photonen aus der Abregungskaskade der produzierten Tochterkerne wurden mit vier organischen  $\text{C}_6\text{D}_6$  Flüssigszintillationsdetektoren gemessen.

Mithilfe von Messungen mit verschiedenen Kalibrationsquellen wurde anhand der Compton-Kanten die Photonenenergiekalibration durchgeführt. Die Messdaten mit einer Goldprobe wurden genutzt, um mithilfe der wohlbekannten Neutroneneinfangsresonanzen von Gold die Umrechnung von Flugzeit zu Neutronenenergie mit

einer Unsicherheit  $< 1\%$  zu bestimmen. Dedizierte Messungen bei ausgeschaltetem Neutronenstrahl beziehungsweise mit einem leeren Probenhalter bei eingeschaltetem Neutronenstrahl ermöglichten den Abzug der umgebungs- und strahlinduzierten Hintergrundkomponenten von den Messdaten. Der Einfluss elastisch gestreuter Neutronen auf die Messdaten wurde mit aus den evaluierten Wirkungsquerschnitten bestimmten Korrekturfaktoren abgeschätzt. Für die Effizienzkorrektur der Detektorsignale wurden Monte Carlo Simulationen bei verschiedenen Photonenenergien durchgeführt. Aus den gewonnenen Spektren wurde eine  $\gamma$ -energieabhängige Gewichtungsfunktion bestimmt, mithilfe derer gemäß der *Pulse Height Weighting Methode* die experimentellen Daten mit einer Unsicherheit von ungefähr 3,5% effizienzkorrigiert werden konnten. Der integrierte Neutronenfluss wurde aus Kombination des evaluierten n\_TOF Neutronenflussprofils und der gesättigten Goldresonanzmethode ermittelt.  $^{197}\text{Au}$  besitzt bei 4,9 eV eine starke Neutroneneinfangsresonanz, so dass alle die Probe passierenden Neutronen dieser Energie mit ihr interagieren. Das Neutronenflussprofil lässt sich damit skalieren und liefert den integrierten Neutronenfluss über den gesamten gemessenen Energiebereich vom thermischen bis zu mehreren hundert keV.

Die in dieser Arbeit ermittelten differentiellen Wirkungsquerschnitte für den Neutroneneinfang von  $^{69}\text{Ga}$  und  $^{71}\text{Ga}$  sind in Abbildung 8.1 und Abbildung 8.2 dargestellt, und mit den evaluierten Daten aus ENDF/B-VIII.0 [43] verglichen. Des Weiteren wurden für astrophysikalisch relevante Energien die nach der Maxwell-Boltzmann-Verteilung gemittelten Wirkungsquerschnitte (*MACS*) bestimmt. Diese sind in Abbildung 8.3 und Abbildung 8.4 gezeigt.



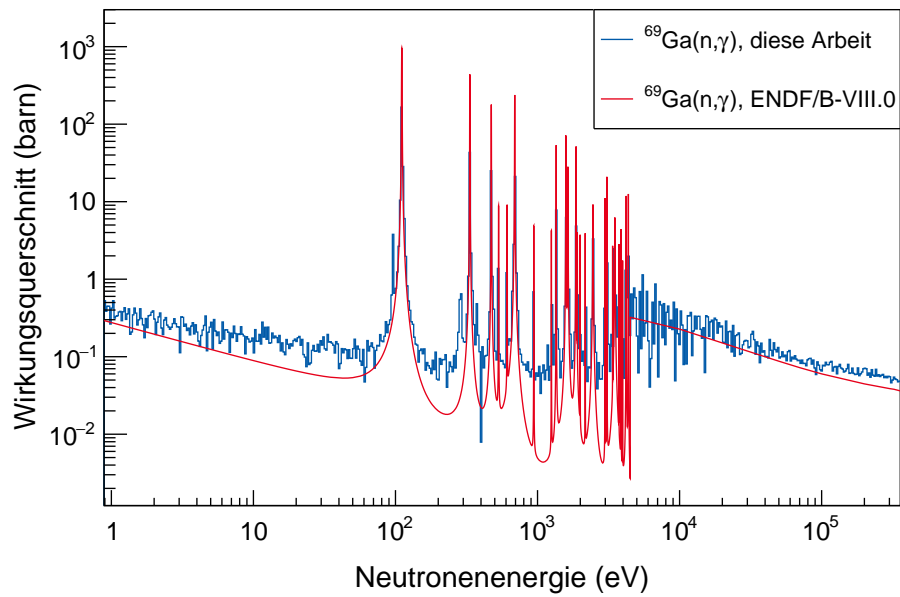


Abbildung 8.1.: Der differentielle  $^{69}\text{Ga}(n, \gamma)$  Neutroneneinfangwirkungsquerschnitt, verglichen mit den evaluierten ENDF Daten [43].

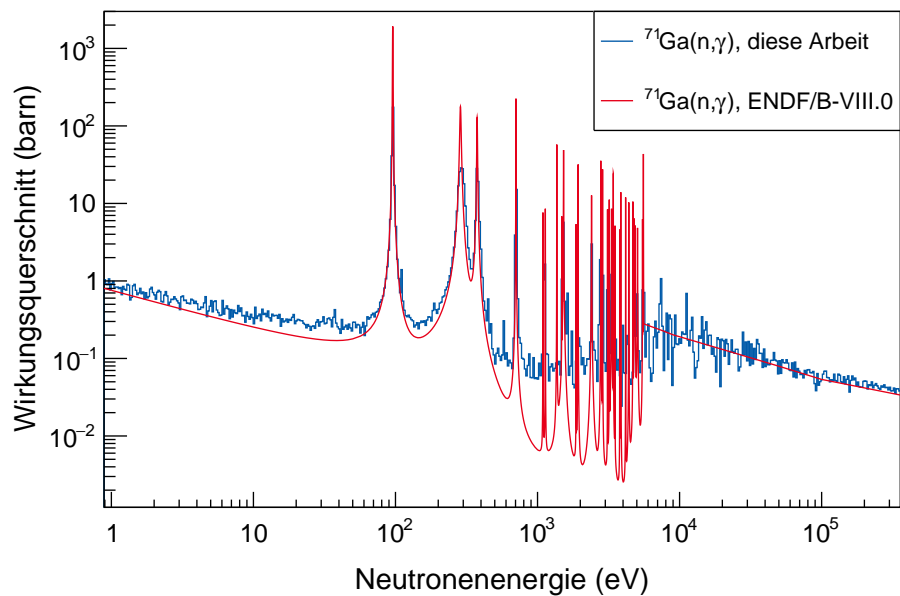
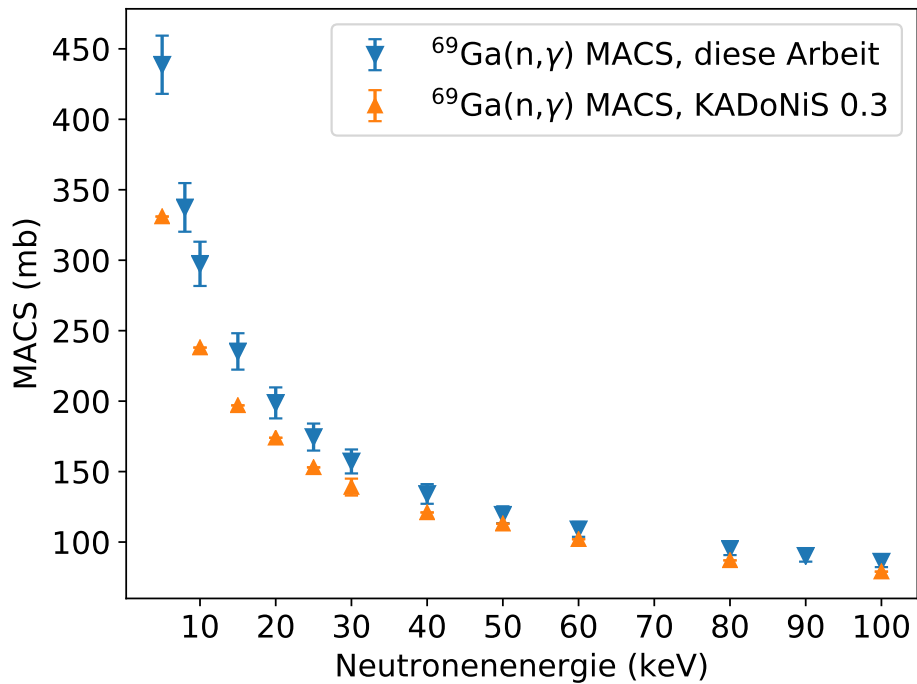


Abbildung 8.2.: Der differentielle  $^{71}\text{Ga}(n, \gamma)$  Neutroneneinfangwirkungsquerschnitt, verglichen mit den evaluierten ENDF Daten [43].

Während die Resultate für  $^{71}\text{Ga}$  größtenteils gute Übereinstimmung mit den evaluierten Daten aus KADoNiS v0.3 [14] zeigen, ist für  $^{69}\text{Ga}$  eine stärkere Abweichung zu sehen.



**Abbildung 8.3.:** Die  $^{69}\text{Ga}(n,\gamma)$  Werte aus dieser Arbeit, verglichen mit den evaluierten Daten aus KADoNiS v0.3 [14].

Ähnliche Diskrepanzen konnten auch in kürzlich durchgeführten Aktivierungsmessungen beobachtet werden [59, 60]. Insbesondere der totale und Streuquerschnitts sollten mithilfe weiterer Messungen genau bestimmt werden, da Streueffekte ersten Abschätzungen zufolge einen nicht vernachlässigbaren, systematischen Einfluss auf die bestimmten Neutroneneinfangwirkungsquerschnitte haben.

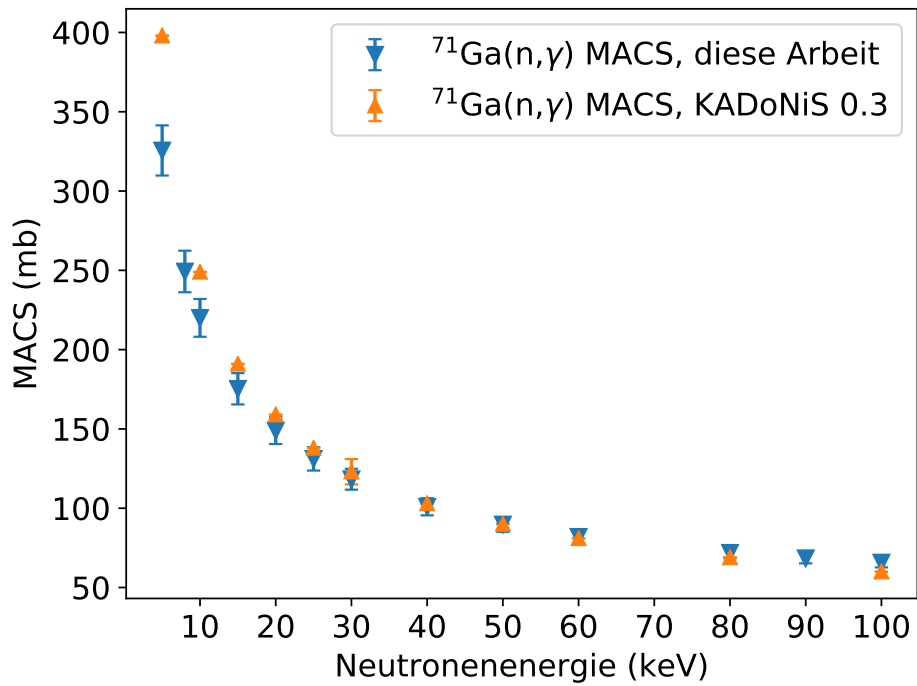


Abbildung 8.4.: Die  $^{71}\text{Ga}(n,\gamma)$  Werte aus dieser Arbeit, verglichen mit den evaluierten Daten aus KADoNiS v0.3 [14]



## A.1. Uncertainty calculation

In all physical measurements, the true value of the measured variable is affected by two kinds of uncertainties. The *statistical* uncertainty is an inherent byproduct of statistical processes like the decay of radioactive nuclei, or reactions between particles. The average of all measurements will converge towards the true value for increased number of repetitions, making high counting statistics desirable. On the other hand, *systematic* uncertainties are often caused by insufficient calibrations or user errors. Such uncertainties will repeat for any number of repeated measurements, and will not be reduced by increased statistics.

Since most quantities of interest need to be calculated from the measured variables, the total uncertainty  $u_y$  of result  $y$  can be calculated from the individual uncertainties  $u_i$  of the contributing measured variables  $x_i$ , such that

$$u_y = \sqrt{\sum_{i=1}^n \left( \frac{\partial y}{\partial x_i} \cdot u_i \right)^2}. \quad (\text{A.1})$$

However, this only holds true for independent variables  $x_i$ . If a correlation between two variables  $x_i$  and  $x_j$  exists, their covariance  $u(x_i, x_j)$  needs to be included

$$u_y = \sqrt{\sum_{i=1}^n \left( \frac{\partial y}{\partial x_i} \cdot u_i \right)^2 + 2 \sum_{i=1}^{n-1} \sum_{j=i+1}^n \left( \frac{\partial y}{\partial x_i} \right) \left( \frac{\partial y}{\partial x_j} \right) u(x_i, x_j)}. \quad (\text{A.2})$$

## A.2. Chemical sample composition

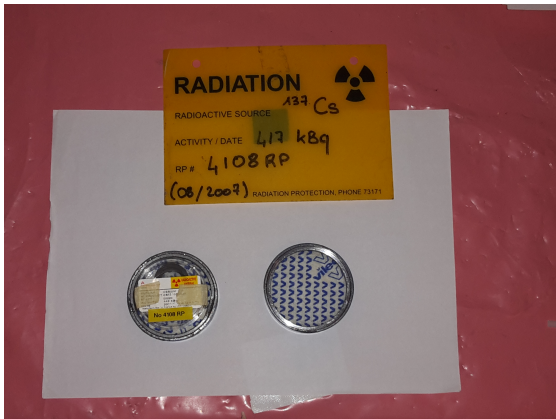
Element	Content (ppm)	Element	Content (ppm)
Li	< 0.4	Cd	0.32
Be	< 0.04	Sn	13.50
B	< 4	Sb	0.16
Na	< 40	Te	< 0.4
Mg	< 2	Cs	< 0.04
Al	< 4	Ba	0.14
Si	< 40	La	< 0.04
P	< 40	Ce	< 0.04
K	< 40	Pr	< 0.04
Ca	< 40	Nd	0.12
Sc	< 0.4	Sm	< 0.04
Ti	< 0.4	Eu	< 0.04
V	< 4	Gd	< 0.04
Cr	< 4	Tb	< 0.04
Mn	1.0	Dy	< 0.04
Fe	< 40	Ho	< 0.04
Co	< 0.2	Er	< 0.04
Ni	< 0.4	Tm	< 0.04
Cu	< 12.6	Yb	< 0.04
Zn	< 12	Lu	< 0.04
Ge	< 0.4	Hf	< 0.2
As	< 4	Ta	< 0.2
Se	< 4	W	< 0.2
Rb	0.08	Re	< 0.2
Sr	< 0.04	Ir	< 0.2
Y	< 0.04	Pt	119.6
Zr	< 0.04	Au	< 0.2
Nb	< 0.04	Hg	< 0.2
Mo	0.04	Tl	< 0.04
Ru	0.06	Pb	3.44
Rh	< 0.04	Bi	< 0.04
Ag	< 0.04	Th	< 0.04
Pd	2.70	U	< 0.04

Table A.1.: Chemical analysis of  $^{69}\text{Ga}$  sample admixtures, extracted from [27].

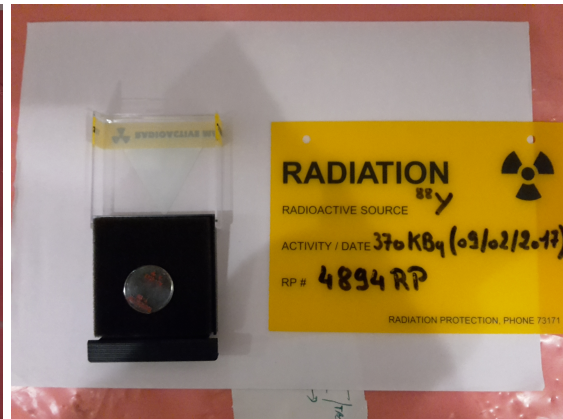
Element	Content (ppm)	Element	Content (ppm)
K	< 50	Cu	< 1
Na	< 20	Pb	< 1
Ca	< 50	B	< 10
Mg	< 3	P	< 50
Fe	< 50	Se	< 20
Al	< 3	Br	< 50
Si	< 50	Sn	1
Cr	< 10	Ag	< 1
Ni	< 1	Zn	< 2

**Table A.2.:** Chemical analysis of  $^{71}\text{Ga}$  sample admixtures, extracted from [28].

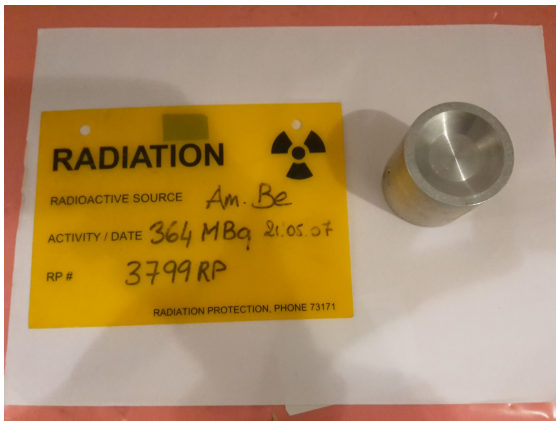
### A.3. Calibration sources



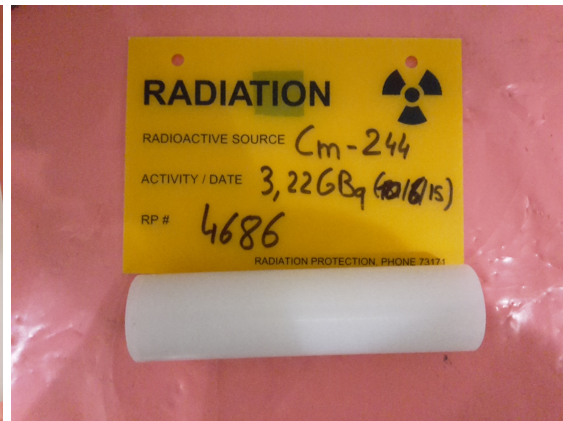
(a)  $^{137}\text{Cs}$



(b)  $^{88}\text{Y}$



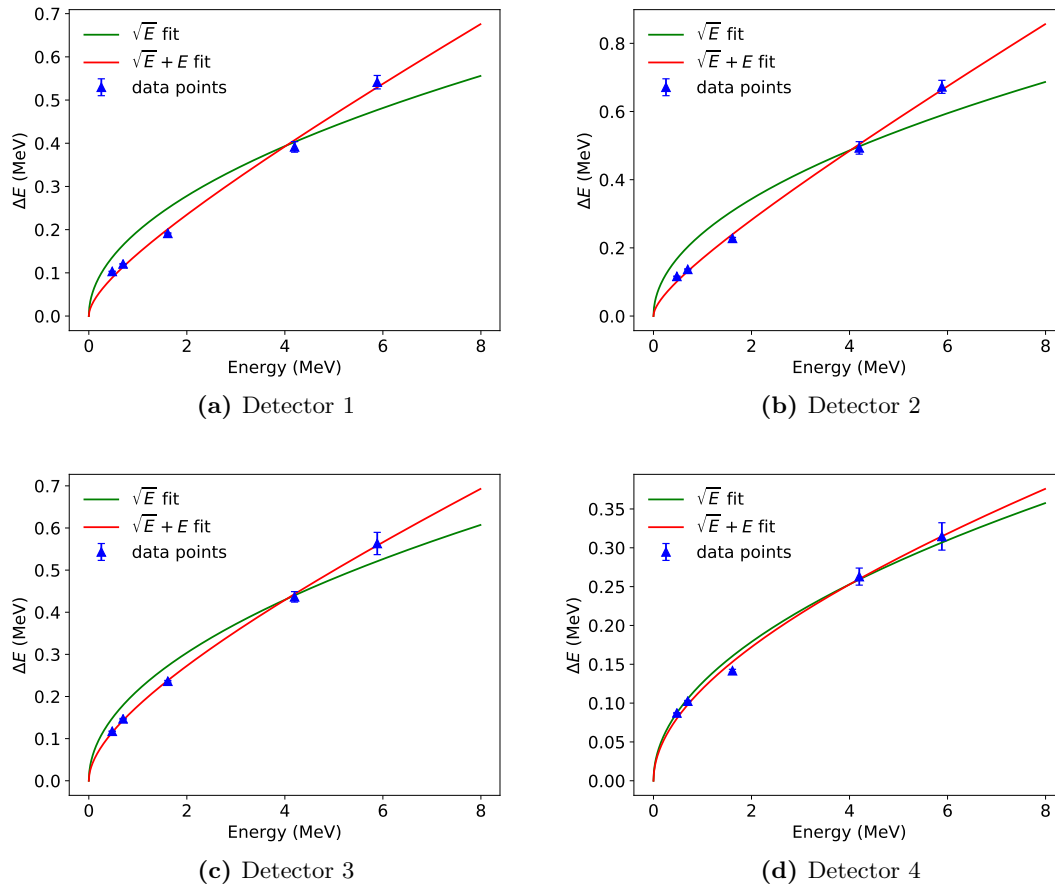
(c) AmBe



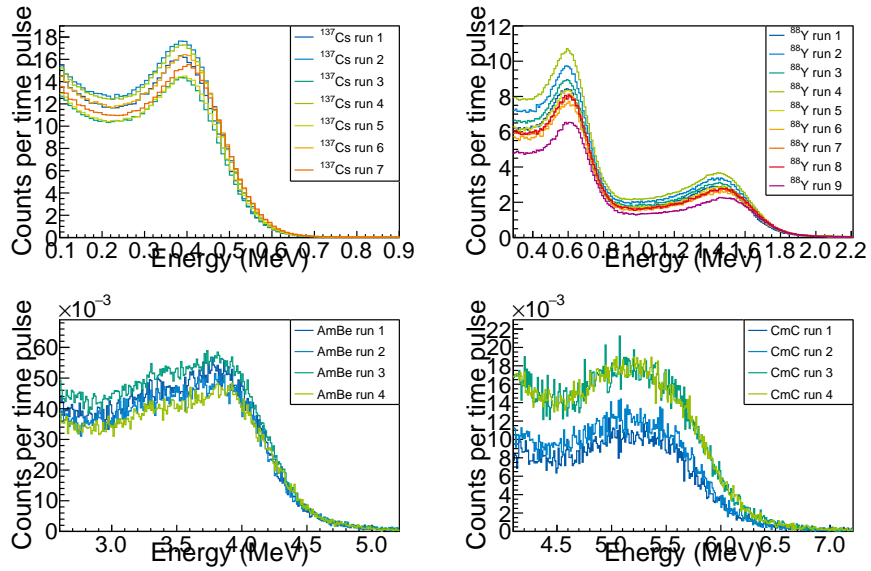
(d) CmC

Figure A.1.: Calibration sources used in this measurement campaign.

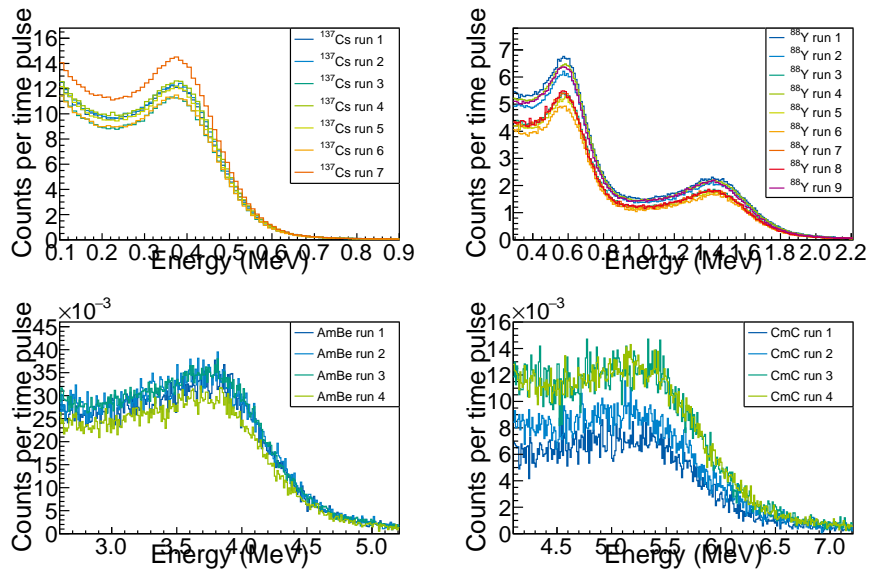




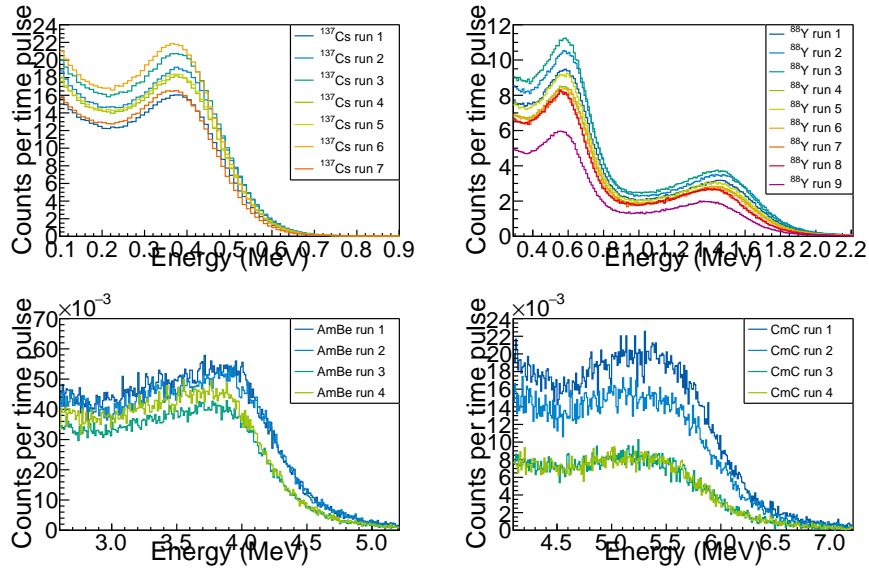
**Figure A.2.:** Fit of the energy resolution for all four detectors, derived from the broadening of the Compton edges of the calibration source data. The  $\sqrt{E} + E$  fit was chosen due to its much better agreement with the data.



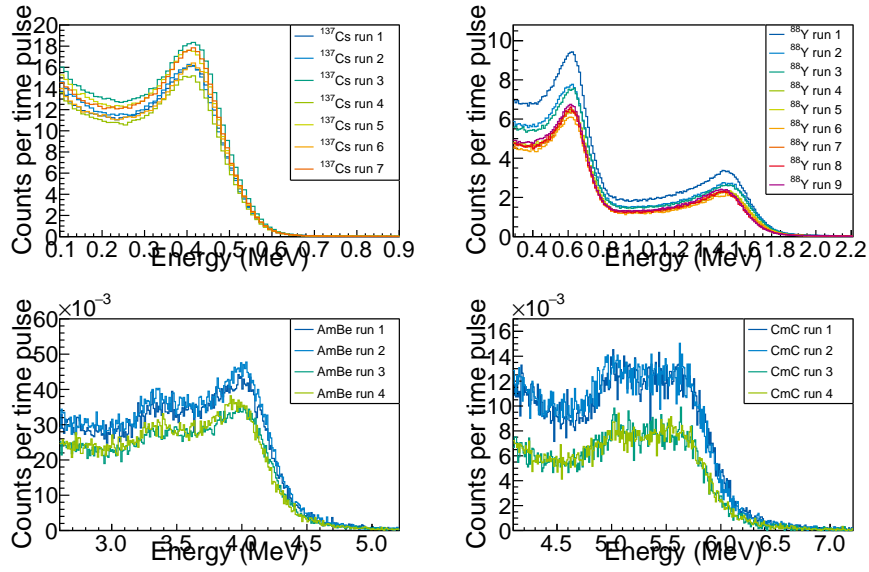
(a) Detector 1



(b) Detector 2

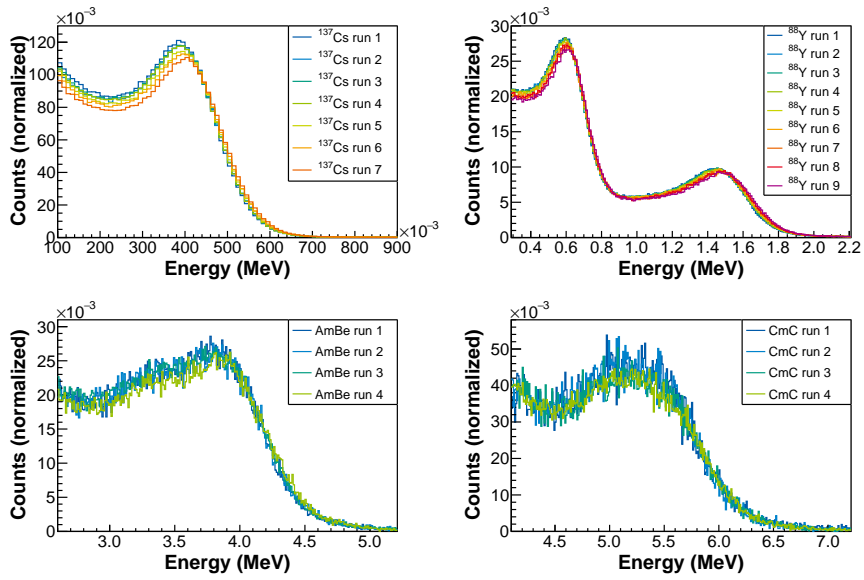


(a) Detector 3

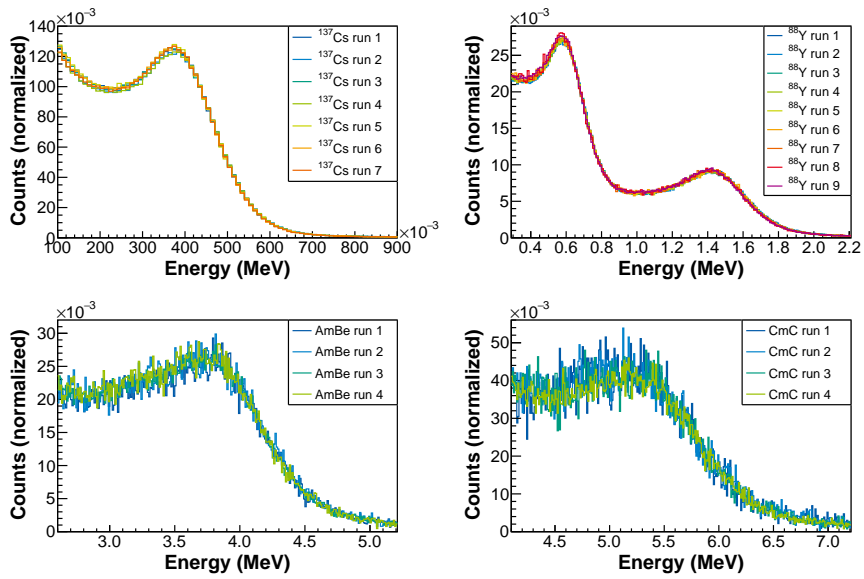


(b) Detector 4

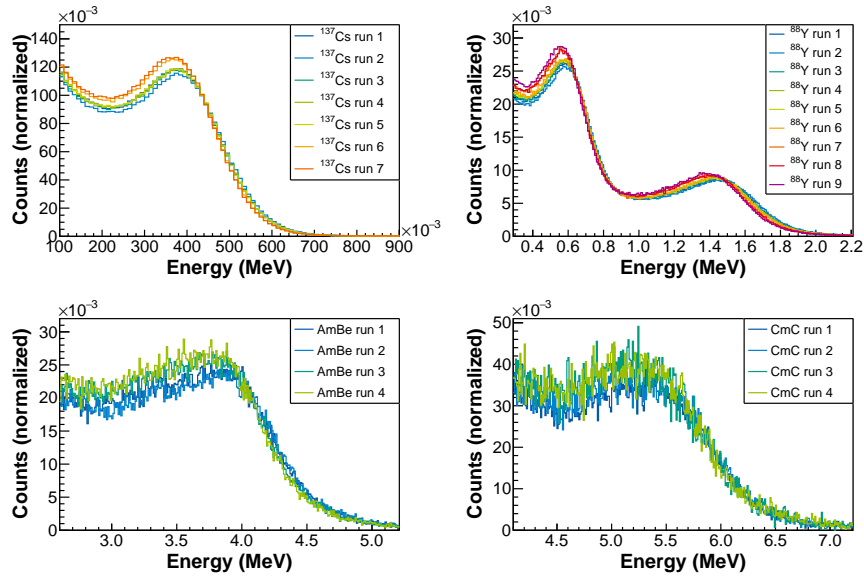
**Figure A.4.:** Amplitude spectra across campaign for all detectors, normalized to measurement time.



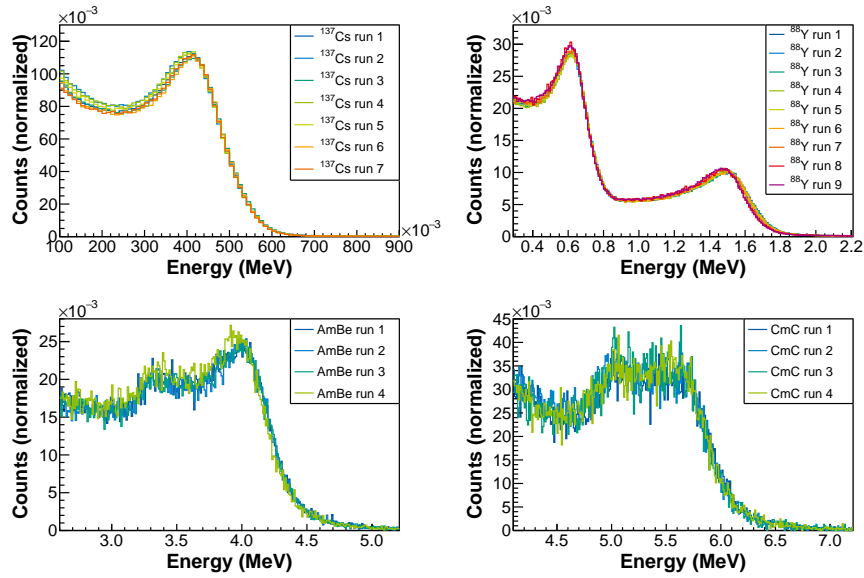
(a) Detector 1



(b) Detector 2



(a) Detector 3



(b) Detector 4

Figure A.6.: Amplitude spectra across campaign for all detectors, normalized to number of counts in the energy region around the Compton edge.

## A.4. Monitor consistency

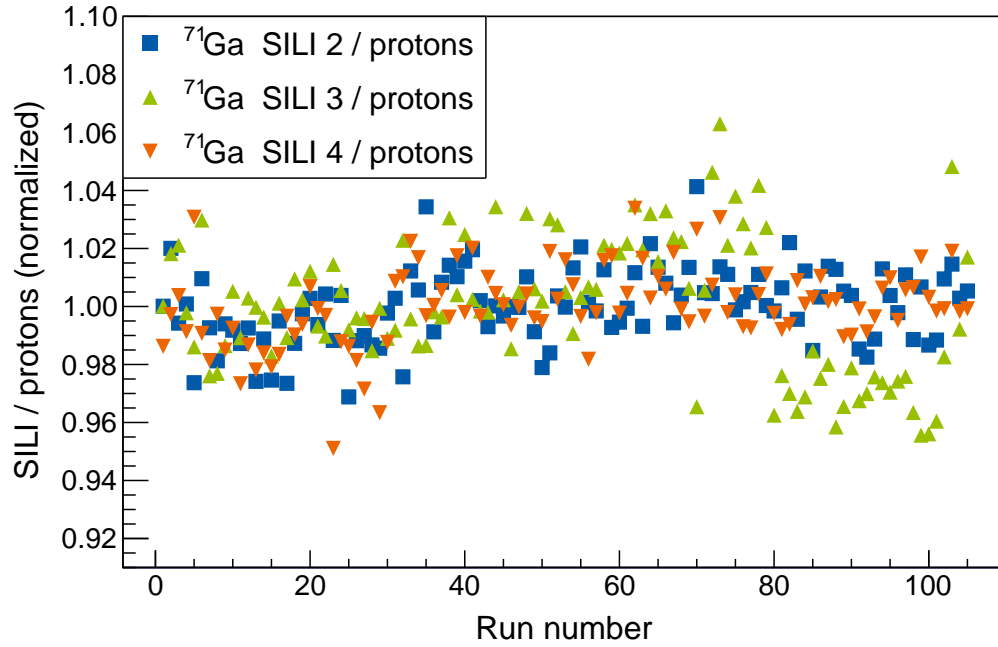


**Figure A.7.:** Ratios of beam monitor counts across all  $^{71}\text{Ga}$  runs, normalized to the respective average across all runs, after removing the outlier SILI 1.

## A.5. Rebound effect

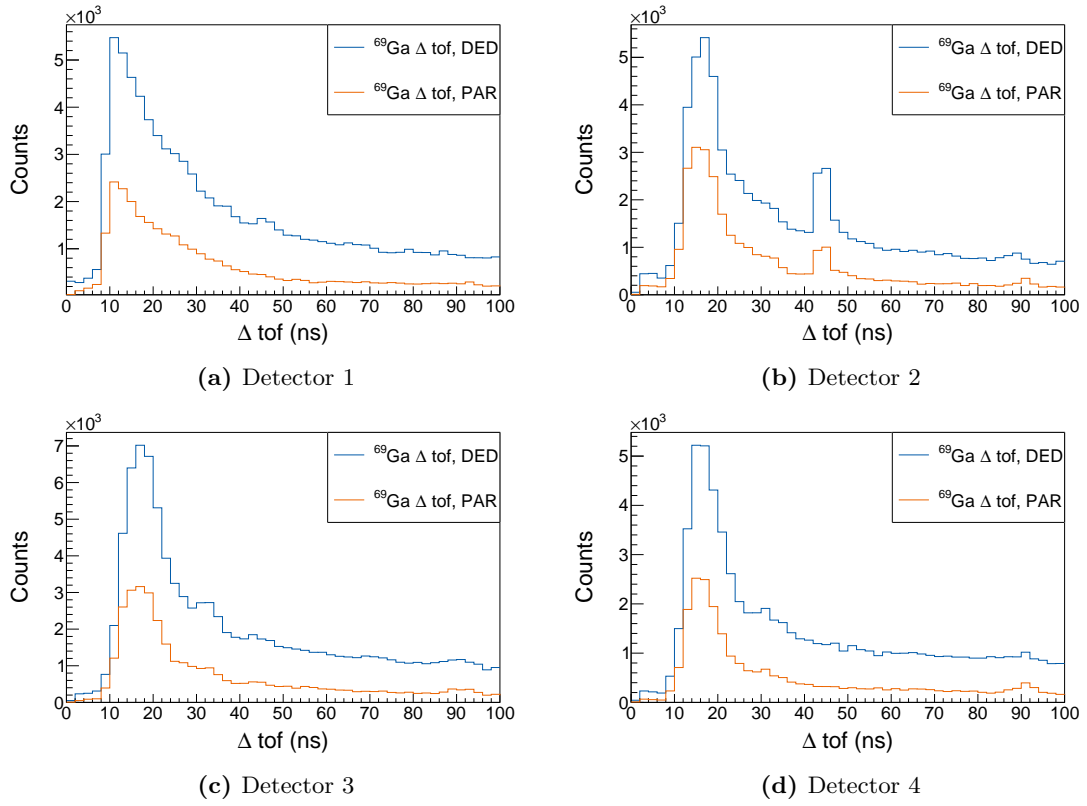


**Figure A.8.:** Distribution of time difference between consecutive events for  $^{69}\text{Ga}$  in each  $\text{C}_6\text{D}_6$  detector, with a clear lower bound at 20 ns. A rebound signal is noticeable, especially in detector 2.

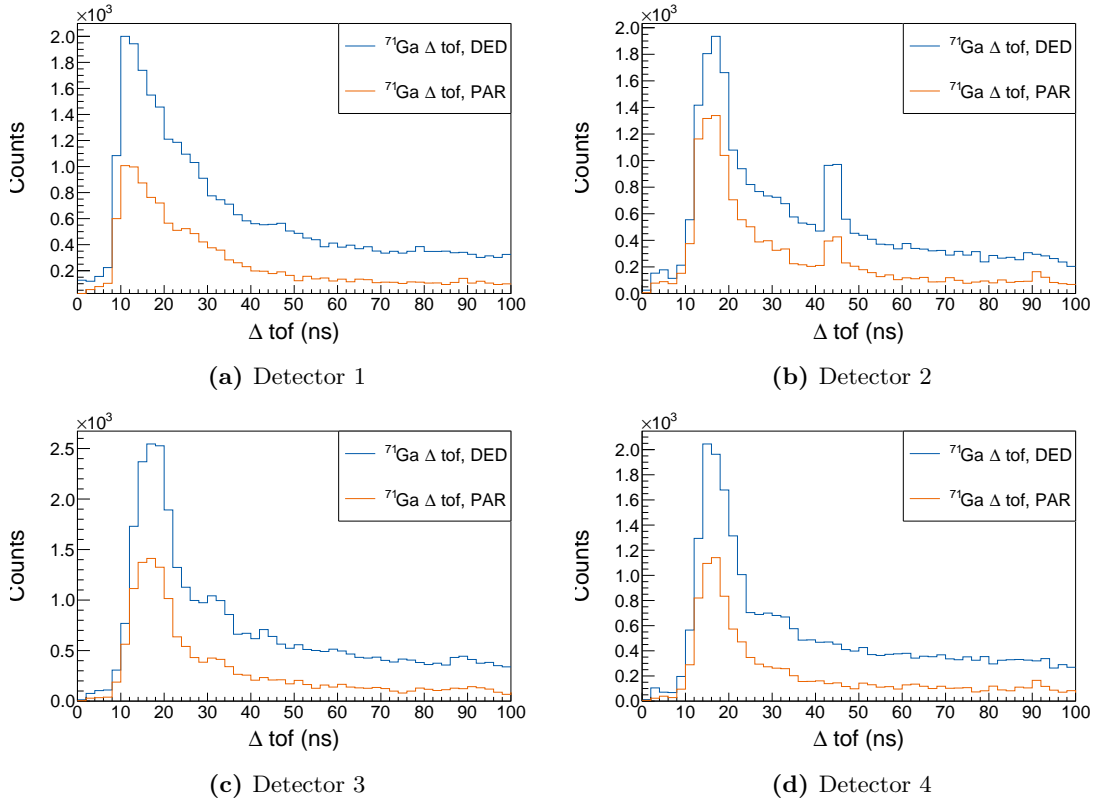


**Figure A.9.:** Distribution of time difference between consecutive events for  $^{71}\text{Ga}$  in each  $\text{C}_6\text{D}_6$  detector, with a clear lower bound at 20 ns. A rebound signal is noticeable, especially in detector 2.



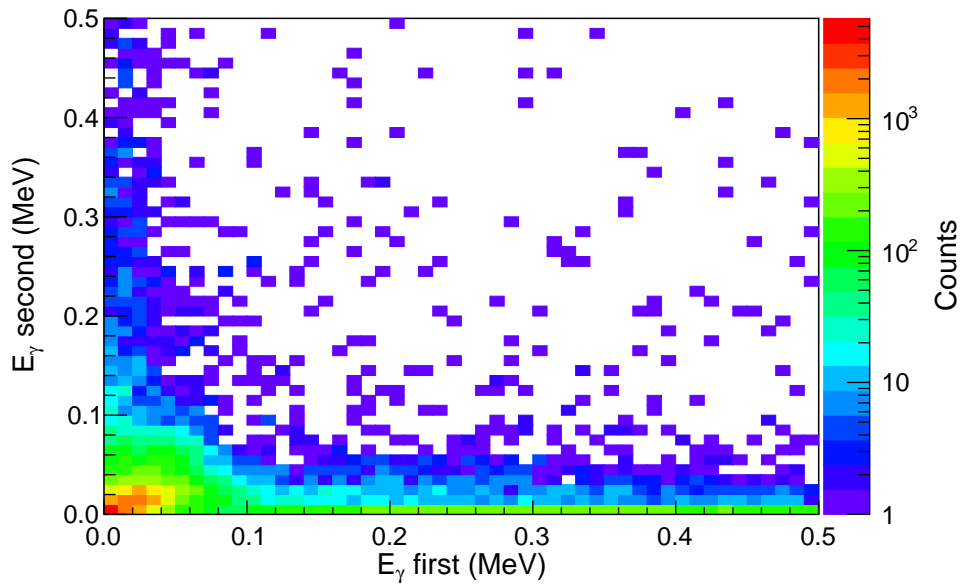


**Figure A.10.:** Zoom on low energy region of the  $^{71}\text{Ga}$   $\Delta t$ -window for detector 2, which had the strongest rebound effects. A  $\gamma$ -energy threshold of 100 keV would remove the majority of these rebound and other background effects, and was therefore applied to all data.

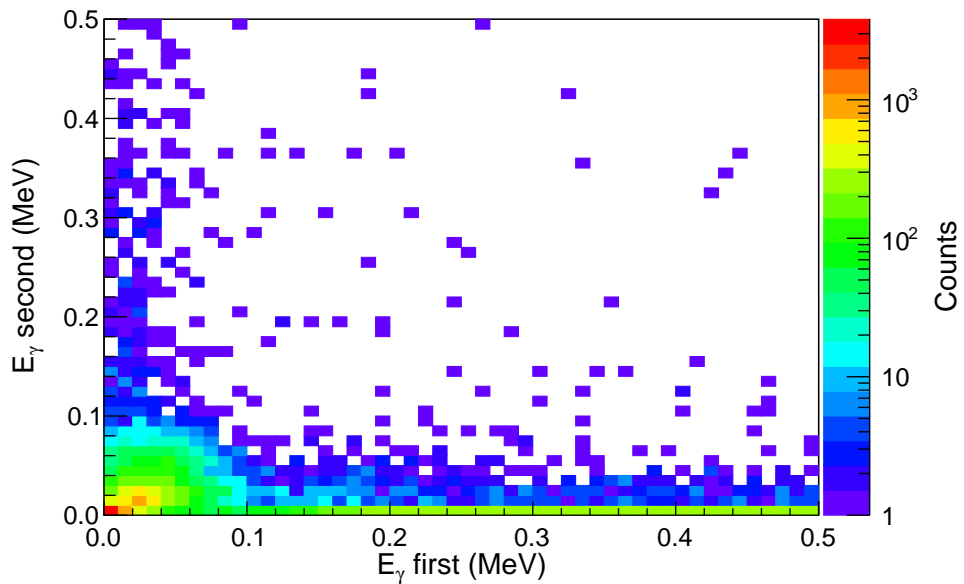
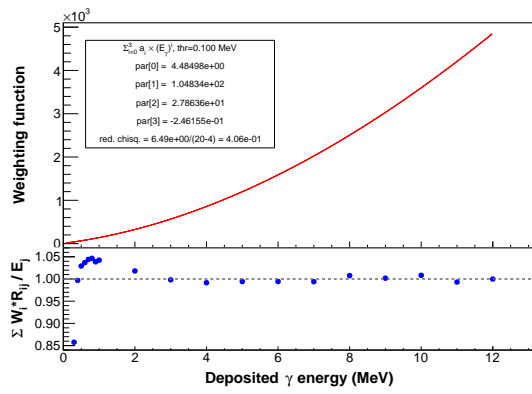
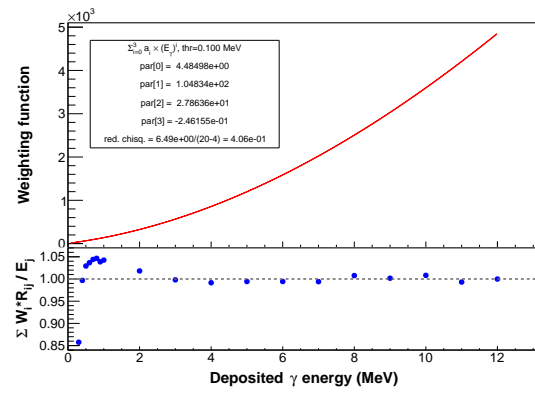


**Figure A.11.:** Zoom on low energy region of the  $^{197}\text{Au}$   $\Delta t$ -window for detector 2, which had the strongest rebound effects. A  $\gamma$ -energy threshold of 100 keV would remove the majority of these rebound and other background effects, and was therefore applied to all data.

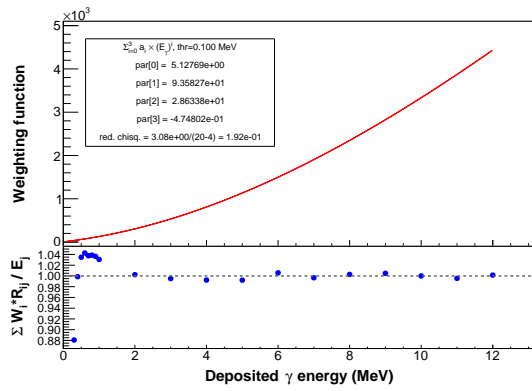
## A.6. PHWT



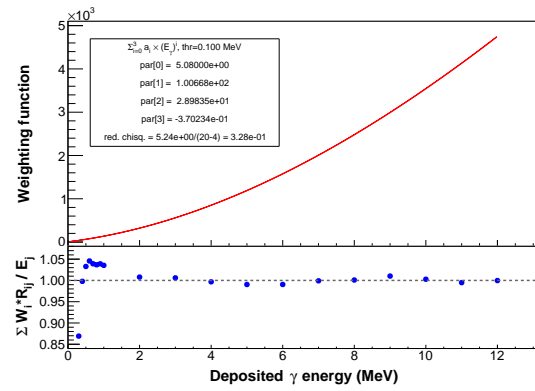
(a) Detector 1



(b) Detector 2



(c) Detector 3



(d) Detector 4

Figure A.12.: Weighting function, excluding 200 keV outlier.

LIST OF FIGURES
-----------------

1.1. Solar abundances . . . . .	2
1.2. Weak s process sensitivities . . . . .	8
2.1. Time of flight technique . . . . .	15
2.2. C <sub>6</sub> D <sub>6</sub> detector . . . . .	21
3.1. Sample production frame . . . . .	23
3.2. Capture sample frame . . . . .	25
4.1. CERN accelerator complex . . . . .	27
4.2. In-beam photon time of flight distribution . . . . .	28
4.3. In-beam photon energy distribution . . . . .	29
4.4. Capture setup overview . . . . .	30
4.5. Sample exchanger . . . . .	31
4.6. Beam profile . . . . .	32
5.1. Compton edge gaussian fits . . . . .	35
5.2. Channel to energy conversion . . . . .	37
5.3. Energy resolution . . . . .	38
5.4. Beam monitor evaluation . . . . .	39
5.5. Beam monitor consistency . . . . .	40
5.6. Calibration source spectra over time . . . . .	41
5.7. Detector correlation in calibration source data . . . . .	42
5.8. Normalized calibration source data over time . . . . .	43
5.9. ToF to neutron energy conversion . . . . .	45
5.10. $\gamma$ -flash width . . . . .	46
5.11. Consecutive event time distribution . . . . .	47

5.12. Dead time correction factors . . . . .	48
5.13. Deposited energy relation between rebound signals . . . . .	49
5.14. Low energy distribution of rebound events . . . . .	50
5.15. Ambient background subtraction . . . . .	51
5.16. Beam on empty frame background component . . . . .	52
5.17. Scattering to neutron capture ratio for gallium and lead . . . . .	53
5.18. Estimation of gallium scattering component from scaled lead data . .	54
5.19. Gallium scattering correction factors from simulations . . . . .	55
5.20. GEANT4 detector simulation . . . . .	58
5.21. Simulated detector responses . . . . .	59
5.22. Weighting function for Pulse Height Weighting . . . . .	60
5.23. Evaluated n_TOF neutron flux profile . . . . .	62
5.24. Saturated resonance in gold data for flux normalization . . . . .	63
5.25. Uncertainty due to PHWT for $^{69}\text{Ga}$ data . . . . .	65
5.26. Uncertainty due to PHWT for $^{71}\text{Ga}$ data . . . . .	66
5.27. Observable resonances due to gallium impurities . . . . .	67
5.28. Impurity subtraction in resolved resonance region . . . . .	68
6.1. Differential $^{69}\text{Ga}(n, \gamma)$ cross section . . . . .	70
6.2. Differential $^{71}\text{Ga}(n, \gamma)$ cross section . . . . .	71
6.3. MACS impurity correction . . . . .	72
6.4. MACS scattering correction . . . . .	73
6.5. Comparison with $^{69}\text{Ga}$ KADoNiS values . . . . .	75
6.6. Comparison with $^{71}\text{Ga}$ KADoNiS values . . . . .	76
8.1. Differentieller $^{69}\text{Ga}(n, \gamma)$ Neutroneneinfangwirkungsquerschnitt . . . .	81
8.2. Differentieller $^{71}\text{Ga}(n, \gamma)$ Neutroneneinfangwirkungsquerschnitt . . . .	81
8.3. Vergleich mit $^{69}\text{Ga}$ KADoNiS Wirkungsquerschnitten . . . . .	82
8.4. Vergleich mit $^{71}\text{Ga}$ KADoNiS Wirkungsquerschnitten . . . . .	83
A.1. Calibration sources . . . . .	87
A.2. Energy resolutions . . . . .	88
A.4. Calibration source spectra over time . . . . .	90
A.6. Normalized calibration source data over time . . . . .	92
A.7. Beam monitor ratios . . . . .	93
A.8. Consecutive event time distribution $^{69}\text{Ga}$ . . . . .	94
A.9. Consecutive event time distribution $^{71}\text{Ga}$ . . . . .	95
A.10. Low energy distribution of rebound events $^{71}\text{Ga}$ . . . . .	96

A.11.Low energy distribution of rebound events $^{197}\text{Au}$ . . . . .	96
A.12.Weighting function for Pulse Height Weighting, all detectors . . . . .	97

LIST OF TABLES
----------------

3.1. Gallium cross contaminations . . . . .	23
3.2. Gallium sample masses . . . . .	24
5.1. Calibration sources . . . . .	34
5.2. $^{197}\text{Au}$ resonances for time of flight to energy conversion . . . . .	44
5.3. Evaluated flux uncertainties . . . . .	61
5.4. Beam interception factors . . . . .	63
6.1. $^{69}\text{Ga}$ MACS values . . . . .	70
6.2. $^{71}\text{Ga}$ MACS values . . . . .	71
6.3. Gallium MACS normalized to gold at $k_{\text{B}}T = 25\text{ keV}$ . . . . .	76
A.1. Chemical analysis of $^{69}\text{Ga}$ . . . . .	85
A.2. Chemical analysis of $^{71}\text{Ga}$ . . . . .	86

## BIBLIOGRAPHY

- [1] E. Margaret Burbidge, G. R. Burbidge, William A. Fowler, and F. Hoyle. “Synthesis of the Elements in Stars”. In: *Rev. Mod. Phys.* 29 (4 Oct. 1957), pp. 547–650. DOI: 10.1103/RevModPhys.29.547. URL: <https://link.aps.org/doi/10.1103/RevModPhys.29.547>.
- [2] Katharina Lodders. “Solar System Abundances and Condensation Temperatures of the Elements”. In: *The Astrophysical Journal* 591.2 (2003), pp. 1220–1247. DOI: 10.1086/375492. URL: <https://doi.org/10.1086/375492>.
- [3] Christian Iliadis. *Nuclear Physics of Stars*. 2007. DOI: 10.1002/9783527692668.
- [4] P. A. Seeger, W. A. Fowler, and D. D. Clayton. “Nucleosynthesis of Heavy Elements by Neutron Capture.” In: *The Astrophysical Journal, Supplement* 11 (Feb. 1965), p. 121. DOI: 10.1086/190111.
- [5] R Reifarth, C Lederer, and F Käppeler. “Neutron reactions in astrophysics”. In: *Journal of Physics G: Nuclear and Particle Physics* 41.5 (Mar. 2014), p. 053101. DOI: 10.1088/0954-3899/41/5/053101. URL: <https://doi.org/10.1088/0954-3899/41/5/053101>.
- [6] Roberto Gallino, Claudio Arlandini, Maurizio Busso, Maria Lugaro, Claudia Travaglio, Oscar Straniero, Alessandro Chieffi, and Marco Limongi. “Evolution and Nucleosynthesis in Low-Mass Asymptotic Giant Branch Stars. II. Neutron Capture and the s-Process”. In: *The Astrophysical Journal* 497.1 (Apr. 1998), pp. 388–403. DOI: 10.1086/305437. URL: <https://doi.org/10.1086/305437>.
- [7] Falk Herwig. “Evolution and Yields of Extremely Metal-poor Intermediate-Mass Stars”. In: *The Astrophysical Journal Supplement Series* 155.2 (Dec. 2004), pp. 651–666. DOI: 10.1086/425419. URL: <https://doi.org/10.1086/425419>.
- [8] M. Pignatari, R. Gallino, M. Heil, M. Wiescher, F. Käppeler, F. Herwig, and S. Bisterzo. “The Weak s-Process in Massive Stars and its Dependence on the Neutron Capture Cross Sections”. In: *The Astrophysical Journal* 710 (Feb. 2010), pp. 1557–1577. DOI: 10.1088/0004-637X/710/2/1557.

- [9] M. Weigand, T. A. Bredeweg, A. Couture, et al. “ $^{63}\text{Ni} (n, \gamma)$  cross sections measured with DANCE”. In: *Physical Review C* 92.4, 045810 (Oct. 2015), p. 045810. DOI: 10.1103/PhysRevC.92.045810.
- [10] N. Prantzos, M. Hashimoto, and K. Nomoto. “The s-process in massive stars : yields as a function of stellar mass and metallicity.” In: *Astronomy and Astrophysics* 234 (Aug. 1990), p. 211.
- [11] A Arcones and F-K Thielemann. “Neutrino-driven wind simulations and nucleosynthesis of heavy elements”. In: *Journal of Physics G: Nuclear and Particle Physics* 40.1 (Nov. 2012), p. 013201. DOI: 10.1088/0954-3899/40/1/013201. URL: <https://doi.org/10.1088/0954-3899/40/1/013201>.
- [12] C. Freiburghaus, S. Rosswog, and F.-K. Thielemann. “[CLC][ITAL]r[/ITAL][[/CLC]-Process in Neutron Star Mergers”. In: *The Astrophysical Journal* 525.2 (Nov. 1999), pp. L121–L124. DOI: 10.1086/312343. URL: <https://doi.org/10.1086/312343>.
- [13] Daniel M Siegel. “GW170817—the first observed neutron star merger and its kilonova: Implications for the astrophysical site of the r-process”. In: *The European Physical Journal A* 55.11 (2019), pp. 1–20.
- [14] I. Dillmann, R. Plag, F. Käppeler, and T. Rauscher. “KADoNiS v0.3 - The third update of the “Karlsruhe Astrophysical Database of Nucleosynthesis in Stars””. In: *Proceedings of the workshop “EFNUDAT Fast Neutrons - scientific workshop on neutron measurements, theory & applications”*, Geel, Belgium (2009).
- [15] C Guerrero, S Altstadt, S Andriamonje, et al. “Performance of the neutron time-of-flight facility n\_TOF at CERN”. In: *Eur. Phys. J. A* 49 (2013), 27. 15 p. DOI: 10.1140/epja/i2013-13027-6. URL: <https://cds.cern.ch/record/1709388>.
- [16] B. Povh, K. Rith, C. Scholz, and F. Zetsche. *Teilchen und Kerne*. 8th ed. Springer-Verlag Berlin Heidelberg: Springer-Verlag, May 2008. ISBN: 978-3-540-68075-8.
- [17] Claus E. Rolfs and William S. Rodney. *Cauldrons in the Cosmos*. Chicago and London: University of Chicago Press, 1988. ISBN: 0-226-72457-3.
- [18] W. R. Leo. *Techniques for Nuclear and Particle Physics Experiments: A How to Approach*. 2nd ed. Springer Verlag Berlin Heidelberg New York, 1994. ISBN: 978-3-540-57280-0.
- [19] Glenn F. Knoll. *Radiation detection and measurement*. 2nd ed. John Wiley & Sons Ltd., 1989. ISBN: 0-471-81504-7.
- [20] René Reifarth, Philipp Erbacher, Stefan Fiebiger, et al. “Neutron-induced cross sections”. In: *The European Physical Journal Plus* 133.10 (2018), p. 424. DOI: 10.1140/epjp/i2018-12295-3. URL: <https://doi.org/10.1140/epjp/i2018-12295-3>.
- [21] M.C. Moxon and E.R. Rae. “A gamma-ray detector for neutron capture cross-section measurements”. In: *Nuclear Instruments and Methods* 24 (1963), pp. 445–455. ISSN: 0029-554X. DOI: [https://doi.org/10.1016/0029-554X\(63\)90364-1](https://doi.org/10.1016/0029-554X(63)90364-1). URL: <https://www.sciencedirect.com/science/article/pii/0029554X63903641>.



- [22] R. L. Macklin and J. H. Gibbons. “Capture-Cross-Section Studies for 30—220-keV Neutrons Using a New Technique”. In: *Phys. Rev.* 159 (4 1967), pp. 1007–1012. DOI: 10.1103/PhysRev.159.1007. URL: <https://link.aps.org/doi/10.1103/PhysRev.159.1007>.
- [23] P. E. Koehler, R. R. Winters, K. H. Guber, T. Rauscher, J. A. Harvey, S. Raman, R. R. Spencer, J. C. Blackmon, D. C. Larson, D. W. Bardayan, and T. A. Lewis. “High-resolution neutron capture and transmission measurements, and the stellar neutron-capture cross section of  $^{88}\text{Sr}$ ”. In: *Phys. Rev. C* 62 (5 2000), p. 055803. DOI: 10.1103/PhysRevC.62.055803. URL: <https://link.aps.org/doi/10.1103/PhysRevC.62.055803>.
- [24] K.H. Guber, L.C. Leal, R.O. Sayer, P.E. Koehler, T.E. Valentine, H. Derrien, and J.A. Harvey. “New neutron cross-section measurements at ORELA and their application in nuclear criticality calculations”. In: *Nuclear Instruments and Methods in Physics Research Section B: Beam Interactions with Materials and Atoms* 241.1 (2005). The Application of Accelerators in Research and Industry, pp. 218–222. ISSN: 0168-583X. DOI: <https://doi.org/10.1016/j.nimb.2005.07.083>. URL: <https://www.sciencedirect.com/science/article/pii/S0168583X05012085>.
- [25] Pierfrancesco Mastinu, Roberto Baccomi, Eric Berthoumieux, Daniel Cano-Ott, F Gramegna, Carlos Guerrero, Cristian Massimi, Paolo Maria Milazzo, Federica Mingrone, Javier Praena, G Prete, and Aczel Regino García. “New  $\text{C}_6\text{D}_6$  detectors: reduced neutron sensitivity and improved safety”. In: (2013). URL: <https://cds.cern.ch/record/1558147>.
- [26] R. Plag, M. Heil, F. Käppeler, P. Pavlopoulos, R. Reifarth, and K. Wisshak. “An optimized  $\text{C}_6\text{D}_6$  detector for studies of resonance-dominated  $(n,\gamma)$  cross-sections”. In: *Nuclear Instruments and Methods in Physics Research Section A: Accelerators, Spectrometers, Detectors and Associated Equipment* 496.2 (2003), pp. 425–436. ISSN: 0168-9002. DOI: [https://doi.org/10.1016/S0168-9002\(02\)01749-7](https://doi.org/10.1016/S0168-9002(02)01749-7). URL: <https://www.sciencedirect.com/science/article/pii/S0168900202017497>.
- [27] *Certificate of Analysis No. 5958*. San Francisco, Ca, USA: Isoflex USA, Dec. 2016.
- [28] *Certificate of Analysis No. 6803*. San Francisco, Ca, USA: Isoflex USA, Dec. 2016.
- [29] N. Colonna, A. Tsinganis, R. Vlastou, et al. “The fission experimental programme at the CERN n\_TOF facility: status and perspectives”. In: *The European Physical Journal A* 56.2 (Feb. 2020). This work is licensed under the Creative Commons Attribution 4.0 International License. To view a copy of this license, visit <http://creativecommons.org/licenses/by/4.0/>, p. 48. ISSN: 1434-601X. DOI: 10.1140/epja/s10050-020-00037-8. URL: <https://doi.org/10.1140/epja/s10050-020-00037-8>.
- [30] Collaboration n\_TOF. “The neutron Time-Of-Flight facility, n\_TOF, at CERN (I): Technical Description”. In: (Feb. 2013). First draft version. URL: <http://cds.cern.ch/record/1514680>.
- [31] Renilde Vanden Broeck. “THE CERN ACCELERATOR COMPLEX. Complexe des accélérateurs du CERN”. 2019. URL: <https://cds.cern.ch/record/2693837>.

- [32] F. Gunsing, O. Aberle, J. Andrzejewski, et al. “Nuclear data activities at the n\_TOF facility at CERN”. In: *The European Physical Journal Plus* 131.10 (Oct. 2016), p. 371. ISSN: 2190-5444. DOI: 10.1140/epjp/i2016-16371-4. URL: <https://doi.org/10.1140/epjp/i2016-16371-4>.
- [33] S. Meo, Miguel Cortés-Giraldo, Cristian Massimi, Jorge Lerendegui-Marco, M. Barbagallo, N. Colonna, C. Guerrero, Davide Mancusi, Federica Mingrone, José Quesada Molina, M. Sabaté-Gilarte, Gianni Vannini, and Vasilis Vlachoudis. “GEANT4 simulations of the n\_TOF spallation source and their benchmarking”. In: *The European Physical Journal A* 51 (Dec. 2015). DOI: 10.1140/epja/i2015-15160-6.
- [34] Davide Mancusi, Sergio Lo Meo, Nicola Colonna, Alain Boudard, Miguel Antonio Cortés-Giraldo, Joseph Cugnon, Jean-Christophe David, Sylvie Leray, Jorge Lerendegui-Marco, Cristian Massimi, and Vasilis Vlachoudis. “On the role of secondary pions in spallation targets”. In: *The European Physical Journal A* 53.5 (2017), p. 80. ISSN: 1434-601X. DOI: 10.1140/epja/i2017-12263-0. URL: <https://doi.org/10.1140/epja/i2017-12263-0>.
- [35] M. Bazioglou and J. Kalef-Ezra. “Dosimetry with radiochromic films: a document scanner technique, neutron response, applications”. In: *Applied Radiation and Isotopes* 55.3 (2001), pp. 339–345. ISSN: 0969-8043. DOI: [https://doi.org/10.1016/S0969-8043\(01\)00060-4](https://doi.org/10.1016/S0969-8043(01)00060-4). URL: <https://www.sciencedirect.com/science/article/pii/S0969804301000604>.
- [36] M Barbagallo, S Altstadt, S Andriamonje, et al. “High-accuracy determination of the neutron flux at n\_TOF”. In: *Eur. Phys. J. A* 49 (2013), 156. 11 p. DOI: 10.1140/epja/i2013-13156-x. URL: <https://cds.cern.ch/record/1709417>.
- [37] S. Marrone, P.F. Mastinu, U. Abbondanno, et al. “A low background neutron flux monitor for the n\_TOF facility at CERN”. In: *Nuclear Instruments and Methods in Physics Research Section A: Accelerators, Spectrometers, Detectors and Associated Equipment* 517.1 (2004), pp. 389–398. ISSN: 0168-9002. DOI: <https://doi.org/10.1016/j.nima.2003.09.060>. URL: <https://www.sciencedirect.com/science/article/pii/S0168900203028626>.
- [38] I. Murata, I. Tsuda, R. Nakamura, S. Nakayama, M. Matsumoto, and H. Miyamaru. “Neutron and gamma-ray source-term characterization of AmBe sources in Osaka University”. In: *Progress in Nuclear Science and Technology* 4 (2014), pp. 345–348. DOI: 10.15669/pnst.4.345. URL: [https://www.aesj.net/document/pnst004/345\\_348.pdf](https://www.aesj.net/document/pnst004/345_348.pdf).
- [39] J.K. Dickens and R.D. Baybarz. “A monoenergetic 6130-keV gamma-ray source for detector calibration”. In: *Nuclear Instruments and Methods* 85.1 (1970), pp. 143–145. ISSN: 0029-554X. DOI: [https://doi.org/10.1016/0029-554X\(70\)90133-3](https://doi.org/10.1016/0029-554X(70)90133-3). URL: <https://www.sciencedirect.com/science/article/pii/0029554X70901333>.
- [40] K.W. Geiger and L. Van der Zwan. “Neutrons and  $\gamma$ -rays from radioactive  $^{13}\text{C}(\alpha,n)$  sources”. In: *Nuclear Instruments and Methods* 157.1 (1978), pp. 199–201. ISSN: 0029-554X. DOI: [https://doi.org/10.1016/0029-554X\(78\)90607-9](https://doi.org/10.1016/0029-554X(78)90607-9). URL: <https://www.sciencedirect.com/science/article/pii/0029554X78906079>.

- [41] U Abbondanno, G Aerts, Héctor Álvarez Pol, et al. “New experimental validation of the pulse height weighting technique for capture cross-section measurements”. In: *Nuclear Instruments and Methods in Physics Research Section A: Accelerators, Spectrometers, Detectors and Associated Equipment* 521 (Apr. 2004), pp. 454–467. DOI: 10.1016/j.nima.2003.09.066.
- [42] G. Lorusso, N. Colonna, S. Marrone, et al. “Time–energy relation of the n\_TOF neutron beam: energy standards revisited”. In: *Nuclear Instruments and Methods in Physics Research Section A: Accelerators, Spectrometers, Detectors and Associated Equipment* 532 (Oct. 2004), pp. 622–630. DOI: 10.1016/j.nima.2004.04.247.
- [43] D.A. Brown, M.B. Chadwick, R. Capote, et al. “ENDF/B-VIII.0: The 8th Major Release of the Nuclear Reaction Data Library with CIELO-project Cross Sections, New Standards and Thermal Scattering Data”. In: *Nuclear Data Sheets* 148 (2018). Special Issue on Nuclear Reaction Data, pp. 1–142. ISSN: 0090-3752. DOI: <https://doi.org/10.1016/j.nds.2018.02.001>. URL: <https://www.sciencedirect.com/science/article/pii/S0090375218300206>.
- [44] Jorge Leredegui Marco. “Radiative neutron capture on  $^{242}\text{Pu}$ : addressing the target accuracies for innovative nuclear systems (Cross section measurements at the CERN n\_TOF and BRR neutron beams from thermal to 500 keV)”. Presented 15 Dec 2019. 2018. URL: <https://cds.cern.ch/record/2661485>.
- [45] S. Agostinelli, J. Allison, K. Amako, et al. “Geant4—a simulation toolkit”. In: *Nuclear Instruments and Methods in Physics Research Section A: Accelerators, Spectrometers, Detectors and Associated Equipment* 506.3 (2003), pp. 250–303. ISSN: 0168-9002. DOI: [https://doi.org/10.1016/S0168-9002\(03\)01368-8](https://doi.org/10.1016/S0168-9002(03)01368-8). URL: <https://www.sciencedirect.com/science/article/pii/S0168900203013688>.
- [46] J. Leredegui-Marco, C. Guerrero, J.M. Quesada, and M Cortes. “A GEANT4 application for planning and analysis of  $\text{C}_6\text{D}_6$  capture measurements at n\_TOF”. In: (2015). Internal n\_TOF report.
- [47] J. Leredegui-Marco, C. Guerrero, J.M. Quesada, and M Cortes. “Extension GEANT4 Application for  $\text{C}_6\text{D}_6$  capture: New carbon fiber setup for L-type detectors in EAR1”. In: (2016). Internal n\_TOF report.
- [48] Claudia Lederer. “Neutron capture measurements on  $^{62}\text{Ni}$ ,  $^{63}\text{Ni}$  and  $^{197}\text{Au}$  and their relevance for stellar nucleosynthesis”. Presented 01 Mar 2012. 2012. URL: <https://cds.cern.ch/record/1474071>.
- [49] M. Barbagallo. *Update on flux*. unpublished. Internal n\_TOF talk. 2020.
- [50] Richard L. Macklin, Joseph Halperin, and Ronald R. Winters. “Absolute neutron capture yield calibration”. In: *Nuclear Instruments and Methods* 164.1 (1979), pp. 213–214. ISSN: 0029-554X. DOI: [https://doi.org/10.1016/0029-554X\(79\)90457-9](https://doi.org/10.1016/0029-554X(79)90457-9). URL: <https://www.sciencedirect.com/science/article/pii/0029554X79904579>.
- [51] V. N. Kononov, I. I. Stavisskii, and V. A. Tolstikov. “Measurement of the radiative capture cross section of 25 keV neutrons.” In: *The Soviet Journal of Atomic Energy* 5(5) (1958), p. 1483.

- [52] N. Otuka, E. Dupont, V. Semkova, et al. “Towards a More Complete and Accurate Experimental Nuclear Reaction Data Library (EXFOR): International Collaboration Between Nuclear Reaction Data Centres (NRDC)”. In: *Nuclear Data Sheets* 120 (2014), pp. 272–276. ISSN: 0090-3752. DOI: <https://doi.org/10.1016/j.nds.2014.07.065>. URL: <http://www.sciencedirect.com/science/article/pii/S0090375214005171>.
- [53] A. K. Chaubey and M. L. Sehgal. “Test of Statistical Theory of Nuclear Reactions at 24 keV”. In: *Phys. Rev.* 152 (3 Dec. 1966), pp. 1055–1061. DOI: 10.1103/PhysRev.152.1055. URL: <https://link.aps.org/doi/10.1103/PhysRev.152.1055>.
- [54] R. L. Macklin, N. H. Lazar, and W. S. Lyon. “Neutron Activation Cross Sections with Sb—Be Neutrons”. In: *Phys. Rev.* 107 (2 July 1957), pp. 504–508. DOI: 10.1103/PhysRev.107.504. URL: <https://link.aps.org/doi/10.1103/PhysRev.107.504>.
- [55] R. P. Anand, M. L. Jhingan, D. Bhattacharya, and E. Kondaiah. “25 keV-neutron capture cross-sections”. In: *Nuovo Cimento A Serie* 50.2 (Mar. 1979), pp. 247–257. DOI: 10.1007/BF02902005.
- [56] G. Walter, H. Beer, F. Kaeppler, G. Reffo, and F. Fabbri. “The s-process branching at Se-79”. In: *Astronomy and Astrophysics* 167.1 (Oct. 1986), pp. 186–199. URL: <https://ui.adsabs.harvard.edu/abs/1986A&A...167..186W>.
- [57] A. G. Dovbenko, V. E. Kolesov, V. P. Koroleva, and V. A. Tolstikov. “Cross sections of radiative capture of neutrons in the 10–350 keV energy range”. In: *Soviet Atomic Energy* 27.5 (1969), pp. 1185–1189. DOI: 10.1007/BF01164969. URL: <https://doi.org/10.1007/BF01164969>.
- [58] G. Walter. “Temperatur und Neutronendichte der schwachen Komponente des s-Prozesses”. In: *KfK Bericht* 3706 (1984).
- [59] K. Göbel, C. Beinrucker, B. Brückner, et al. “Neutron activation of  $^{69}\text{Ga}$  and  $^{71}\text{Ga}$  at  $k_B T \approx 25\text{ keV}$ ”. In: *Phys. Rev. C* 103 (2 2021), p. 025802. DOI: 10.1103/PhysRevC.103.025802. URL: <https://link.aps.org/doi/10.1103/PhysRevC.103.025802>.
- [60] Benjamin Sebastian Brückner. “ $^7\text{Li}(p,n)^7\text{Be}$  neutron fields and their application for astrophysics”. doctoralthesis. Universitätsbibliothek Johann Christian Senckenberg, 2022, p. 203. DOI: 10.21248/gups.68639.
- [61] F. Bečvář. “Simulation of  $\gamma$  cascades in complex nuclei with emphasis on assessment of uncertainties of cascade-related quantities”. In: *Nuclear Instruments and Methods in Physics Research A* 417.2 (Jan. 1998), pp. 434–449. DOI: 10.1016/S0168-9002(98)00787-6.
- [62] Nancy M Larson. “Updated User’s Guide for Sammy: Multilevel R-Matrix Fits to Neutron Data Using Bayes’ Equations”. In: (Oct. 2008). DOI: 10.2172/941054. URL: <https://www.osti.gov/biblio/941054>.
- [63] Tabea Kuttner. “Stellare Neutroneneinfangsquerschnitte von  $^{69,71}\text{Ga}$ ,  $^{23}\text{Na}$  und  $^{37}\text{Cl}$ ”. MA thesis. Goethe-University Frankfurt, 2022.





## ACKNOWLEDGEMENT

I would like to express my gratitude to everybody who helped me in and during the creation of this thesis.

First of all, my sincerest thanks to Prof. Dr. René Reifarh, not only for accepting me into his group, but introducing me to the joy of scientific thinking and work. I always felt supported, understood and encouraged, not just as a PhD student, but as a human being as well. Discussions about physics, being someone that also liked the "math side" of things, seeing how you interacted with both peers and students made me always look forward to life and work in our group. René, you kept reminding us that there is "a life beyond physics", but you also made this side of it incredibly interesting and enjoyable!

To Dr. Kathrin Göbel, my thanks for introducing me to this group, making me feel welcome from the start, and helping me with all the pitfalls that I now know to be completely normal in experimental work, but that seemed at times insurmountable in the beginning; and at the same time always keeping an eye out to make sure I did not stress myself too much.

Philipp Erbacher, Benjamin Brückner and Meiko Volkmandt, I cannot properly express how much your support and friendship means to me. Be it physics discussions, walk&talks, boardgame or barbecue nights, it was always you who made me feel at home here. Family are the people who unconditionally share both your joy and your suffering, and I could not ask for better brothers than the three of you!

To Sophia Dellmann, for her patience and positivity, as well as her unrivaled eye for details when proofreading this thesis.

My thanks to the Arbeitsgruppe Experimentelle Astrophysik, especially Dr. Stefan Fiebiger, Markus Reich, Lukas Bott, Dr. Mario Weigand and Kirstin Schäfer, for your support and the positive and inclusive atmosphere you created every day.

To the n\_TOF trio Dr. Michael Bacak, Dr. Marta Sabaté-Gilarte and Dr. Lucianna Damone, for your competence, reliability and friendship. You made CERN a home away from home, and my experiment among the most memorable three months in my life, which I will always cherish.

Efcharistó to Dr. Maria Diakaki and Dr. Athanasios Stamatopoulos (although you will always be Thanos to me), for your kindness, patience and constant joyfulness while helping me with the experiment.

To Dr. Mirco Dietz, Dr. Samuel Bennett, Dr. Jorge Lerendegui Marco, Dr. Adria Casanovas Hoste and Dr. Stanislav Valenta for the invaluable discussions about the analysis, your open ears and always being willing to take the time needed.

A special thank you to the n\_TOF collaboration, especially the local team during my time there, Dr. Federica Mingrone, Dr. Daniela Macina, Dr. Massimo Barbagallo and Dr. Mario Mastromarco.

My gratitude to Steffi Schönberger, who was the one to even suggest this adventure in Frankfurt, and who was there for me for such a long time. Your support and your sacrifices played a big role in the creation of this thesis, and for that I will always be grateful.

Schlussendlich gilt mein Dank meiner Familie. Emin, du hast meine Begeisterung für die Physik schon in jungen Jahren geweckt, und mir immer die Freiheit gelassen und mich darin unterstützt, diesen Weg auf meine Art zu verfolgen. Und Senay, deine Arbeitsmoral und Disziplin, gekoppelt mit deiner bedingungslosen Unterstützung, waren mir stets ein großes Vorbild.







### Personal information

Name: Cem Deniz Kurtulgil  
Date of birth: June 26th, 1986  
Place of birth: Lingen (Ems), Germany  
Citizenship: German

---

### Education

since 2017      Research assistant and PhD student  
Goethe University Frankfurt

2006-2016      Diploma student in Physics  
Technical University Munich  
Diploma thesis: *Design of an algorithm for the treatment of isomeric states in a nuclear reaction network code*  
Supervisor: Prof. Dr. Shawn Bishop  
Academic degree: Diplom-Physiker Univ.

2005-2015      Diploma Student in Mathematics  
Technical University Munich  
Vordiplom in 2009

2005            General qualification for university entrance: Abitur  
Emsland Gymnasium, Rheine